Novel Catalytic Applications of Carbon Nanofibers on Sintered Metal Fibers Filters as Structured Supports

THÈSE N^{O} 4224 (2008)

PRÉSENTÉE LE 7 NOVEMBRE 2008

À LA FACULTÉ SCIENCES DE BASE
LABORATOIRE DE GÉNIE DE LA RÉACTION CHIMIQUE
PROGRAMME DOCTORAL EN ENVIRONNEMENT

ÉCOLE POLYTECHNIQUE FÉDÉRALE DE LAUSANNE

POUR L'OBTENTION DU GRADE DE DOCTEUR ÈS SCIENCES

PAR

Marina RUTA

acceptée sur proposition du jury:

Prof. A. Mermoud, président du jury
Dr L. Kiwi, directrice de thèse
Prof. P. J. Dyson, rapporteur
Dr B. Louis, rapporteur
Dr S. Perathoner, rapporteur

ÉCOLE POLYTECHNIQUE
FÉDÉRALE DE LAUSANNE
Suisse
2008

Esiste solo una veduta perfetta ed è quella del cielo sopra le nostre teste. Le altre non sono che brutte copie di quella lassú. E.M. Forster

Aknowledgments

I have worked on this thesis from October 2005 to September 2008 in the Group of Chemical Reaction Engineering (former Laboratory of Chemical Reaction Engineering). It has been an incredible journey through science and personal development. As experienced travelers know, it is impossible to reach the final destination without the help of people met on the road.

First of all I would like to thank Prof. Renken for taking me into his group and MER Liouba Kiwi-Minsker, for being my guide during this three years. I express my gratitude for her trust and for keeping me on the right track whenever I needed an advice. Her vision on this research project has always been clear and she managed to keep the light on my steps.

I thank Prof. André Mermoud for having presided the jury, as well as all its members: Dr. Siglinda Perathoner, Dr. Benoît Louis and Prof. Paul Dyson for taking the time to read my thesis and to initiate the fruitful discussion on the day of my exam.

I am extremely grateful to:

- Pascal Tribolet, who relayed his knowledge and expertise on carbon nanofibers to me. Thanks for being such a good friend as well, and for proof reading my thesis.
- Igor Yuranov, who was always beside me at the beginning of this work and who inspired me with his silent and deep wisdom.
- Natasha Semagina, for her unconditionate support, her assistance in the lab, her friendship. Last but not least for proof reading my thesis and coming up with such interesting comments on it.
- Prof. Dyson, Dr. Gabor Laurenczy and Dr. Dongbin Zhao from the LCOM. Not only they introduced me to the magic world of Ionic Liquids, but they advised, supported and prepared samples for my research work. It was a real pleasure to collaborate with them.

- Dr. Dirk Rosenthal, from the FHI in Berlin, for spending most of his evenings in a week characterizing the samples with me and for his support to interpret the XPS results.
- Daniele Laub, Marco Cantoni and Fabienne Bobard from the CIME, for their support on the electronic microscopy of my samples.
- to the semester/master students who worked with me: Muriel Pasquier, Lu Yi, Natalia Mergulis, and in particular Turan Eslanloo-Pereira.

Thanks to the technicians, the electricians, to PAP and the secretaries Mme Szuman, Mme Anken, Vida and Stéphanie which helped a lot in administrative stuff.

Special thanks to my colleagues: Martin, Kim, Edi, Bryan, AnneLaure, Micaela, Dmitri, Kashid, Ameya; to my multiple office mates; Petra, Subbu, Mickael; to the Corbusier lunch mates: Agnieszka, Michal, Lisa and to the rest of the Comin's group: Pietro and Erika.

Thanks to my friends in Geneva, because they managed to keep my mind busy with life instead of just focusing on my beloved carbon nanofibers. Amongst the others a special thank to Camilla e Roberto, who made me feel at home when I have lost mine. Grazie anche a Marta e Giacomo, perchè va un po' cosí.

Thanks to the old friends from Milan, especially to those who were curious enough to cross the Alpes, come and see me as emigrant researcher. In particular Valentina, Arianna e Andrea.

Gracias al Gonzalo que siempre me decia "cuidate mucho".

Grazie alla mia famiglia, a cui devo tanto di quello che sono oggi e che saró nel futuro. Al nonno Lelio, che mi spiegava la trigonometria quando avevo appena 9 anni, alla nonna Dorina che vicina a me per soli 6 mesi mi ha passato la sua maieutiké techné, a Chiara che grazie al suo amore per i cavalli mi ha insegnato cosa significa "addomesticare", a babbo soprattutto per il rispetto e la fiducia che ha riposto nelle mie scelte di vita. Ma soprattutto a Rosanna, perché è il catalizzatore della mia vita.

Abstract

Supported metal catalysts are important from both an industrial and a scientific point of view. They are used, amongst others, in large-scale processes such as catalytic reforming, hydrotreating, polymerization reactions and hydrogenations. Often, these catalysts consist of nanosized metal particles deposited on a suitable support, which acts as an anchor for the active phase and, in several cases, contributes to improve the overall catalyst performances. The growth of carbon nanofibers on sintered metal fibers filters (CNF/SMF) by hydrocarbons catalytic decomposition results in a structured composite material presenting all the suitable characteristics for its application as catalyst support.

The main objective of this thesis was to develop novel catalytic systems based on CNF/SMF as catalytic support for continuous gas-phase hydrogenations. At first, the synthesis of CNF/SMF was optimized to tailor the properties of the material for further applications as catalytic support. The use of ethylene as carbon precursor and high synthesis temperature (973K) provided high yields of well-ordered CNF with increased specific surface area (SSA), up to 516 m^2/g. On the other hand, the synthesis of CNF by ethane decomposition, which is less reactive than ethylene, resulted in a support with higher permeability, minimizing the pressure drop and being more suitable in a continuous-flow reactor. After the synthesis, the CNF surface was activated by treatment with O_3 or H_2O_2. A novel technique, which consist of XPS analysis after step-wise TPD in UHV conditions, was developed and applied for the surface characterization. It allowed to assess the nature of the functional groups created on the CNF surface. The O_3-activation was found the most effective for increasing the acidity of the CNF/SMF surface, yielding a relatively high amount of carboxylic functional groups. These groups are important because involved in the chemical anchoring and stabilization of the active metal deposited on the support.

Industrially, many hydrogenations are performed over supported metal catalyst. The majority of these reactions are known to be structure sensitive reactions, so the control of the metal particle size is crucial in order to study the catalyst activity and selectivity. We prepared monodisperse-sized Pd nanoparticles (8, 11 and 13 nm) via the reverse microemulsion method and deposited on CNF/SMF and activated-

CNF/SMF for a two-fold study: the effect of the nanoparticles size and the effect of the support nature on the selective hydrogenation of acetylene. The antipathetic size dependence of the TOF disappeared at particle size bigger than 11 nm. The initial selectivity to ethylene ($\sim 60\%$) was found size-independent. The structure-sensitivity relations have been discussed in terms of "geometric" and "electronic" nature of the size-effect and rationalized assuming a Pd-C_x phase formation which is known to be size-dependent. CNF/SMF supports with increased acidity diminished the formation of coke and changed the by-products distribution, diminishing the catalyst deactivation.

Subsequently, CNF/SMF was applied to develop a new catalytic system: the Structured Supported Ionic Liquid Phase (SSILP) catalyst, embedding an active Rh complex. The selective gas-phase hydrogenation of 1,3-cyclohexadiene to cyclohexene was used as model reaction. The SSILP based on CNF/SMF supports showed a high turnover frequency, up to 250 h^{-1} and selectivity > 96%. Multiple advantages of supporting a homogeneous active phase, dissolved in IL, on CNF/SMF have been demonstrated: the thin layer of IL was homogeneously distributed over the mesoporous support, so mass transfer limitations could be avoided, furthermore the chemical inertness of the CNF prevented any interaction between the active phase dissolved in IL ensuring an efficient use of the Rh complex.

The SSILP concept can be applied not only for the "heterogenization" of a transition metal catalyst, but also to obtain metal nanoparticles with monodispersed size via the reduction of a metal precursor dissolved in IL. In this case, IL provides a suitable environment for the nucleation and growth of the nanoparticles. By applying the SSILP concept to the selective hydrogenation of acetylene, the influence of IL on the stability of the nanoparticles was investigated. Moreover, the different solubilities of reactants and products in the IL phase allowed to improve the selectivity toward ethylene. Monodispersed Pd nanoparticles of 5 and 10 nm in SILP on CNF/SMF showed excellent long-term stability. The lower solubility of ethylene than acetylene in the IL had the beneficial effect of allowing high selectivity to ethylene up to 85%, due to the inhibition of its consecutive hydrogenation to ethane.

In conclusion, a novel catalytic system for continuous-flow, gas-phase hydrogenations was conceived, taking advantage of the suitable characteristics of CNF/SMF supports. The SSILP concept, involving both homogeneous and heterogeneous active phases has been demonstrated, indicating a great potential and flexibility for continuous-flow industrial applications.

Keywords: heterogeneous catalysis; structured catalyst; carbon nanofibers; supported ionic liquids; gas-phase hydrogenations; Rh complex; Pd-nanoparticles.

Version Abregée

Le développement de catalyseurs supportés est considéré important à la fois d'un point de vue industriel que scientifique. Ce type de catalyseurs est utilisé, entre autres, par des procédés à grande échelle comme le "reforming" catalytique, les "hydrotreating", les réactions de polymérisation et les hydrogénations. Typiquement, ils sont constitués de nanoparticules métalliques déposées sur un support, qui ancre la phase active et, parfois, aide à améliorer les performances du catalyseur. La croissance de nanofibres de carbone sur filtres de fibres métalliques frittées (CNF/SMF), par décomposition catalytique d'un hydrocarbure, permet d'obtenir un matériau composite structuré qui présente toutes les caractéristiques souhaitées pour l'application en tant que support catalytique. L'objectif principal de ce travail à été de développer de nouveaux systèmes catalytiques, employant les CNF/SMF comme support catalytique pour des réactions d'hydrogénation en phase gazeuse et en continu. Premièrement, la synthèse des CNF/SMF a été optimisée afin d'adapter les propriétés du matériau aux applications catalytique. En employant l'éthylène comme précurseur de carbone et en effectuant la synthèse à haute température (973 K), on obtient un haut rendement de CNF avec une structure cristalline bien organisée et l'on atteint une surface spécifique très élevée (jusqu'à 516 m^2/g). D'autre part, la synthèse des CNF par décomposition d'éthane, celui-ci étant moins réactif que l'éthylène, permet d'obtenir un support plus perméable qui est mieux employé dans un réacteur continu à lit-fixe en minimisant les pertes de charge. Après la synthèse, la surface des CNF peut être activée par traitement avec O_3 ou H_2O_2. Pour caractériser la surface, une nouvelle technique a été employée, qui consiste en une TPD par étapes, suivie d'une analyse XPS dans des conditions de vide ultra-poussé. Cette technique permet d'estimer la nature des groupes fonctionnels formés à la surface des CNF. L'activation par O_3 s'est revelée plus efficace pour augmenter l'acidité du composite CNF/SMF, en créant une plus grande quantité de groupes fonctionnels carboxyliques en surface. Ces groupes sont importants parce qu'ils facilitent l'ancrage chimique et la stabilisation des espèces métalliques actives déposées sur le support. Beaucoup d'hydrogénations industrielles sont conduites sur des catalyseurs métalliques supportés. On sait que la structure de la phase catalytique

active influence la majorité de ces réactions, donc ainsi le contrôle de la taille des particules métalliques est crucial pour étudier l'activité et la sélectivité du catalyseur. On a préparé des nanoparticules de palladium avec une distribution de tailles mono dispersée (8,11 et 13 nm), ceci à l'aide d'une méthode de microémulsion. Ensuite, on les a déposées sur CNF/SMF et CNF/SMF activé pour étudier l'influence de la taille des particules et de la nature du support sur l'hydrogénation sélective de l'acétylène. La dépendance du TOF de la taille des particules disparaisse pour des tailles plus grandes que 11 nm. La sélectivité initiale par rapport à l'éthylène ($\sim$60 %) a été trouvé indépendante de la taille. La liaison entre la structure du palladium et l'activité du catalyseur a été interpreté en terme de nature "géométrique" et "électronique", et rationalisée en supposant la formation d'une phase Pd-Cx, qui notamment dépend de la taille des particules. Les supports CNF/SMF plus acides diminuent la formation de "coke" et changent la distribution des co-produits, tout en ralentissant le désactivation du catalyseur. Le support de CNF/SMF a ensuite été appliqué pour concevoir un nouveau système catalytique basé sur un complexe de Rh dissous en phase liquide ionique à la surface d'un support structuré (SSILP). L'hydrogénation sélective de 1,3-cyclohexadiène en cyclohexène a été testée en tant que réaction modèle. L'emploi de CNF/SMF pour le développement du SSILP permet d'obtenir des TOF élevés, jusqu'à 250 h^{-1}, et des sélectivités > 96%. En supportant la phase active sur CNF/SMF, on a donc montré plusieurs avantages : la couche de liquide ionique est mince et homogène grâce à la meso-porosité du support, les limitations par transfert de masse sont donc négligeables. De plus l'inertie chimique des CNF empêche toute interaction avec la phase active dissoute dans le liquide ionique, assurant ainsi une utilisation efficace du complexe de Rh. Le concept du SSILP peut être appliqué non seulement pour "hétérogeniser" un complexe de métal de transition comme catalyseur, mais aussi pour synthétiser des nanoparticules métalliques de taille mono dispersée. Ceci est fait par réduction d'un précurseur métallique dissous dans un liquide ionique supporté. Dans ce cas, le liquide ionique fournit un environnement approprié pour la nucléation et la croissance des nanoparticules. En appliquant le concept du SSILP à l'hydrogénation sélective de l'acétylène on a pu étudier l'influence du liquide ionique sur la stabilité des nanoparticules. D'ailleurs, les réactifs et les produits de la réaction étant plus ou moins solubles dans la phase liquide ionique, il a été possible d'améliorer la sélectivité envers l'éthylène. Des nanoparticules de palladium avec une taille mono dispersée (5 et 10 nm) synthétisées en SILP sur CNF/SMF sont exceptionnellement stables sur la longue durée. L'éthylène étant moins soluble que l'acétylène en phase liquide aide à inhibir l'hydrogénation consécutive en éthane et ainsi obtenir une sélectivité jusqu'à 85%. En conclusion, un nouveau système catalytique a été conçu pour des hydrogénations en continu et en phase gazeuse, grâce aux caractéristiques appropriées des supports CNF/SMF. Le concept du SSILP, en impliquant des phases

actives soit homogènes soit hétérogènes, a été développé et il a montré un grand potentiel et flexibilité pour des applications industrielles en continu.

Mot clefs : catalyse hétérogène, catalyseurs structurés, nanofibres de carbone, liquides ioniques supportés, hydrogénation en phase gazeuse, complexe de Rh, nanoparticules de Pd.

Contents

Nomenclature

Abbreviations

AAS Atomic Absorption Spectroscopy

CNF Carbon Nanofibers

CNT Carbon Nanotubes

CVD Chemical Vapor Deposition

EDX Energy Dispersive X-ray Spectrometer

GC Gas Chromatography

HRTEM High Resolution Transmission Electron Microscopy

IL Ionic Liquids

IR Infrared Spectroscopy

ME Microemulsion

MFC Mass Flow Controller

MS Mass Spectrometer

NMR Nuclear Magnetic Resonance

SEM Scanning Electron Microscopy

SILP Supported Ionic Liquid Phase

SMF Sintered Metal Fibers

SSA Specific Surface Area

SSILP Structured Supported Ionic Liquid Phase

TEM Transmission Electron Microscopy

TMC Transition Metal Complexes

TOF Turnover frequency

TPD Temperature Programmed Desorption

TPO Temperature Programmed Oxidation

UHV Ultra High Vacuum

XPS X-ray Photoelectron Spectroscopy

XRD X-ray Diffraction

Roman Letters

C Concentration [mol/m^3]

d Diameter [m]

E_a Activation energy [kJ/mol]

F Molar Flow [mol/s]

m Mass [g]

MM Molar mass [g/mol]

n Number of moles [mol]

p Pressure [bar]

Q Volumetric flow [m^3/s]

R Reaction rate [mol/g_{cat}s]

S Selectivity [-]

T Temperature [K]

V Volume [m^3]

w Mass fraction [-]

X Conversion [-]

Greek Letters

τ Residence time [s]

τ' Modified residence time [g s/m^3]

Chapter 1

Introduction

The chemical industry nowdays needs to integrate the principles of green or sustainable technology, due to the growing awareness of its past negative impacts on the environment and the society. The sustainable production of chemicals can be achieved by reaching **higher product selectivity, high conversion, lower emissions and improved energy efficiency**. Catalyzed chemical syntheses accounts for 90% of the current chemical processes [1], including the manufacture of petroleum-based products and fuels, production of polymers, fine chemicals, and pollution abatement. Since the majority of chemical processes is influenced by the performance of catalysts, new concepts in catalyst design are required in order to innovate toward sustainable technologies. Heterogeneous catalytic systems are complex environments in which every component contributes to the final goal of improving the sustainability of chemical processes. The nature, structure and form of the **active phase** as well as the nature of the material used as **support** play the most important role in order to improve the efficiency of the catalyst toward a given reaction. Therefore, new materials and synthetic routes for different shaped catalyst are today extensively investigated.

1.1 Carbon Nanostructures as Catalyst Supports

Carbon in its various forms is widely used for catalysis, especially as support for metal active phases [2]. The discovery of carbon nanofibers (CNF) and their particular properties led to important technological deliveries in this field [3]. The structure and the shape of CNF can influence the activity of the supported catalytic phase as well as its stability, but at the same time CNF are chemically inert and specific pretreatments are required to achieve the optimal interaction between them and the catalyst precursor. This

can complicate the synthesis of the catalyst, but the major drawback to the application of CNF as support is their fluffy powder form. They can therefore be difficult to be used in the conventional catalytic reactors. Indeed, fixed-beds could suffer of high pressure-drop, reducing the energy efficiency of the process. In order to overcome this problem, CNF have been successfully immobilized on structured supports [4], but the potential of the resulted composite has not been hitherto fully exploited.

1.2 Supported Ionic Liquid Phase (SILP) catalysis

For a particular transformation, various routes can be chosen applying different types of catalytic methods, e.g., heterogeneous or homogeneous. The heterogeneous is usually preferred because it offers the most economic and ecological benefits. Nevertheless, great research efforts are nowdays dedicated to the immobilization of homogeneous catalysts, which could exhibit the advantages of both methods: easy separation and recovery, stability, easy handling and well-defined structure at molecular level plus the possibility to tune the properties of the catalytically active phase. At the same time, the potential to reduce pollution in industrial processes have led to extensive investigations of ionic liquids (IL) as alternative reaction media for a variety of applications that conventionally used organic solvents. Among different methods, the "heterogenization" of homogeneous catalyst can be achieved by dissolving in IL phase, subsequently supported on solid and porous materials [5]. Supported ionic liquid phase (SILP) catalysis allows to broaden the application of transition metal complexes in catalysis and their use for fixed-bed technologies. In this case, since the support material can interact with the dissolved catalyst, the employment of an inert, porous and macrostructured support is envisageable. Furthermore, in order to avoid mass transfer limitations, the thickness of the IL layer on the support should be minimized approaching to the distance of the diffusion layer of the reactants into the liquid phase.

1.3 Metal Nanoparticles with Controlled size for Catalysis

Many important reactions are catalyzed by metal nanoparticles [6], which are considered as the interface between heterogeneous and homogeneous catalysis because they can be used in homogeneous systems or they can be heterogenized by fixation on a suitable support. Metal nanoparticles are small nanocluster with diameters in the range of 1-20 nm and with near-monodispersed size distribution. Therefore, they should be reproducibly synthesized and thus successfully employed for studying structure-sensitive reactions (e.g. hydrogenations, oxidations, Suzuki and Heck coupling). The standard approaches for

preparing catalytically active nanoparticles are often based on the direct synthesis over catalytic support, which can result in a lack of control over the nanoparticle size. On the contrary, colloidal methods, which provide electrostatic and/or steric stabilization, allow easy tuning of the nanostructure size and morphology [7]. Once obtained nanoparticles with monodispersed size, it is very important though to find the right support for the chosen catalytic application. The support should avoid the aggregation of the nanoparticles and at the same time provide good accessibility of the reactants. In addition, it can influence the electronic and catalytic properties for the improvement of the activity and selectivity of the supported nanoparticles.

1.4 Goals and Scope of the Thesis

This thesis aims on the development of novel CNF-based structured catalytic systems, useful for continuous-flow fixed-bed reactors applied for hydrogenation reactions. A prerequisite for such a study is tailoring the CNF synthesis over SMF and the CNF surface functionalization for the specific catalytic application. The further objectives addressed in this work include the use of CNF grown on SMF as structured support for:

- **Pd nanoparticles synthesized and stabilized by a surfactant in a microemulsion (ME) for the selective hydrogenation of acetylene.** Thanks to the precise control on the particle size and the good interaction between Pd nanoparticles and CNF, the resulting catalyst can be used for studying the structure sensitivity of the reaction. Our scope will be to find the optimal size of the nanoparticles, which will afford superior catalytic performance for the hydrogenation of acetylene. Furthermore, by tuning the surface functionalities of CNF we will investigate on the effect of the support on the catalytic properties of Pd nanoparticles with monodispersed size.

- **Heterogenization of a homogeneous catalyst, based on a transition metal complex (TMC), in SILP.** Toward this goal it will be important to find the most efficient synthetic route and to compare different structured support in a fixed-bed reactor for a model hydrogenation reaction, such as the selective conversion of a diene to a monoene. Through the study and optimization of the catalytic system we will try to find the best structured support for the SILP catalytic application.

- **Pd nanoparticles synthesized and stabilized in SILP for the selective hydrogenation of acetylene.** Since IL provide a good environment for the nucleation and growth of metal nanoparticles with monodispersed size, our goal is to synthesize SILP Pd nanoparticles with controlled size

through a rather simplified preparation method than the ME synthesis. Subsequently, we will investigate about the use of the resulting catalyst for improving the selectivity and the stability of the Pd nanoparticles for the chosen reaction.

1.5 Outline of the Thesis

Chapter 2 provides an overview on the state of the art as to structured catalysts, carbon nanostructures in catalysis, the development and application of SILP catalyst as well as the formation of metal nanoparticles in IL phase; an introduction to the literature concerning the acetylene hydrogenation, studied during this thesis, is presented.

In **Chapter 3** the experimental set-ups used during the course of this work are explained, as well as the preparation/activation methods of the catalysts herein developed and tested. Moreover, this section presents the different physico-chemical characterization techniques employed through the study.

Chapter 4 addresses the synthesis and characterization of CNF on SMF, varying the carbon precursor, the synthesis temperature and time. Moreover, the results of the surface modification of CNF by two different oxidative treatments are presented (O_3-or H_2O_2-based), as well as the characterization of the functional groups by a novel technique which couples step-wise temperature programmed desorption (TPD) with subsequent X-ray photoelectron spectroscopy (XPS) analysis in a UHV chamber. This results were obtained in collaboration with the department of Inorganic Chemistry at the Fritz Haber Institute of the Max Planck Society in Berlin.

Chapter 5 deals with the development of a structured SILP catalyst, based on a Rh complex as active phase homogeneously dissolved in IL, and on different structured supports. The results obtained for the gas-phase hydrogenation of 1,3-cyclohexadiene in a fixed-bed reactor show how it is possible to improve the performance of the catalyst by using CNF/SMF supports. The influence of different parameters during the synthesis of the SILP catalyst, such as the ligand content and the acidity of the catalytic media, has also been reported.

In **Chapter 6** the study of monodispersed Pd nanoparticles supported on CNF/SMF in the hydrogenation of acetylene is described: this work demonstrates that the nanoparticle size and the acidity of the support can influence the performance of the catalyst.

In **Chapter 7** the research aiming at a further extension of the structured SILP catalysis to the hydrogenation of acetylene is described. At this purpose, a novel method for the synthesis of Pd nanoparticles in IL

containing a reducing functionality is applied and the influence of the SILP both on the Pd nanoparticles characteristics and on their catalytic performance is reported.

Finally, in **Chapter 8** a summary of the results of the previous chapters is given and some concluding remarks are presented.

Chapter 2

State of the Art

2.1 Structured Fibrous Supports for Catalysis

2.1.1 Structured Catalysts

Conventional fixed-bed reactors are packed with powdered or granulated catalysts. Thus, they present some obvious disadvantages, such as maldistributions of various kind (including a non-uniform access of reactants to the catalytic surface), high pressure drop in the bed and broad residence time distributions. Structured catalysts are promising, as far as the elimination of these drawbacks is concerned. Two basic kind of structured catalysts can be distinguished:

- Structural packings covered with catalytically active material, similar in design to those used in distillation and absorption columns and static mixers.
- Monolithic catalysts as continuous unitary structures which contain many passages. A ceramic or metallic support is coated with a layer of material in which active species are dispersed. The catalytically active material is present on, or inside the walls of these passages.

Fibrous catalysts are structured materials belonging to the first category. The small fiber diameter, on the order of 1-80 μm, makes possible the use of support sizes in the same order of magnitude as powders, but without the disadvantages of handling and pressure drop associated with powders. A comparison of some characteristics of fibers with monolith and pellet structures is given in Table 2.1.

Table 2.1: Characteristics comparison for pellet-, monolith- and fibrous-catalysts. Adapted from [8]

	Pellet	Monolith	Fibrous structure (wire-mesh, cloths)
Particle/channel diameter [mm]	3.0-5.0	1.5	0.01-2
Diffusion length [μm]	100-2500[a]	25-100[b]	0.15[c]
Specific surface area [m^2/g]	up to 1000	-	2-2000[d]
Geometric surface area [m^2/m^3]	1200	1900	up to 100 000
Porosity [-]	0.42	0.65	0.8

[a] Depending on catalyst structure

[b] Washcoat thickness

[c] Depending on porosity

[d] Depending on material

Ahlstrom-Silversand and Odenbrand compared metal cloths, monolith- and pellet-catalysts during catalytic combustion [9]. Although in terms of reactor performance per volume 1 mm pellets were comparable to a 20 mesh-cloth, and that both were better than monolith, the performance comparison on pressure drop indicated the monolith as the preferred support followed by the wire-mesh and pellets. Eventually, the wire-mesh showed the best behavior in terms of thermal response and losses by radial temperature gradient. Fibrous catalysts based on precious metals (Pt, Ru, Ag) have been extensively used in the production of nitric acid, hydrocyanic acid and aldehydes [10]. Since they present the inconvenient of being very expensive, during the last decade cheaper metals, as well as glass and carbon fibers were explored as potential material for fibrous catalysts.

2.1.2 Advantages of Fibrous Materials

The fibrous materials are flexible and can be packed in fixed-bed of different geometries and in different shapes, which would be otherwise impossible to reach with powdered or granulated materials. Furthermore, fibrous materials possess very high porosities, 70-90%, compared to randomly packed beds porosities of 34-60% [8]. The high porosity leads to low pressure drop, so fibrous material are seen as attractive alternatives in three-phase systems. However, high porosities are often associated to lower specific surface area and higher risk of channeling. The main advantage of fibrous materials is provided by their immobility and the short diffusion time of reactants through the bed, similar to the one provided

by monolithic structures. Other attractive features include the possibility of safer operation and easy scale-up.

The most studied and applied classes of materials are: carbon fibers, glass fibers and metallic wires. Catalyst based on metallic fibers are mainly used in highly exothermic and fast gas phase reactions, where their excellent heat transfer properties can help to avoid hot spot formation and their associate negative effects on the catalyst activity, selectivity and thermal runaway. Glasses are often used due to their relative chemical inertness, the absence of harmful metal-support interactions and their ability of facilitating the action of promoters. Activated carbon fibers (ACF) exhibit an apparent specific surface area (SSA), in the range of 1500-3000 m^2/g, but with a complex texture including macropores ($\varnothing$ 10^2-10^5 nm), mesopores ($\varnothing$ 2-10^2 nm) and micropores ($\varnothing$ < 2nm). Microporosity is detrimental for the efficiency of the catalysts, because the reactants often badly diffuse into the micropores where the catalytic active phase can be deposited, giving place to mass transfer limitations during the catalytic process.

2.1.3 Modification of the Surface of Metallic Fibrous Supports

The major drawback associated to metallic fibrous supports is their relatively small SSA, which can limit the dispersion of the active catalytic phase. To achieve better performances a non-porous support can be modified by coating with a layer at high surface area. Coating of stainless steel wires with active alumina by electrophoretic deposition was successfully realized by Vorob'eva *et al.* [11], even if it is a relatively expensive way of deposition. Thin catalytically active zeolite coatings were deposited on fibrous material by immersing the support in an aqueous sol-gel for *in-situ* hydrothermal synthesis of mesoporous ZSM-5 or MCM-41 zeolite crystals on the surface [12, 13]. A controlled method for the growth of homogeneous ZSM-5 on sintered metal fibers filters was more recently developed by Yuranov *et al.* [14], allowing SSA of 300-320 m^2/g. The catalyst packing achievable with this technique consisted of a three level structure: (1) a micro-structure of zeolite crystals; (2) a meso-structure of porous 3D media of sintered metal fibers; (3) a macro-structure of layered catalytic bed formed of composite elements.

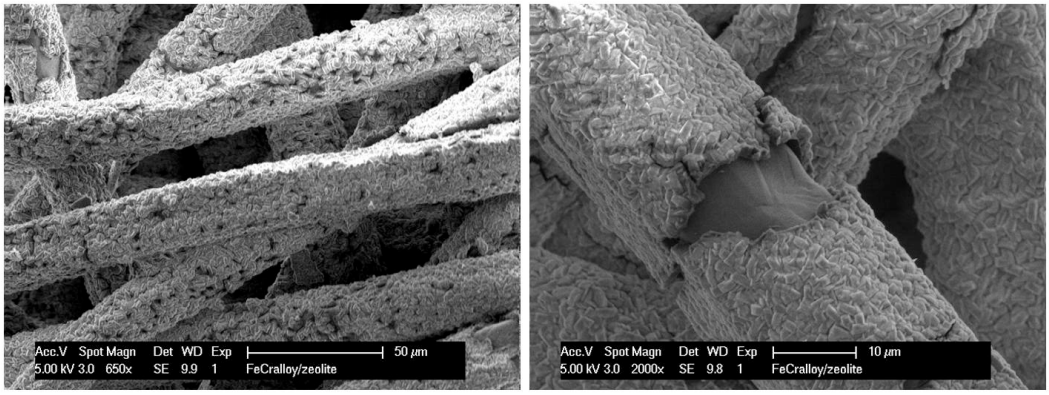

Figure 2.1: Sintered metal fibers coated by ZSM-5 following the method developed in [14]: an example of modified fibrous support.

Jarrah *et al.* created a novel structured catalyst support modifying the surface of Ni foams by the growth of a layer of carbon nanofibers on their surface and thus increasing the SSA. Similarly, Tribolet *et al.* developed the composite material, object of study of the herein reported thesis work, consisting of sintered metal fibers coated with carbon nanofibers, directly grown on the metallic surface [15]. The carbon nanofibers were firmly anchored to the surface and allowed reaching SSA of 310-472 m^2/g.

2.2 Carbon Nanostructures

2.2.1 Introduction

Carbon in the form of nanofilaments is known since it was observed as undesired byproduct in some industrial processes. In 1953, Davis *et al.* reported "an unusual form of carbon" in the course of experimental work on the deposition of carbon in the brickwork of blast furnaces [16]. The form of this carbon, observed for the first time by electron microscopy, was described as "minute vermicular growths". They were formed by the interaction of carbon monoxide and iron oxide in the so-called iron-spots in the brick. Later, carbon filaments were observed growing during the gas-steam reforming in steam cracker tubes, where they provoked rises in pressure drop and the deactivation of catalytic particles [17]. Finally, thanks to two important discoveries at the end of the last century, today these particular carbonaceous structures are not anymore seen as useless deposit from hydrocarbons decomposition, but they are object of an extensive scientific research around the world. The first important discovery, in 1985, was the third allotropic form of carbon: the fullerenes, tridimensional structures similar to

nanosized footballs [18]. The second one was the finding, by Iijima in 1991 [19], of a different structure in which carbon can arrange in the space: the carbon nanotubes.

2.2.2 Structures

Carbon nanostructures can be divided in two main subcategories: carbon nanofibers (CNF) and carbon nanotubes (CNT). Both derive from the basic structure of graphite, but while CNT are formed by a graphene sheet rolled up to form a hollow cylinder, CNF are formed by graphene platelets stacked together.

2.2.2.1 Carbon nanotubes (CNT)

The crystalline structure of graphite is formed by layers of carbon atoms arranged in hexagonal honeycomb planes, the layers are connected by weak Van der Waals interactions (overlap of π-orbitals perpendicular to the plane). Due to that conformation, the graphite exhibits anisotropic properties. An ideal CNT can be seen as a graphene sheet rolled-up in different directions to give a cylinder, whose extremities are closed by a semi-fullerene (Figure 2.2). The diameter is in the range of 0.7-10 nm and the length can reach several micrometers.

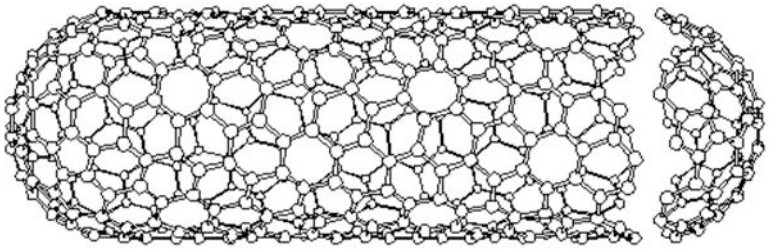

Figure 2.2: Ideal single-walled carbon nanotube.

Although the basic shape is cylindrical, the different orientations of the hexagones with respect to the central axis can affect the properties of the CNT. The main difference between graphite and CNT is the degree of hybridization sp^2 which changes around the circumference of the CNT. So, the way the graphene sheet is rolled (the amplitude of the chiral angle) originates three different conformation (Figure 2.3): armchair (*n, n*), zig-zag (*n, 0*) which are achiral, and all the possibility in-between (*n, m*), which are chiral.

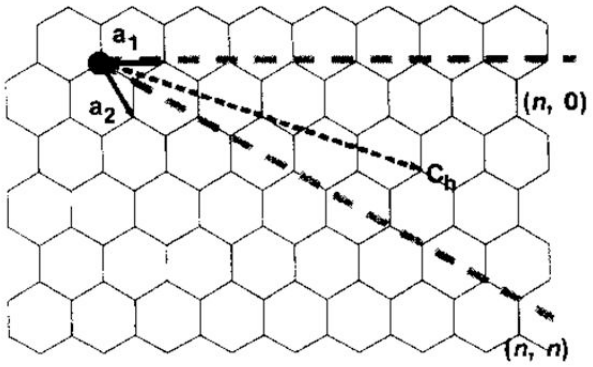

Figure 2.3: Geometric representation of the CNT chirality on a graphene layer.

So-called single-walled nanotubes (SWNT) are the structural units and thanks to the high ratio length-diameter can be virtually considered as mono-dimensional periodic structures along the axis. Many structural units, co-axially organized at the same distance of layers in graphite (0.34 nm), constitute muti-walled nanotubes (MWNT). Their diameter is bigger, increasing the walls number, and can reach up to 50 nm.

2.2.2.2 Carbon nanofibers (CNF)

Small graphene sheets can also arrange themselves in the space stacking together in a fibrous morphology and leaving a small or no central channel. The resulting structure is referred to as carbon nanofibers. According to the orientation of the graphene layers with the axis of the fiber, three main categories of CNF can be distinguished (Figure 2.4):

- Platelet, the graphene sheets are perpendicular to the fiber axis.
- Herringbone-like, the graphene layers form an angle of 45° with the fiber axis.
- Ribbon-like, the graphene sheets are parallel to the fiber axis.

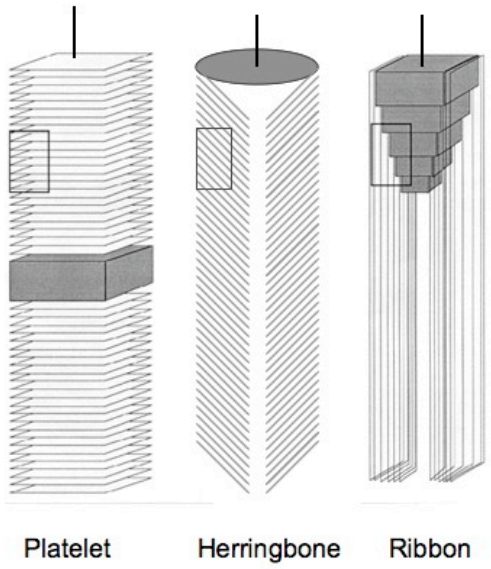

Figure 2.4: Morphologies of CNF.

CNF assume a tubular morphology due to the anisotropic surface free-energy of graphite, according to the thermochemical model elaborated by Tibbetts [20]. Generally, CNF diameters are bigger than for CNT, reaching values up to 200 nm, but the inter-planar distance is the same as for MWNT, or graphite. Similarly to CNT, the length can be of several micrometers and depends on the growing time. CNF exhibit properties intermediate between those of typical vapor grown carbon fibers and MWNT.

2.2.3 Synthesis Methods

Two different class of synthesis methods can be distinguished:

- physical methods, based on the "direct energy processing", such as laser ablation of a graphite target or arc discharge between two graphite electrodes (Figure 2.5).
- chemical methods, based on the presence of a "chemical atmosphere" in the reacting zone, like the traditional chemical vapor deposition (CVD) of hydrocarbons (Figure 2.6).

In the first case the nucleation process is instantaneous, and the non-equilibrium conditions, in which the growth takes place, account for high temperatures and chemical potential gradients. For the chemical methods the synthesis is carried out in equilibrium conditions, where temperature, pressure and chemical

potential are constant: the nucleation of carbon nanostructures is rather a continuous process, dependent on the equilibrium constant of the reactions involved.

The arc discharge synthesis is very similar to the Kratschmer-Huffman method of generating fullerenes [21], at low voltage ($\sim$12 to 25 V), high current (50 to 120 amps) an arc is produced between two graphite electrodes. An inert gas such as Ar or He is used as the atmosphere of the reaction, at a pressure of 100 to 1000 torr. It has been reported that CNT could only form if a metal catalyst is added to the anode [22,23]. The high energy, created between the electrodes, generates a plasma which sublimes the carbon at the anode and makes it condensate at the cathode in structured forms. The laser ablation technique uses a metal/graphite composite target placed in a quartz tube, at 1473 K, with an inert atmosphere (Ar or He at $\sim$ 500 torr), and vaporized with a laser pulse. The metal particles formed by the vaporization of the target catalyze the growth of carbon nanostructures which are collected via condensation on a cold finger downstream. Many by-products such as "bucky onions" and amorphous carbon are collected as well [24].

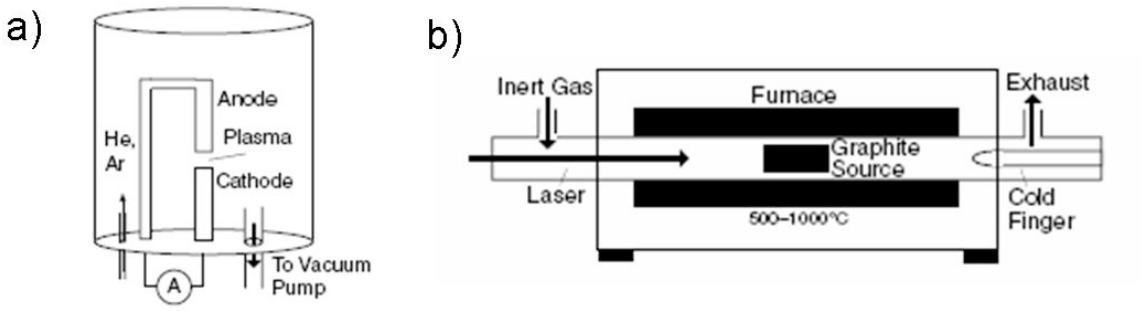

Figure 2.5: Schematic of physical methods, adapted from [25]: a) arc discharge chamber, b) laser ablation furnace.

Chemical methods never apply temperatures above 1373 K, so they are considered "medium temperature" synthesis, which allows reaching higher selectivities of carbon nanostructures. They rely only on thermal energy and on active metal catalytic species (Fe, Ni, Co and their alloys). CVD was first reported by Endo and coworkers [26] and today it is the most common process for the large-scale synthesis of carbon nanostructures [27]. The general procedure consists in thermally decomposing a gaseous carbon precursor (e.g. hydrocarbons, CO, alcohols) at the surface of the metal catalyst in a temperature range of 773-1373 K. Indeed, the temperature of the process strongly depends on the precursor chosen due to their different reactivities. The mostly used carbon precursors are methane, ethane, ethylene, acetylene

or carbon monoxide. The use of alcohols has been reported, explaining that the presence of OH groups may have a cleansing effect by preventing the formation of amorphous carbon [28]. The reactive mixture should contain a percentage of hydrogen in order to induce the reconstruction of the catalyst surface and to favor the precipitation of graphitic forms [29–31]. The metal catalyst can be in form of powders or *in-situ* generated by decomposition of an organometallic precursor (see 2.2.4). Nevertheless, in the majority of the cases the catalyst employed is supported in order to have a better control on the size of the particles which generate the carbon filaments [32]. The CVD can be carried out in two reactor typologies: the fixed-bed (Figure 2.6) or the fluidized-bed, which can be employed for a better thermal control and contact between gaseous reactive phase and solid catalyst [33].

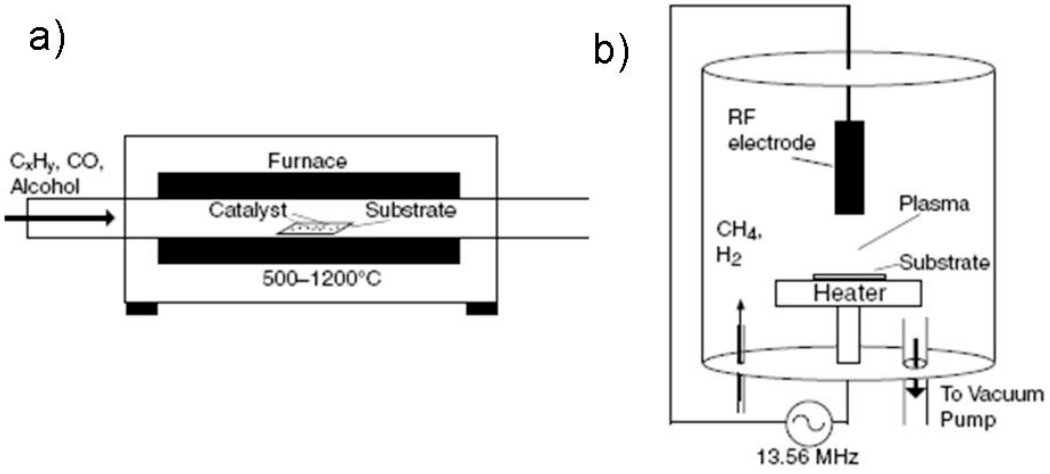

Figure 2.6: Schematic of chemical methods, adapted from [25]): a) CVD furnace, b) direct radiofrequency PECVD system.

As crossover between plasma-based growth and CVD synthesis, plasma-enhanced chemical vapor deposition (PECVD) have been extensively used to produce carbon nanostructures. By this technique the molecules are activated via weakly ionized plasma [34]. The low-pressure deposition chamber (Figure 2.6) is filled with the reactive gaseous mixture, where a discharge is induced by applying a high frequency voltage between two electrodes. The substrate, on which carbon nanostructures grow, is placed onto one of the electrode.

Another recently developed synthesis method has been reported to work at room temperature, by electrochemical deposition [35]; this method can be employed to produce a thin film of CNT from organic solvents, coating on the electrodes transition metal nanoparticles.

2.2.4 Growth Mechanism

Many mechanisms have been proposed over the years for the growth of carbon nanofilaments. Clearly, all the synthesis methods have a few points in common such as the carbon source and the way of activating that source. Most of them rely on the presence of metal catalysts. However the growth conditions in the arc, laser, and CVD environments are quite different and complex, therefore it is difficult to find one unifying model to describe the growth. The early model was developed by Baker and coworkers [36] and outlined in four main steps: (i) carbon-containing compounds adsorb dissociatively at the metal surface; (ii) carbon dissolves into the bulk of metal cluster; (iii) carbon diffuses through the bulk to the rear end; (iv) the carbon atoms are incorporated into a new graphene sheet of the growing nanofiber. A schematic representation of this process is depicted in Figure 2.7.

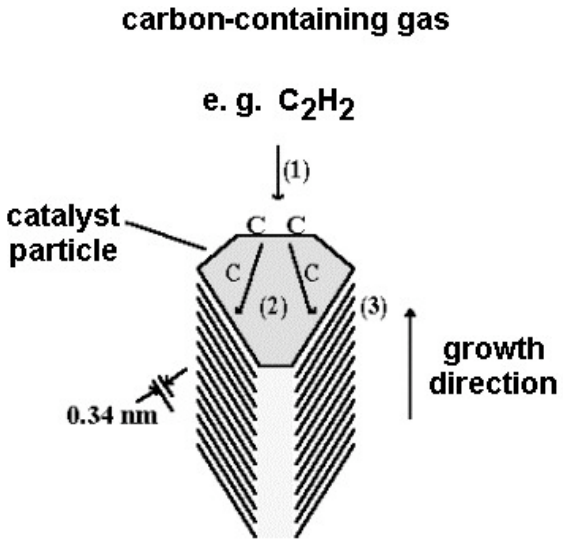

Figure 2.7: One-dimensional CNF growth model from a single metal nanoparticle.

The growth stops when the buildup of a carbon overlayer prevent further hydrocarbon decomposition. Generally, the rate determining step is believed to be the diffusion of carbon through the catalyst particle [37], indeed the activation energies for the growth were found correlated with those for diffusion of carbon through the corresponding metals (see Table 2.2).

Table 2.2: Activation energies for CNF growth from the metal catalyzed decomposition of acetylene, adapted from [38]

Catalyst	E_a for CNF growth [kcal/mol]	E_a for carbon diffusion [kcal/mol]
Nickel	34.7	33.0-34.8
α-iron	16.1	10.5-16.5
γ-iron	33.9	33.3-37.4
Nickel-iron	33.6	34.0
Cobalt	33.0-33.3	34.7

A metal carbide phase forms at the gas-particle interface, according to Sacco *et al.* [39]. Later Alstrup *et al.* suggested that this unstable carbide phase governs the growth of the nanofiber [40]. The supersaturation of the particle with carbon creates the concentration gradient required for diffusion. Some different models based on surface mediated carbon transport have also been proposed [41,42], because the energy barrier for such migration is lower than that for bulk diffusion [43]. Nevertheless, a very recent study of nucleation of CNT showed no evidence of surface diffusion of carbon [44].

According to the model based on the diffusion through the metal particle, two growth-mode have been identified: tip-growth, if the catalyst particle detaches form the support and is found a the tip of the fiber, and root-growth if the particle remains anchored to the support due to the strong interaction between them. This is also the reason why the diameter of the fiber is believed to be determined by the size of the associated catalyst particle [45]. Helveg *et al.* presented real-time images of the early stages of nanofiber tip-growth during the catalytic reaction between methane and supported Ni particles [46]. If the starting support on which CNF is either a metal foil or a powder, the diameters of the nanostructures vary over a wide range. In this case the mechanism of growth involves a first step of metal fragmentation in smaller particles, whose dimension is often unpredictable. This phenomenon was described by Jablonski *et al.* as a "surface break-up" necessary for the formation of CNF on metal foils [47]. They explained that the molar volume of the metal carbide is bigger than that of the corresponding metal, so the pressure generated between the grain boundaries can lead at the cracking of the metal surface in smaller particles. More recently, other groups observed this phenomenon while growing CNF on nickel foams [48, 49] and on nickel supported on carbon felt [50–52]. Ledoux and coworkers stressed on the fact that the final diameter of CNF is not dependent on the starting particle size of the catalyst, as shown in Figure 2.8,

and they rather invoked the octopus-like mechanism, firstly observed by Ermakova [53], leading to a web-like network of CNF.

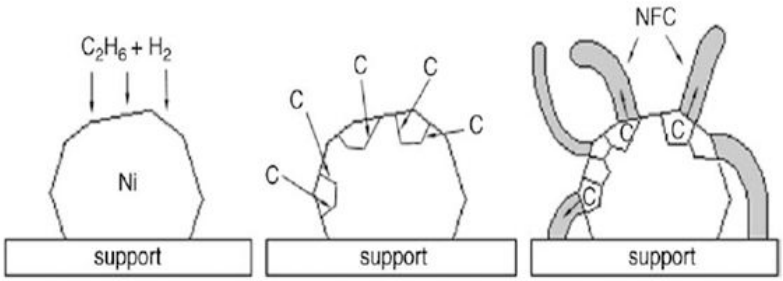

Figure 2.8: Growth mechanism proposed by Ledoux *et al.* for CNF formation from a single metal particle , involving metal fragmentation and reconstruction.

As already mentioned in 2.2.3, regardless the feedstock the most used catalysts for CNF growth are Fe, Co, and Ni and their alloys, due to their ability to diffuse carbon. Nevertheless the use of bimetallic or trimetallic mixtures with elements such as Mo, Ru and Pt have been reported to increase the yield under certain conditions [54, 55]. They can take any of three basic forms: bulk, supported, and vapor phase . Bulk metal can be employed in form of foil or powders. Supported metals are based on high surface area materials [56], and prepared by impregnation with a solution of the metal salt. Vapor-phase catalysts are generated by the release of volatile organometallic compounds, such as iron pentacarbonyl $Fe(CO)_5$, ferrocene $Fe(C_5H_5)_2$, or nickelocene $Ni(C_5H_5)_2$, along with feedstock gases into furnaces at high temperatures [57].

2.2.5 Properties and Applications

The unique properties of carbon nanofilaments make them suitable for many different applications [58–60]:

- very low electrical resistivities, in the order of the graphite ones: $\sim$ 1375 $\mu\Omega$·cm
- high thermal conductivities: $\sim$ 2000 W·m^{-1}·K^{-1}
- exceptional mechanical properties, Young modulus in the range of 400-600 GPa
- high specific surface area, up to 300-700 m^2·g^{-1}

- chemical stability and inertness

The application of CNF to composite materials development is mainly due to their mechanical properties. CNF can be used as reinforcement in fields such as aeronautics, civil engineering, or sport industry. Adding a 10 vol.% of CNF to a standard polymer can double its mechanical resistance and triple its elastic modulus [61]. The electronic properties of CNF allow applications in nanoelectronics or in fuel cell technology, such as electrodes in supercapacitators [62] or in fuel cells [63, 64], allowing to obtain higher power density. A controversial application of carbon nanostructure is the potential hydrogen storage, in the perspective of the use in on-board automotive applications [65, 66]. Since the inter-planar distance within the material is 0.337 nm, the sorption of molecular hydrogen (kinetic diameter of 0.289 nm) is enhanced thanks to to the short diffusion path. In addition, due to the weak (van der Waals) bonding of the platelets, the non-rigid nanopores can expand to accommodate hydrogen in a multilayer configuration. Nevertheless, it seems that currently none of the different storage solid state materials can reach the required storage densities for a hydrogen-powered vehicle [67, 68], so the interest for this application is loosing ground. The combinations of the physical and chemical properties together make possible to exploit the potential of carbon nanostructures as catalyst support. The features connected to this potential will be reported in much detail in 2.3, being this application the main subject of the herein reported thesis.

2.3 Carbon Nanofibers (CNF) for Catalytic Applications

2.3.1 Why CNF may be Suitable as Catalyst Support?

The majority of the industrial catalysts are based on supported metals. The main role of the support is to maintain the active phase dispersed and thus to provide a high surface area in order to host sufficient active sites per volume unit. Nevertheless, the interaction of the catalytic phase and the support can affect the activity, so the choice of the right support is crucial in the industrial process development. This choice is based on a series of desirable characteristics: inertness, stability under reaction and regeneration conditions, adequate mechanical properties, appropriate physical form for the given reactor, high surface area, porosity, and chemical nature. Following these directives carbon materials have been used since long time as catalyst supports [2, 69]. They show higher resistance to acidic/basic media than conventional oxide supports, they are stable at high temperatures (>1000 K), the chemical nature of the surface can be modified (e.g. to increase the hydrophilicity), and by burning away the carbon,

the precious metallic phase can be easily recovered. The main drawback to the use of active carbon materials in catalysis is their microporosity. In principle, internal mass transfer limitations are reduced by maximizing the porosity and minimizing the tortuosity of the catalytic system. Graphite, used as catalyst support, does not present this inconvenient and at the edge of each basal plane it shows a high concentration of unpaired electrons, who may play an important role for the chemisorption.

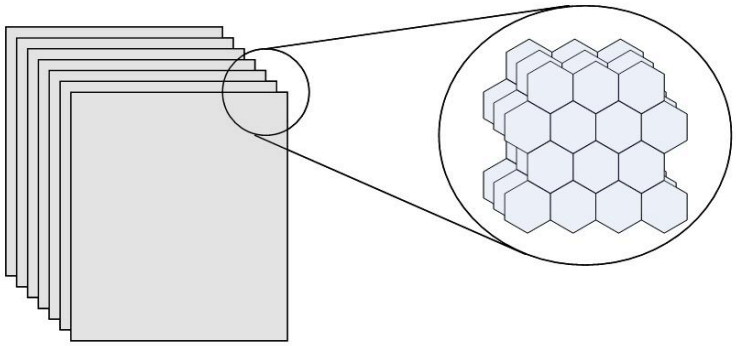

Figure 2.9: Schematic representation of graphite/CNF basal planes stacked together.

Although graphite is not extensively employed in catalysis due to its very low surface area, CNF are promising because they exhibit higher surface area, large pore volume and minimal or no microporosity. Several reviews dealing with this subject have been published [3, 27, 70, 71], proving the scientific interest around the potential of CNF as catalyst supports. The first group, who started the research on CNF as support for catalytic active phase, was probably the one of Baker in the nineties [72]. They supposed a strong interaction of the crystalline structure of the support with the metal clusters. According to this study, the metal particles would exhibit different adsorption strength and reactivity compared to those supported on less structurally ordered supports. Since then, Baker's group explored specific features of this material compared to other support media [73] or the influence of CNF structure on the catalytic behavior of supported metal particles [74, 75]. Other groups followed this research using carbon nanofilaments-based supports for metal catalysts: De Jong [51, 76], Geus [77], Ledoux [78] and Lefferts [49, 79] are maybe the most active in this field.

The most studied reactions on CNF-based catalysts are hydrogenations, both in liquid and gas phase [3]. Indeed, they are exothermic reactions which benefit of the good thermal conductivity of CNF. Many studies showed that catalysts supported on CNF exhibit higher activities and/or selectivities compared to the ones on traditional supports [73,75,78,80–84]. As reviewed by Serp *et al.*, besides hydrogenations other reactions have been investigated with CNF-supported catalysts, such as dehydrogenation, hydro-

formilation, hydrodechlorination, ammonia synthesis, hydrazine decomposition, hydrocarbons decomposition [3]. These examples underline the variety of fields where CNF can be successfully applied as catalytic supports, from processes of fine chemistry to environmental protection.

2.3.2 Modification of the Surface Chemistry of Carbon-based Supports

CNF exhibit an hydrophobic and inert nature, as well as graphite. For many applications it is suitable to chemically modify the surface to enhance the wettability by polar solvents such as water. In the perspective of supporting metal-containing species on CNF, some preparation methods, such as incipient wetness impregnation, ion-exchange, and organometallic grafting, require the surface functionalization. By treatment with strongly oxidizing media in gas or in liquid phase, oxygen-containing groups can be introduced on the surface of CNF [85, 86]. Since the edge sites of the graphene layers are much more reactive than the internal atoms, chemisorbed oxygen is predominantly located on the prismatic planes (Figure 2.9). The process of oxidation has also been related to the presence of defective sites in the graphene layers [87, 88].

The surface groups created by oxidative treatments are mainly acidic in character [89, 90]. They cause cation exchange properties, which can be useful when preparing metal supported catalysts from solutions containing cationic precursors. Furthermore, it has been demonstrated that prismatic planes, exposed by the CNF containing hydrophilic oxygenated surface groups, may interact and stabilize metal particles [91–93]. In Figure 2.10 a schematic representation of the possible surface groups on carbon is shown. They can be divided in four categories: strongly acidic groups (carboxylic and anhydride), weakly acidic groups (lactone and quinone), hydroxylic groups with phenolic characters, and carbonyl groups [89]. The number of oxygen-containing groups is highly dependent on the way of preparation. A critical survey of methods for determination of these groups is given by Boehm *et al.* [90].

- Titration methods are useful to determine the acidity of the groups;
- X-ray photoelectron spectroscopy (XPS) estimates the chemical composition of the few uppermost layer of the material, the characterization is performed by deconvolution of overlapping peaks in the O1s or C1s regions;
- Temperature programmed desorption spectroscopy methods (TPD) analyze the releasing of CO and CO_2 upon sample heating, indeed the groups decompose evolving gas at different temperatures;

- Infrared spectroscopy (IR) is used to differentiate the groups based on the chemical bond between carbon and oxygen (C=O, C-O, C-OH, etc.).

Despite the variety of the characterization methods, it became clear that individual methods are not capable to univocally identify the types of functional groups. IR spectroscopy is very difficult to interpret because of the strong IR absorption of carbon. The TPD technique, although widely used, has a high level of uncertainty. The desorption temperatures of the desorption peaks depend on the sample properties (e.g. pore size), the oxidation conditions, and the way TPD is carried out, in addition to the probability of secondary reactions of the evolved gases, especially in porous carbons. That is why the published TPD spectra differ widely. Lastly, in XPS, the differences in binding energy for different binding states are very small for an electronegative element like oxygen. The technique, in addition, requires calibration because of charging problems. Thus, the interpretation of results is normally not straight forward. Accordingly, the use of a single method is not recommended, but the combination of more than one technique can offer better understanding.

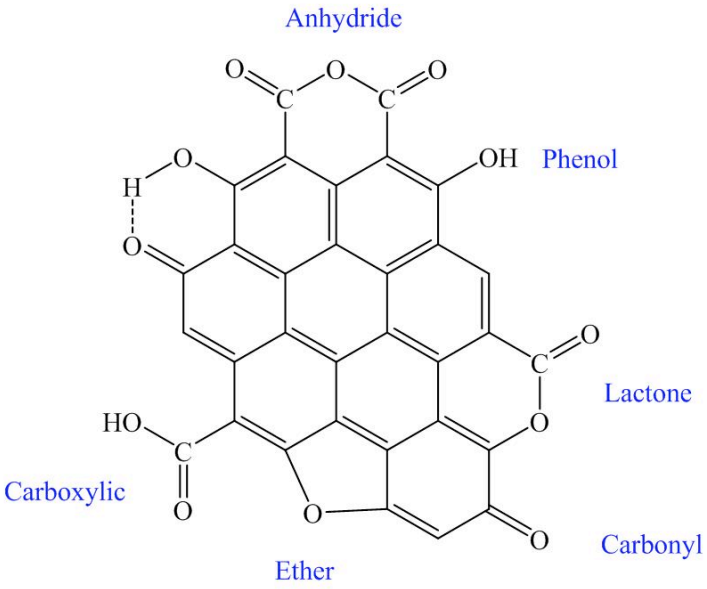

Figure 2.10: Surface groups on carbon after oxidative treatment.

Different studies have been carried out in order to investigate the effect of the surface oxidation of CNF [85, 86, 94, 95]. Ros *et al.* and Toebes *et al.* observed by XRD and TEM that the graphitic structure

of the CNF was maintained after oxidation. Nevertheless, the macroscopic structure of ribbon-like CNF was affected, while that one of herring-bone CNF remained intact. Both research groups demonstrated, with titration experiments, that the increase in the severity and in time of the oxidation results in an increase in the number of acidic surface sites.

2.3.3 Structured Catalysts based on CNF

CNF can be applied as catalysts supports in different ways. The most common is in form of small aggregates of fluffy powder, consisting of entangled CNF loaded with the catalytic active phase. Unfortunately, their use in this form in fixed-bed reactors gives rise to pressure drops and poses problems of handling. CNF can also form layers on structured materials (see 2.1.1), combining the advantages of carbon nanostructures and the easy handling of a macroscopic structure. In addition, diffusion distances become shorter and the hydrodynamic behavior of the reactor can be determined by the choice of the structured material [71].

One approach to build CNF-based structures supports is depositing active catalysts for the growth of CNF layers on macroscopic materials. Ledoux's group developed a CNF/graphite felt composite which was then used for supporting Ir for the hydrazine catalytic decomposition [50, 96, 97]. This reaction is highly exothermic and requires a catalyst working at high temperatures and having strong mechanical resistance. It should also transfer rapidly the heat avoiding hot spots formation. By applying the CNF-based catalysts mass and heat transfer limitations were overcome. A similar support was employed by Gangeri *et al.* as an alternative electrode for fuel cells [98]. In this case, Pt was supported on CNF grown on felt or cloth of carbon microfibers. The electrode assembled with the developed catalyst gave very low mass transfer losses. The cell performances were enhanced thanks to the good electron transport properties of the Pt/C interface. Research works, by Leffert's group, led to the development of a CNF/cordierite monolith support [48, 99], while De Lathouder *et al.* prepared CNF on monolith wash-coated with silica [100].

Figure 2.11: Typical structured material, ceramic monolith, felt and metal foam [71].

In order to avoid the step of depositing the catalyst for the growth of CNF on the structured support, the CNF can be synthesized directly on materials that are intrinsically active for the formation of CNF (containing elements like Fe, Ni and Co). Following this principle, Jarrah *et al.* prepared and characterized a novel material immobilizing CNF on the surface of Ni foam [49, 79]. The concept allows one to bypass a step in the CNF synthesis because the same metal catalyst for the CNF growth is the macroscopic support, which can be used directly in the reactor. However this structured catalyst has never been tested in a reaction. The material studied in the herein reported thesis was for the first time synthesized in our research group by Tribolet *et al.* [15]. It consisted of CNF grown on the surface of sintered metal fibers (SMF), which acted as catalyst and support at the same time. The macroscopic shape of the resulted composite is suitable for fixed-bed technology and the mesoporous structure created by the network of CNF improved the catalytic performance of the supported active phase. The support was firstly applied in the selective hydrogenation of acetylene on supported Pd-nanoparticles [84].

2.4 Supported Ionic Liquid Phase (SILP) Catalysis

2.4.1 Ionic Liquids (IL) in catalysis

Ionic liquids (IL) are salts which are liquid at ambient atmosphere and below 373 K. They have negligible vapor pressure and because of this they are sometimes referred as “green” solvents, due to their potential as alternative to volatile organic solvents (VOC) in industrial catalysis. They generally consists of a bulky, asymmetric cation and a smaller anion. The asymmetry of the system reduces the lattice energy of the crystalline structure and results in a low melting point salt. The first synthesis of IL is reported in 1914 [101], but it is just more recently that the scientific community started to be attracted

by the unique physical and chemical properties of this class of compounds. The most known series of IL is based on 1,3 -dialkylimidazolium cations and anions such as [PF_6] and [BF_4]; Hagiwara *et al.* compiled a detailed list of physical and chemical properties of IL relevant to their applications in synthesis and catalysis [102]. The properties of the IL depend on the nature and the combination of the ions which constitute them, so today a wide range of cations and anions have been investigated in order to tune the properties of the corresponding IL (Figure 2.12, [103]). Thanks to this synthetic flexibility it is nowdays possible to prepare functionalized IL which are "task-specific" and can be tailored to specific applications.

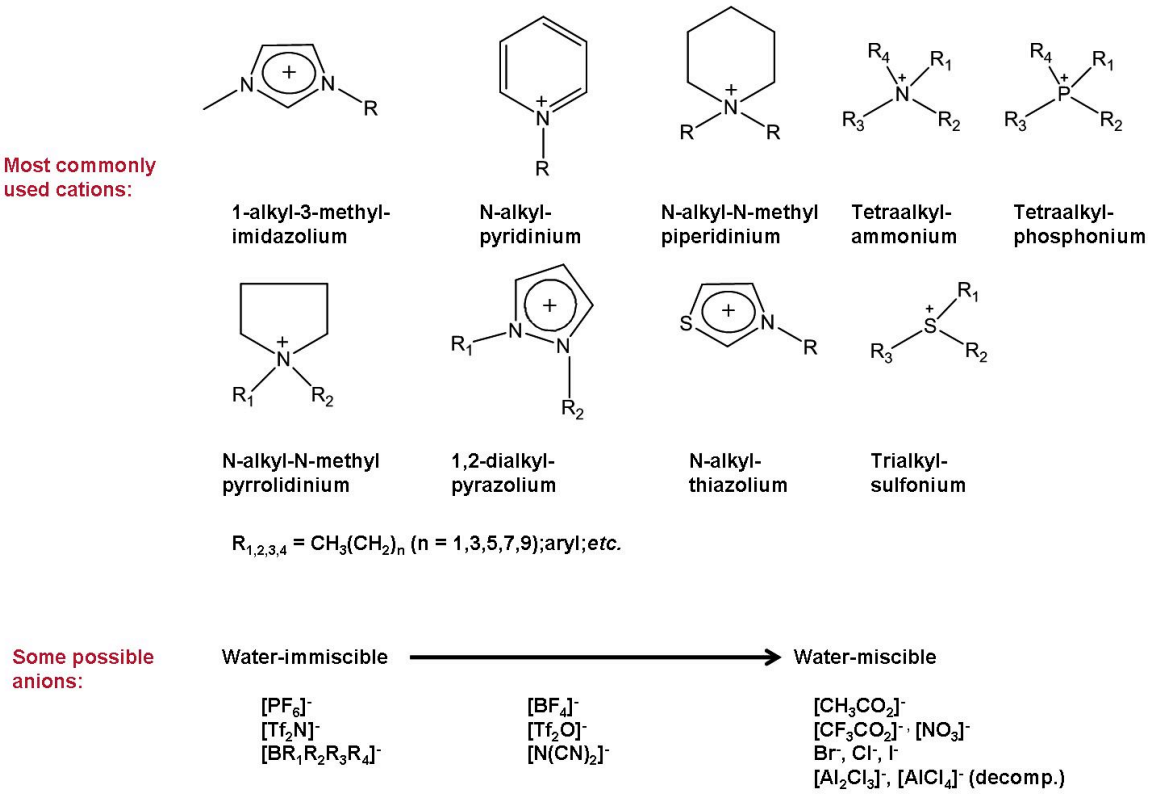

Figure 2.12: Some commonly used ionic liquid systems, adapted from [103].

In catalysis, IL are so attractive compounds because they provide a polar, but weakly coordinating medium for catalysts, substrates and products. Especially for transition metal catalysts in biphasic systems, IL are regarded as superior compared to water and common molecular solvents. They create, indeed, a non-nucleophilic environment which may increase the activity and the life-time of the catalyst. Nevertheless, in some cases they are not completely "innocent "solvents and they can participate to the

process acting as co-catalysts or as ligand sources [104]. The most common IL are also thermally stable in a large temperature range, melting below room temperature and starting to decompose above 523 K. Many catalyzed reactions have been reported in IL including hydrogenations, hydroformilations and C-C coupling reactions [105, 106]. Nevertheless some concerns arises regarding their toxicity [107], on which very little data are available, and their relatively high production cost. So, the commercialization of ionic liquid (e.g. Acros, Aldrich, Covalent Associates, Cytec, Merck, Sachem, Solvent Innovation and Strem) has been slow, despite the potential benefits described in scientific literature and related patents. At the present, there is only one known industrial process that employs IL on a commercial scale [108]. The so-called BASIL process uses N-methylimidazole to scavenge acid that is formed during the manufacturing of alkoxyphenylphosphine.

2.4.2 Metal Nanoparticles in IL and their Catalytic Applications

Transition metal nanoparticles have recently attracted increasing attention in scientific research and for industrial applications thanks to their large surface-to-volume ratio which drives for unique electronic and catalytic properties and provides a high amount of active sites per catalyst mass [109]. Colloidal methods using electrostatic and/or steric stabilization for tuning the nanostructure size and morphology are now widely used for the synthesis of metal nanoparticles [110, 111].

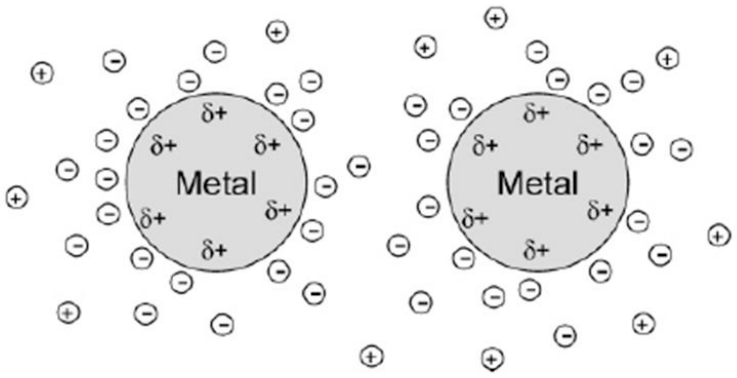

Figure 2.13: Schematic representation of electrostatic stabilization of metal colloid particles.

Imidazolium IL do not crystallize at room temperature, but they possess a particular structural organization due to their network of cations and anions [112, 113]. Thanks to this property they can be used

as "entropic" drivers for spontaneous and well-defined ordering of nanoscale structures, similarly to colloidal methods. Dupont and co-workers took advantage of this feature and discovered the potential use of imidazolium IL as template, stabilizer and solvent for the formation of transition metal nanoparticles [114, 115]. The interaction between the IL with the metal creates a protective layer composed of aggregate anions adjacent to the metal surface and imidazolium counter-ions which provide the charge balance [116]. Metal nanoparticles need this kind of protection because they are only kinetically stable, and the formation of bulk metal is thermodynamically favorite. The nanoparticles can be prepared by *in-situ* controlled reduction (with molecular hydrogen) of organometallic compounds, such as $Pd(acac)_2$, $Pt_2(dba)$, $RhCl_3$, $[Ir(cod)Cl]_2$ and RuO_2 dissolved in IL. They can subsequently be separated from the IL-phase and redispersed in different organic solvents or IL and used as active catalysts for various reactions [115]. The IL creates an electrostatic and steric stabilization which enables the formation of monodispersed sized nanoparticles and prevent the agglomeration of the latter in big and catalytically inactive clusters. The IL anions have the highest influence in the stabilization of the metal nanoparticles. Indeed, the particle size can be related to the molecular volume of the anion [116,117]. Furthermore, the catalytic properties have been found dependent on the nature of the anion, so when the anion is weakly coordinating, the nanoparticle surface is more exposed and the catalytic activity is enhanced [118]. The re-use without loss of activity of the IL synthesized and stabilized metal nanoparticles has also been demonstrated by Dupont's group. Although simple IL have a beneficial effect, sometimes it is envisaged the use of functionalized-IL which weakly coordinates to the nanoparticle surface and prevent agglomeration and leaching from the IL phase [119, 120].

2.4.3 Immobilization of IL on Solid Supports

The advantages of using IL as solvents for catalysts have been illustrated in 2.4.1, but critical issues, such as the easiness of separation from products and the reusability of the catalytic phase, have not been completely addressed when using liquid-liquid or gas-liquid biphasic systems. The concept of immobilization of the IL phase on solid supports has been investigated as alternative approach to pure biphasic systems. It facilitates the separation of catalysts from reaction mixtures and reduces the amounts of IL required, improving the economic viability of the process. The first application of this concept was realized by Chauvin and co-workers by supporting Lewis acid IL systems which were also the catalytically active species for the butene alkylation with isobutane [121]. They followed-up the approach used in the related field of supported aqueous phase catalysis [122, 123]. The immobilization or supporting of IL can be carried out in many different ways, such as simple impregnation [124], anchoring [125],

polymerization sol-gel method [126, 127] amongst others. Although the chosen route depends on the combination of IL and the support, the most straight-forward method is based on the impregnation of the support material with IL diluted with a molecular solvent, followed by the evaporation of the co-solvent, which results in a uniform and thin layer of IL phase.

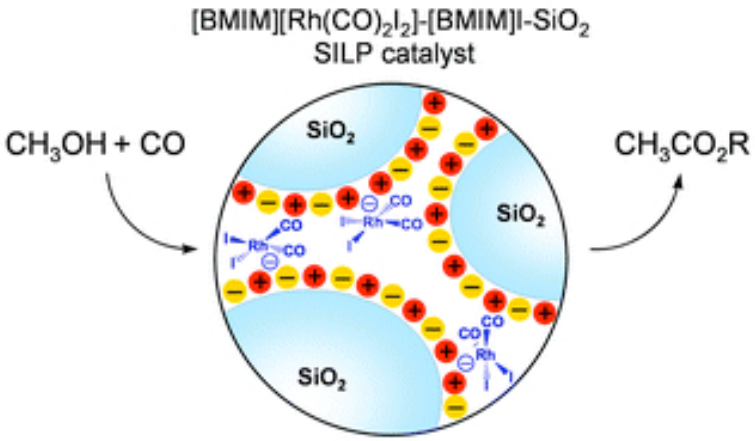

Figure 2.14: Schematic representation of a SILP catalyst [128].

The characterization of the resulting composite material with techniques which imply high-vacuum conditions is allowed by the non-volatility of IL. As a matter of fact, the scanning and transmission electron microscope can be used to observe the morphology of the catalyst, as well as X-ray photoelectron spectroscopy can be applied to get insights on the chemical composition at the surface.

The supported ionic liquid phase (SILP) can be applied in catalysis as active species itself [121, 129], as solvent for transition metal complexes [130–133], or containing metal nanoparticles [134, 135]. The use of SILP has been applied with success to a great range of different reactions covering Friedel-Crafts reaction [125], hydroformilation [124, 133], hydrogenation [126, 130], Heck reaction [136] and hydroamination [137].

2.4.4 Heterogenized Homogeneous Catalysts for Continuous Fixed-bed Reactors

Homogeneous catalysts based on transition metal complexes (TMC) are known to ensure high activity and selectivity because they generally provide only one type of active site. In terms of activity per metal center, homogeneous catalysts are thus preferable to solid state catalysts which present a multitude of different sites. The main drawback of homogeneous TMC is their use in industrial-scale continuous-flow synthesis. Indeed, they have to be both soluble in and separable from the reaction mixtures, while

heterogeneous catalysts form a distinct phase in the reactive environment. The success of homogeneous catalysts in many reactions has led to great interest in attaching the complexes to insoluble supports, thus facilitating the catalyst removal (via filtration/decantation) and reuse.

The SILP concept is most advantageous for continuous gas-phase reactions, where the combination of well-defined catalysts, non-volatile IL and solid, porous supports can enhance the process performance from an economical point of view, in terms of catalyst recovery and product separations. The process of confining the TMC dissolved in IL on the surface of a porous support is perceived as a "heterogenization" of the catalyst which enables its use in fixed-bed reactors, where the catalyst is stationary and the reactants pass over it. From a practical point of view this is the best configuration for the separation of products. Furthermore, the thermal stability of a heterogeneous catalytic system is generally higher, allowing better heat transfer under the reaction conditions (exo- or endo-thermic). In SILP catalysts the ability of dissolving the TMC is combined with the non-volatility and ensures the dissolution of the catalytic species also in continuously operated conditions. The concept has been proved very effective for gas-phase hydrogenations [130] and hydroformylations [5, 133, 138, 139], nevertheless the support nature can affect the activity of the TMC by irreversibly reacting with the ligands and deactivating the catalysts [139]. An ideal SILP catalytic system requires a porous support for the formation of the IL layer of the same size of the reactants diffusion layer. That is why the most employed supports are made of granulated materials. They provide high surface on which the IL can spread, but they can suffer from high pressure drop through the catalytic bed, an important issue that should be addressed in order to minimize the energetic requirement of the process.

2.4.5 Mass Transfer Limitations

Although the SILP concept has been conceived also to overcome the mass transfer limitation, in some cases the optimal utilization of the catalyst is not achieved. In gas-liquid systems, the transport of gaseous reactants to the catalyst is frequently the rate-limiting step [140]. The diffusion within the IL phase can thus affect the overall reaction rate. Although much effort is spent to eliminate the mass transfer to observe the true kinetics of the reactions involving gas and liquid phases, it is difficult to completely eliminate mass transfer effects in industrial reactor design. The high viscosity of IL can induce mass transfer limitations if the chemical reaction is fast. In that case the reaction takes place only within the narrow diffusion layer and not in the bulk of the IL. Thus, the catalyst dissolved in IL phase is only in part used. The challenge in this domain is to find the optimal thickness of the IL layer which does not compromise the homogeneity of the catalyst on the support and ensures the optimal mass transfer of

the reactive species to the catalyst. Few studies have examined mass transfer processes in IL [141, 142], in particular for hydrogenations. An understanding of mass transfer is of particular interest in IL due to the very low solubility of hydrogen in the media [143–145]. Nevertheless, in the majority of the cases the reaction rate is not limited by the transport from the bulk gas flow to the liquid interface (external mass transfer), but rather by the rate of the gas diffusion through the liquid film (internal mass transfer). This is particularly true when the catalysts is homogeneously dispersed in the IL phase (TMC or metal nanoparticles) and the reaction kinetics is fast, so the gaseous species react immediately as they diffuse into the thin IL film. The total flux of reactants through the IL phase is thus dominated by the diffusion term. If the IL film thickness approaches the size of the diffusion layer the productivity of the process is not limited by the mass transfer.

2.5 Selective Hydrogenation of Acetylene

2.5.1 Introduction

The bulk of the worldwide annual commercial production of polymer-grade ethylene is based on thermal cracking of petroleum hydrocarbons with steam. Ethylene predominates in the outlet stream of the process, but other hydrocarbons are present as impurities, such as paraffins, acetylenics and aromatics. Thus, further steps of refining are needed. In particular, the commercial specification for ethylene requires concentrations of acetylene lower than 10 ppm [146, 147].

The selective hydrogenation of acetylene is a key unit operation within the ethylene process. Indeed, traces of acetylene can poison the catalysts used for the downstream ethylene polymerization. The earliest studies of the acetylene hydrogenation coincided with the development of the petrochemical industry in the fifties, and concentrated mostly on the analysis of the product formed [148–150]. Given the large excess of ethylene in the feed, the main challenge is the complete hydrogenation of the acetylene with the minimum ethylene losses ($< 1\%$). Thus, the selectivity of the process is the key objective, requiring a careful choice and study of the catalytic system. The most used industrial catalysts are based on Pd, thanks to its high selectivity toward the semi-hydrogenations of alkynes (see 2.5.3).

There are two basic methods of refining ethylene streams from acetylene: the so-called tail-end and front-end processes. They differ in the location of the hydrogenation reactor within the scheme of the plant. In the tail-end method, the reactor is located after the de-ethanizer unit, so the inlet stream mainly consists of C_2-hydrocarbons. The addition of hydrogen in stoichiometric amounts is performed to ensure

an optimal concentration in the reactor feed. Sometimes small amounts of CO are also separately added, playing the role of selectivity moderator especially at high levels of acetylene conversion (see 2.5.3). In the front-end method, the reactor precede the de-methanizer in the process. Consequently, the feed contains typically 10-35 mol% of hydrogen, together with C_2- and lighter hydrocarbons. Higher H_2 inlet pressure can increase the acetylene removal rate and decrease the rate of the catalyst deactivation, but the most important selectivity to ethylene may decrease. Nevertheless, the development of very selective catalysts made the front-end to be the most adopted configuration in industry [151], because it has lower installation and operating costs. Pressure ranges typically from 20 to 35 bar and temperature from 298 to 373 K.

2.5.2 Main Reactions Mechanism and Selectivity

The network of main reactions involved during the acetylene hydrogenation is shown in Figure 2.15. The only desired reaction is the acetylene half-hydrogenation to ethylene, but further hydrogenation of ethylene to ethane may occur. Besides, the direct hydrogenation of acetylene to ethane can also take place [152] and a complex mixtures of $C_{x>2}$ compounds (C_{4+} commonly called "green oil") can be formed via the acetylene oligomerization. The high selectivity for oligomer formation (20-40 %) is a peculiar feature of acetylene, indeed with increasing substitution the oligomers formation is less favored due to steric interferences in the C-C bond forming step [153].

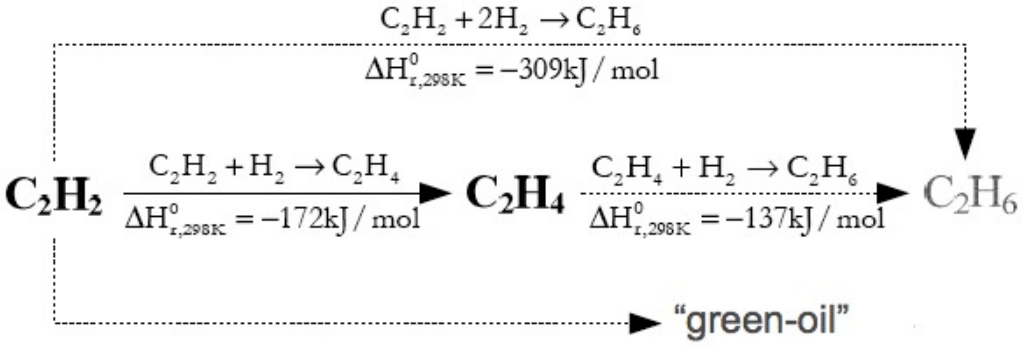

Figure 2.15: Network of main reactions proceeding during the acetylene hydrogenation.

The reaction kinetics is based on the sequential formation of C_2H_x species on the Pd surface, by addition of hydrogen atoms [154]. The complexity of this system is the reason of the slow progress in establishing a molecular mechanism for the process. Although the earliest kinetic models, reviewed by Bos *et al.* [155], did not consider the heterogeneity of the catalyst surface, today the most accredited

mechanistic scheme is the one elaborated by Borodzinski [156, 157]. It assumes the existence of specific types of active sites, created on the catalyst surface by carbonaceous deposits. Low hindered sites, accessible to all reagents, and poisoned parts coated by carbonaceous deposits which generate high hindered sites, may exist on Pd surface. It was proposed that on these high hindered sites only acetylene reacts because for steric reasons ethylene molecules cannot adsorb [158, 159]. A schematic representation of the catalytic surface is shown in Figure 2.16. The catalytic process may proceed via several parallel and sequential steps on the specific types of active sites. Although recently *in-situ* studies demonstrated the presence of carbonaceous deposits [160], the effect of the carbonaceous overlayer on the reaction is still very difficult to clarify [161].

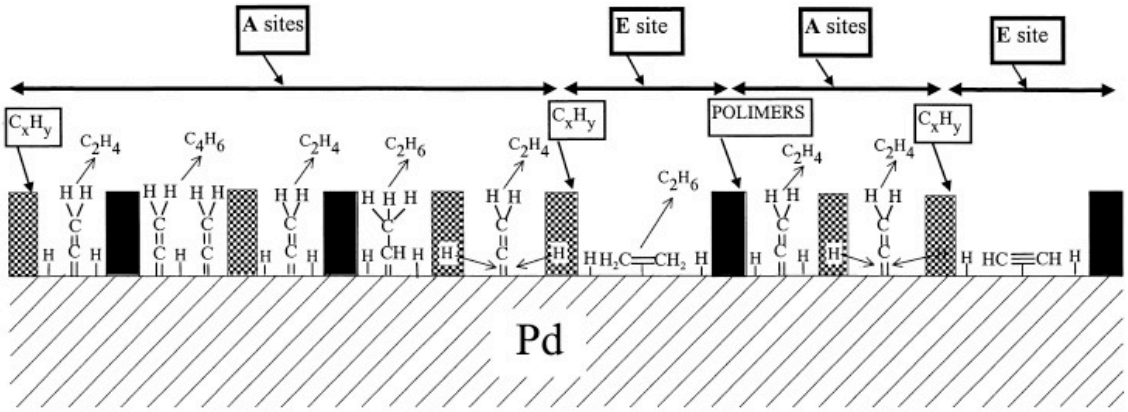

Figure 2.16: Simplified representation of active sites created at the catalyst surface by carbonaceous deposits (C_xH_y), adapted from [157].

For the intermediate half-hydrogenated product, two kinds of selectivity have been defined:

- Mechanistic selectivity, if the rate of ethylene production is much higher than that one of ethane production
- Thermodynamic selectivity, if the adsorption of acetylene is much stronger than that one of ethylene, thus limiting the re-adsorption of ethylene molecules and preventing the consecutive hydrogenation to ethane

Usually, over Pd the rate of half-hydrogenation and that one of the consecutive complete saturation of ethylene have the same order of magnitude. Thus, the selectivity is attributed to the thermodynamic

factor. Orders of reaction for alkynes hydrogenations on Pd are typically first or greater in hydrogen and zero or negative for the alkyne [162, 163]. Activation energies are frequently in the region of 60 $kJ \cdot mol^{-1}$, higher than for alkenes [162].

2.5.3 Catalytic Process: Focus on the Catalyst

For the selective hydrogenation of acetylene, supported Pd catalysts are mainly used due to their exceptional high activity and selectivity [155, 163]. Generally, low loadings of active phase are employed (about 0.01-0.1 %), in order to reduce the overall reaction rate and consequently the mass transfer limitations [147]. The selectivity of the process is improved and the risk of runaway avoided.

Metals from Groups VIII-X are active too, but much less selective than Pd [150, 164, 165]. The addition of Ag offers a good trade of small losses in activity for a large increase in selectivity [166–168]. Indeed, alloying Pd with different metals improve the selectivity by altering either its electronic or its geometric properties [169, 170]. Changing the electronic density of Pd may affect the relative adsorption strength of the reactants and intermediates. On the other hand, the second metal may block part of the surface, thereby affecting the geometry of the active sites.

In industrial reactors small amounts of CO are added to the feed gas, because CO is known to substantially improve the selectivity of the acetylene hydrogenation [155, 171]. One possible interpretation is that CO poisons the catalysts and adsorbs competitively with ethylene [172]. Other groups explained the CO effect in terms of competitive adsorption with hydrogen, rather than ethylene [154, 155]. Unfortunately the addition of CO may help reducing the production of ethane, but it has no effect on the production of the most harmful byproduct, the green-oil, which is responsible of the deactivation of the catalyst.

2.5.4 Carbonaceous Species Formation on the Catalyst Surface

The subject of oligomers formation is one of high commercial importance because it is the primary cause of the catalyst deactivation. On supported-Pd catalysts acetylene readily undergoes to polymerization. Thus, during its hydrogenation both gas phase oligomers and heavier hydrocarbons, so-called green-oil, are formed [173]. Surface oligomers, which remain on the catalyst, are frequently regarded as coke and act as a poison for the catalyst. About 25-30% of acetylene is converted to green-oil [173, 174]. Its formation is enhanced when many multiply-coordinated sites are present, since these favor the adsorption of acetylene as neighbors and consequently the polymerization of C_2 species on the catalytic

surface [175]. The addition of modifiers such as Si or TiO_2 may improve the lifetime of Pd catalyst, by decreasing the formation of green-oil [176, 177]. The modifiers are supposed to block the multiply-coordinated adsorption sites and to prevent the sintering of Pd crystallites, which can participate to the deactivation of the catalyst.

Upon aging and due to the green-oil formation also the selectivity to ethylene decreases [153, 173]. Larsson *et al.* postulated that two types of coke are deposited on the catalysts: "harmful" and "harmless" [178]. The first is formed at low hydrogen coverage of the Pd surface and it is responsible for the decrease in ethylene selectivity. The effect of hydrogen/acetylene ratio is still under discussion, but oligomers were not observed in the absence of hydrogen, which indicates that both hydrogen and acetylene take part in the oligomerization [179]. More recently, Ahn *et al.* demonstrated that 1,3 butadiene is the precursor for the formation of green-oil [180].

Industrially used catalysts are regenerated by burning off the green-oil in air; after a series of such cycles, the catalysts become inactive due to the sintering of Pd crystallites. The time between regeneration cycles is typically less than a year, sometimes several months.

Chapter 3

Experimental

3.1 CNF synthesis on Sintered Metal Fibers (SMF) Filters

3.1.1 Filters Characteristics and Pretreatment

The supports used for the preparation of structured CNF-based material were filters of sintered metal fibers (SMF) made of Inconel, provided by the supplier Bakaert Fibre Technology (Zwegem, Belgium): the characteristics are given in Table 3.1. The SMF are commercially available and industrially used in demanding applications where high porosity, high efficiency and long on-stream lifetime need to be combined to corrosion and temperature resistance. A typical application is process gas filtration, where minimizing the pressure drop is a challenge.

Table 3.1: Characteristics of sintered metal fibers (SMF) filters employed for the CNF synthesis.

Name	Material	Composition (wt %)	∅Fiber (μm)	Thickness (mm)	Porosity (%)
$SMF_{Inconel}$	Inconel 601	Ni: 60.5%, Cr: 23%, Al: 1.25%, Cu: 1%, Mn: 1%, Si: 0.5%, C: 0.1%, S: 0.0015%, Fe: balance	8	0.49	80

Before any use the filters were cleaned and calcined at 923 K for three hours in order to increase the roughness of the fiber surface and create the surface sites for the CNF growth. The SMF panels were subsequently cut in round disks of ∅ 24 mm. The specific surface area (SSA) could not be measured by the BET method, since the fibers are not porous. It could be roughly estimated as the geometric surface of the metal fibers.

3.1.2 Experimental Set-up (Feed-Reactor-Analysis)

The setup used for the CNF synthesis by chemical vapor deposition (CVD) of hydrocarbons assisted by hydrogen is depicted in Figure 3.1. It consists of two parts: feed and reactor. All tubing was stainless steel. The valves and connectors were supplied by Swagelok (Arbor Ventil+Fitting AG, Niederrohrdorf, Switzerland). The inlet gas Ar, H_2, C_2H_4, C_2H_6 (purity > 99.995%) were supplied by Carbagas (Lausanne, Switzerland). Gas flows were regulated by mass flow controller (MFC, Bronkhorst High-Tech B.V. Ruurlo, The Netherlands) and regularly calibrated using a soap-bubble flowmeter.

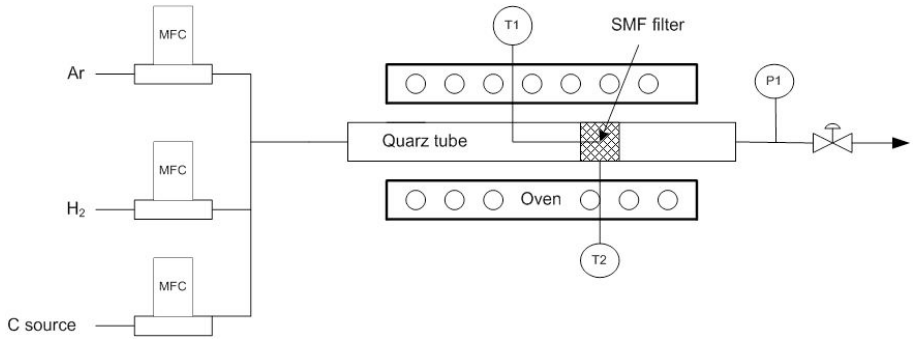

Figure 3.1: Experimental setup for the catalytic CNF growth on $SMF_{Inconel}$ by CVD of hydrocarbon precursors assisted by H_2.

The reactor was a quartz tube (650 mm in length and $\varnothing_{int}$24 mm) and the SMF disk was maintained in perpendicular position to the gas flow by means of two quartz slices ($\varnothing_{int}$ 23mm, 5 mm in length and 2 mm in thickness). The reactor was heated by a cylindrical oven (440 mm in length, type Ro 4/25, Heraus, Hanau, Germany) and the SMF disk was placed at two third of the oven length, so the gas flow was preheated before arriving to the filter. The oven temperature was controlled by a PID regulator (type 2404, Eurotherm Inc., Leesburg, USA) connected to a thermocouple, T_2 (type K, Thermocoax AG, Dietikon, Switzerland). The temperature inside the reactor was measured by a thermocouple T_1

protected by a quartz tube and it was placed in contact with the filter. The pressure inside the reactor was fixed at 1.25 bar by means of a downstream valve (type 44-2360-24, Tescom, Minneapolis, USA).

3.1.3 CNF/SMF$_{Inconel}$ Synthesis

The SMF$_{Inconel}$ were *in-situ* pretreated with 120 ml(STP)/min of H_2 in Ar (total flow 220 ml(STP)/min), the temperature was raised by 10 K/min at 873 K and kept constant for 2 hours. Afterwards the temperature was raised at the set-point for the CVD, which varied between 873 K and 973 K and the gas flow was switched to the standard reaction mix: C-source (C_2H_6 or C_2H_4) :H_2:Ar = 3: 17: 80 (total flow 600 ml(STP)/min). The reaction time was varied between 5 and 180 min. The reactor was then cooled down at $\sim$ 673 K with 120 ml(STP)/min of H_2 in Ar (total flow 220 ml(STP)/min) and then overnight till room temperature with 100 ml(STP)/min of Ar.

After the synthesis the resulting composite material was treated for 5 min with methanol in an ultrasonic bath to remove non-anchored carbon (< 0.5 wt.%) with a Bransonic ultrasonic cleaner (47 kHz and 30W, Branson Ultrasonic Crp., USA). The samples were eventually dried in vacuum (minimum 1 h) or in oven at 100°C (minimum 3 h).

3.1.4 CNF Surface Modification by Oxidative Treatments

CNF/SMF$_{Inconel}$ underwent different treatments in order to functionalize the CNF. In the first case the supports were activated in a 35% H_2O_2 boiling aqueous solution (Fluka, Buchs, Switzerland) for 4 hours and then washed with distilled water until neutral pH was attained. In the second case, the supports were treated for 30 minutes with plasma-generated O_3 formed in a dielectric-barrier discharge plasma reactor described in [181] from air flowing in the quartz tube. The O_3 concentration was monitored with an UV absorption monitor (API-450 NEMA) and after 30 minutes the output value was constant at 1100 ppm.

3.2 SILP Catalyst Preparation and Catalytic Testing for the Hydrogenation of 1,3-Cyclohexadiene

3.2.1 Supports Characteristics and Pretreatment

The supports used for the SILP catalysts were filters of SMF as described in 3.1.1, but made of different metals. Their characteristics are given in Table 3.2

Table 3.2: Characteristics of sintered metal fibers filters (SMF) employed for SILP catalysis.

Name	Material	Composition (wt %)	∅Fiber (μm)	Thickness (mm)	Porosity (%)
$SMF_{Inconel}$	Inconel 601	Ni: 60.5%, Cr: 23%, Al: 1.25%, Cu: 1%, Mn: 1%, Si: 0.5%, C: 0.1%, S: 0.0015%, Fe: balance	8	0.49	80
$SMF_{Fecralloy}$	FeCrAlloy	Cr: 20%, Al: 4.74%, Ni: 0.35%, Mn: 0.35%, Si: 0.35, Y: 0.3%, Cu: 0.15%, P: 0.035%, C: 0.03%, S: 0.01%, Fe: balance	20	0.3	71

Before any manipulation the SMF panels were cut into round disk of ∅ 12 mm and calcinated at 923 K for 3 h ($SMF_{Inconel}$) or at 1273 K for 12 h ($SMF_{Fecralloy}$). At such high temperatures, on Fecralloy fibers, aluminum diffused from the bulk toward the surface, generating a α-Al_2O_3 layer [182].

CNF were grown on $SMF_{Inconel}$ by decomposition of C_2H_6 as described in 3.1.3, while $SMF_{Fecralloy}$ surface was modified with a zeolite ZSM-5 coating (the details of the preparation were described elsewhere [14, 183]).

3.2.2 Rh-based SILP catalyst preparation

The following ionic liquids (IL) were employed for the preparation of Rh-complex based SILP catalysts:

- 1-butyl-3-methylimidazolium tetrafluoroborate, [bmim][BF_4], synthesized at LCOM (Laboratory of Organometallic and Medicinal Chemistry), EPFL.
- sulfonic modified 1-butyl-3-methylimidazolium triflate, [bmimSO_3H][CF_3SO_3], synthesized at LCOM (Laboratory of Organometallic and Medicinal Chemistry), EPFL.

- 1-butyl-3-methylimidazolium hexafluorophosphate, [bmim][PF_6], purchased from Alfa Aesar GmbH &Co KG, Karlsruhe, Gemany.

A mixture of IL (1.25 g), Rh complex bicyclo[2.2.1] hepta-2,5-diene-rhodium(I) chloride dimer, [Rh(nbd)-Cl]$_2$ (0.025 g), triphenylphosphine PPh_3 (PPh_3/Rh molar ratio between 2 and 12) in acetone was stirred and used to impregnate the structured supports. The dilution volume of acetone was chosen in order to obtain different SILP loading on the supports (between 2 wt.% and 12 wt.%). The active catalytic species were stabilized by adding 0.3-0.6 g of acid (HBF_4, 50% aqueous solution or H_3PO_4) to the solution before impregnation, whose color was observed to change from yellow to light orange. The SMF filters were submerged in the solution and then vacuum-dried at room temperature for 1 hour. The SILP loading was measured by difference of the support weight before the impregnation and after the acetone evaporation.

3.2.3 Experimental Set-up (Feed-Reactor-Analysis)

The experimental setup for the hydrogenation of 1,3-cyclohexadiene consisted in a jacketed tubular reactor with $\varnothing_{int}$ =12 mm connected to the inlet gases (for the description of tubing and feed see 3.1.2) and to the analytic part as shown in Figure 3.2. The catalytic bed in the form of ten slices of CNF/SMF$_{Inconel}$ supporting the IL phase catalyst ($m_{cat} \sim 900$ mg) was placed into the central part of the reactor perpendicularly to the gas flow. A fixed bed of glass beads was used to homogenize and preheat the flow of reactants upstream of the catalyst. The temperature was monitored with a thermocouple, protected by a quartz tube, inside the reactor and maintained constant by means of the heat exchanger oil circulating in the external jacket of the reactor.

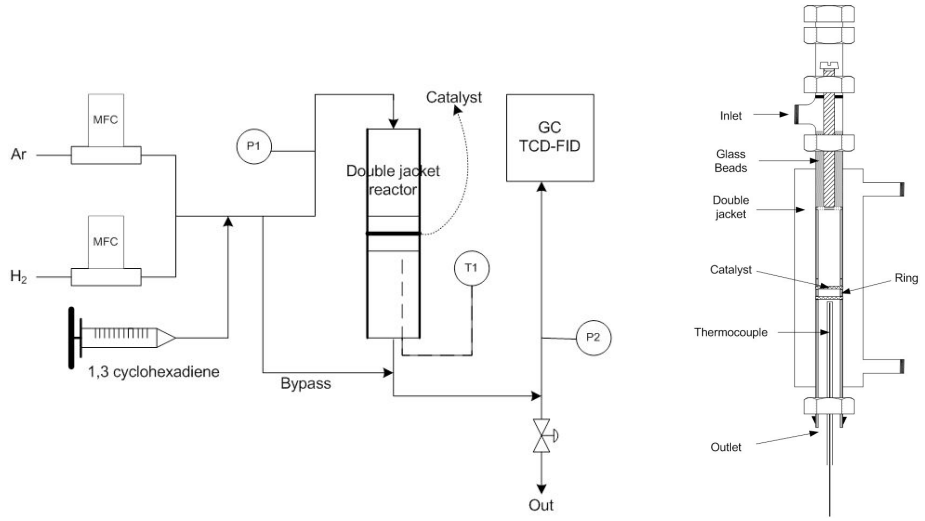

(a) Complete installation (b) Catalytic reactor

Figure 3.2: Experimental setup for the selective hydrogenation of 1,3 cyclohexadiene.

The mixture of 4 vol% of 1,3-cyclohexadiene, C_6H_8 (Fluka, Buchs, Switzerland) , 20 vol% of H_2 in Ar (total gas flow, 50 ml(STP)/min) was used throughout the study. At first, the flow was forced through the bypass in order to measure the initial concentrations of the reactants. The gas lines before and after the reactor were heated above the boiling point of the substrate and products (at $\sim$ 363 K) to prevent condensation. The substrate was fed in the reactor by means of a calibrated syringe pump and pre-heated in order to let it evaporate once injected into the tubing (vapor pressure 345.4 kPa, at 400 K [184]). The reaction mixture was analyzed on-line, within 6 hours, by gas chromatography (HP 6890, Agilent Technology AG, Switzerland) using a SPB-5 capillary column (Supelco, Fluka Holding AG, Switzerland) and a flame ionization detector. The conversion of 1,3-cyclohexadiene was calculated from the difference between the reactor inlet and outlet concentrations according to Eq.3.1:

$$X_{C_6H_8} = \frac{C_{C_6H_8-bypass} - C_{C_6H_8-out}}{C_{C_6H_8-bypass}} \tag{3.1}$$

The selectivity toward ethylene was calculated as the molar ratio of ethylene obtained to acetylene converted, the same for ethane:

$$S_{C_6H_{10}} = \frac{C_{C_6H_{10}-out}}{C_{C_6H_8-bypass} - C_{C_6H_8-out}} \tag{3.2}$$

3.3 Supported Pd Nanoparticles for the Selective Hydrogenation of Acetylene

3.3.1 Supports Characteristics and Pretreatment

The material used to support Pd nanoparticles was CNF/SMF$_{Inconel}$ synthesized by decomposition of C_2H_6, as described in 3.1.3. In order to elucidate the influence of the support nature on the reaction, the composite was also activated with two different oxidative pretreatments as described in 3.1.4.

3.3.2 Pd Nanoparticles Deposition from Colloidal Solution

Pd nanoparticles of ∅ = 8, 11, 13 nm were synthesized in water/aerosol OT/ isooctane microemulsion (AOT, sodium bis(2-ethylhexyl)sulphosuccinate sodium salt, an anionic surfactant) at a water-to-surfactant ratio of 4, 5 and 7, respectively. Figure 3.3 schematically represents the synthetic strategy for the preparation of structured catalysts with microemulsion-derived Pd nanoparticles.

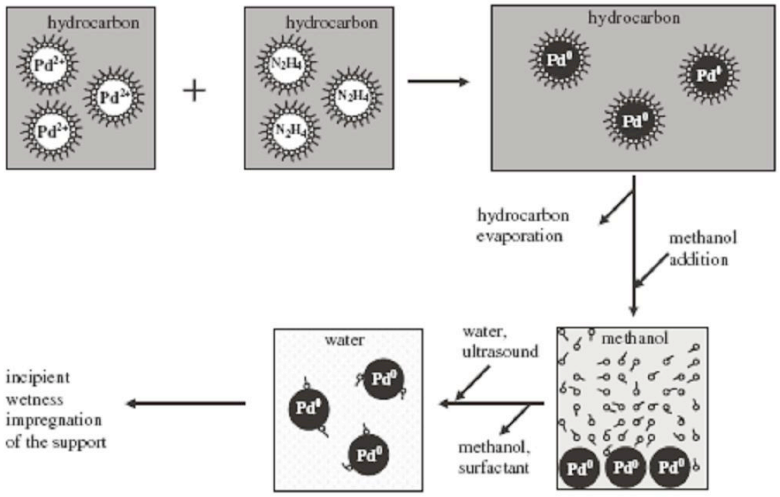

Figure 3.3: Scheme of the Pd nanoparticles preparation via a modified ME technique [185].

The aqueous solution of $PdCl_2(NH_3)_4$ (0.05 M) was used as metal precursor (pH 9 was adjusted with ammonia) and the 3 M solution of hydrazine hydrate as reducing agent giving hydrazine-to-Pd molar ratio of 60 to ensure the complete precursor reduction. The reverse microemulsion (ME) containing the metal precursor and the reducing agent was prepared by injecting the required amounts of the corresponding aqueous solution into 0.35 M isooctane solution of AOT and then mixed within few minutes

for the preparation of Pd nanoparticles. After 1 hour of reduction, the isooctane was evaporated in a rotary evaporator at 323 K and then methanol was added to remove the excess of the surfactant and to flocculate the nanoparticles. They were subsequently isolated by centrifugation and then redispersed in 12 ml of water by ultrasonic treatment for 20 min. The black colloidal solution was used to impregnate the CNF/SMF$_{Inconel}$ supports to give 0.18 wt.% Pd loading. The impregnated supports were then air-dried at 393 K.

3.3.3 Pd Nanoparticles Deposition by Ion Exchange

The deposition of Pd by ion-exchange was carried out by impregnation of CNF/SMF$_{Inconel}$ (previously activated in boiling H_2O_2) with a solution containing the metallic precursor. The support was submerged in a stirred aqueous solution of Na_2PdCl_4. The precursor was prepared mixing 1 equivalent of anhydrous $PdCl_2$ with 10 equivalents of NaCl (both from Fluka, Buchs, Switzerland) in 5 ml of bidistilled water and heated at 353-373 K. The excess of NaCl was needed to easily dissolve $PdCl_2$ and to guarantee the stability of the solution over time. Once the homogeneous solution was achieved , it was diluted at 100 ml with bidistilled water. The concentration of Pd(II) was set with respect to the quantity of carbon on the support. The final solution was brown-yellow colored, the sample was then submerged in the solution and a visible clearing of the color was observed along the deposition. After 5 hours of impregnation the sample was washed 3 times with distilled water and then dried at room temperature for 12 hours. The Pd loading was calculated by difference of concentration before and after the deposition (the washing water did not contain detectable traces of Pd) as described in 3.4.8.

3.3.4 Pd Nanoparticles Synthesis in SILP

The following ionic liquid (IL) were employed for the preparation of Pd-nanoparticles based SILP catalysts:

- hydroxyl modified 1-butyl-3-methylimidazolium bis(trifluoromethylsulfonyl) imide, [bmimOH]-[Tf_2N], synthesized at LCOM (Laboratory of Organometallic and Medicinal Chemistry), EPFL.
- 1-butyl-3-methylimidazolium hexafluorophosphate, [bmim][PF_6], purchased from Alfa Aesar GmbH &Co KG, Karlsruhe, Germany.

A mixture of IL and palladium acetylacetonate, Pd(acac)$_2$ (4 wt.% in IL), in acetone was stirred and used to impregnate the CNF/SMF$_{Inconel}$. The dilution volume of acetone was chosen in order to obtain

different SILP loading on the supports (between 3 wt. % and 9 wt.%). The filters were submerged in the solution and then vacuum-dried at room temperature for 1 hour. The SILP loading was measured by difference of the support weight before the impregnation and after the acetone evaporation. The Pd precursor in [bmim][PF_6] was reduced to nanoparticles at 423 K, 1 atm and overnight, with 30 vol.% H_2 in Ar (total flow 150 ml(STP)/min) . The reduction of $Pd(acac)_2$ in [bmimOH][Tf_2N] was carried out at 423 K under Ar flow (100 ml(STP)/min) overnight, without the addition of external reducing agents.

3.3.5 Experimental Set-up (Feed-Reactor-Analysis)

The experimental setup for the hydrogenation of acetylene consisted in a jacked tubular reactor with $\varnothing_{int}$ =12 mm connected to the inlet gases and to the analytic part as shown in Figure 3.4. The catalytic bed in the form of two slices of CNF/SMF$_{Inconel}$ supporting Pd nanoparticles ($m_{cat} \sim$ 180 mg) was placed into the central part of the reactor perpendicularly to the gas flow. A fixed bed of glass beads was used to homogenize and preheat the flow of reactants upstream of the catalyst. The temperature was monitored with a thermocouple, protected by a quartz tube, inside the reactor and maintained constant by means of the heat exchanger oil circulating in the external jacket of the reactor.

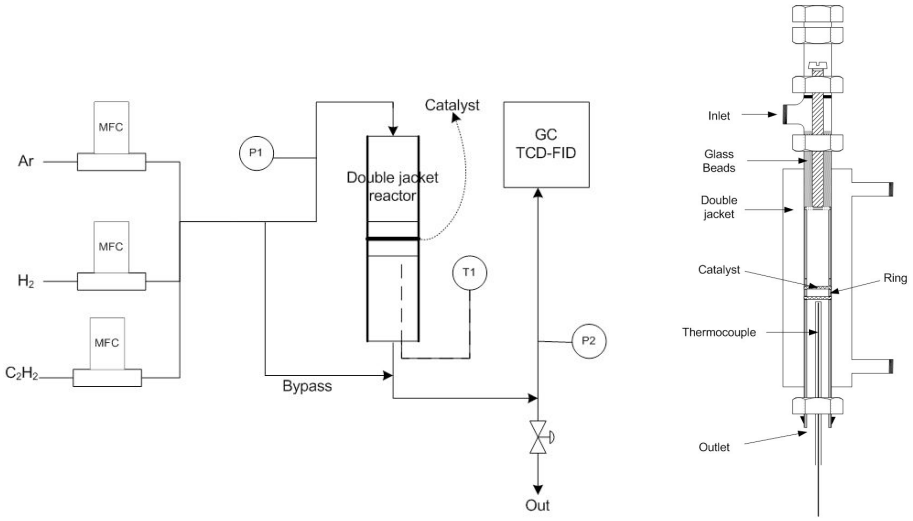

(a) Complete installation (b) Catalytic reactor

Figure 3.4: Experimental setup for the selective hydrogenation of acetylene.

At first, the flow was forced through the bypass in order to measure the initial concentrations of the reactants. During the reaction the pressure was maintained at 1.04 bar. Products were monitored, within 6 hours, on-line by gas chromatography (HP 6890, Agilent Technology AG, Switzerland) using a Car-

boxen 1010 (Supelco, Fluka Holding AG, Switzerland) capillary column; the carrier gas was He and a flame ionizator and a thermal conductivity detectors were used for monitoring the gas mixture, the analysis was repeated every 10 min on-stream.

The conversion of acetylene was calculated from the difference between the reactor inlet and outlet concentrations according to Eq.3.3:

$$X_{C_2H_2} = \frac{C_{C_2H_2-bypass} - C_{C_2H_2-out}}{C_{C_2H_2-bypass}} \tag{3.3}$$

The selectivity toward ethylene was calculated as the molar ratio of ethylene obtained to acetylene converted, the same for ethane (Eq.3.4 and 3.5):

$$S_{C_2H_4} = \frac{C_{C_2H_4-out}}{C_{C_2H_2-bypass} - C_{C_2H_2-out}} \tag{3.4}$$

$$S_{C_2H_6} = \frac{C_{C_2H_6-out}}{C_{C_2H_2-bypass} - C_{C_2H_2-out}} \tag{3.5}$$

Since only C_2H_2, C_2H_4, C_2H_6 and Ar were detected at the outlet, it was supposed that the carbon transformed in the reactor but not detected by gas chromatography was the product of the oligomerization deposited on the catalytic bed. The selectivity to green-oil was thus calculated from the mass carbon balance as the complement of the sum of the previous two, according to Eq. 3.6:

$$S_{C_{x>2}} = 1 - S_{C_2H_4} - S_{C_2H_6} \tag{3.6}$$

The following assumption were made for the catalytic fixed bed reactor:

- Plug flow hydrodynamics
- Thermodynamics of gas assumed equal to pure Ar (diluted reactive mixture)
- Negligible pressure drop
- Ideal gas law

In order to compare the performances of different catalysts the catalytic reactor was operated under differential conditions, where the reaction rate is identical in every point of the reactor if the conversion is kept low. The reaction rate -$R_{C_2H_2}$ is thus calculated from the mass balance of a plug-flow reactor:

$$d\left(\frac{m_{cat}}{F_{C_2H_2-in}}\right) = \frac{m_{cat} \cdot \tau}{V_R \cdot C_{C_2H_2-in}} d\tau = \frac{dX_{C_2H_2}}{-R_{C_2H_2}} \tag{3.7}$$

$$\frac{dX_{C_2H_2}}{d\tau} = \frac{m_{cat} \cdot (-R_{C_2H_2})}{V_R \cdot C_{C_2H_2-in}} \tag{3.8}$$

For the system used through this study instead of the residence time of the gas in the catalytic bed, it was used a modified residence time τ' calculated according to Eq. 3.9 and corresponding to the time of contact of acetylene on the catalyst as a function of the catalytic mass and of the volumetric flow of acetylene:

$$\tau' = \frac{m_{cat}}{Q_{C_2H_2-in}} \tag{3.9}$$

Eventually, the reaction rate was obtained as the ratio between the difference of the acetylene concentration and the time of contact of the gas in the reactor:

$$-R_{C_2H_2} = \frac{C_{C_2H_2-in} - C_{C_2H_2-out}}{\tau'} \tag{3.10}$$

For the hydrogenation of acetylene in ethylene-rich streams the experimental setup was slightly modified (Fig.3.5), adding a line from the C_2H_4-MFC to the reactive mixture feed.

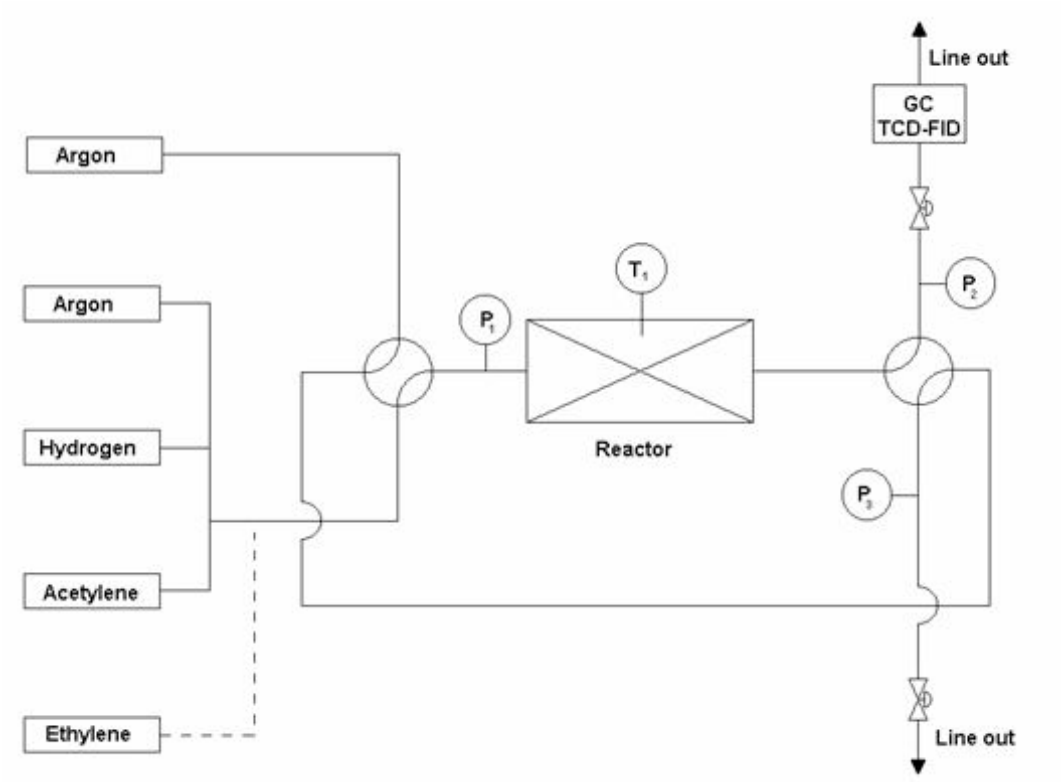

Figure 3.5: Experimental setup for the selective hydrogenation of acetylene in C_2H_4 -rich stream.

3.4 Characterization Methods

3.4.1 BET

The specific surface area (SSA) and the porosity of the supports were measured by nitrogen adsorption-desorption at 77K with a Sorptomatic 1900 instrument (Carlo-Erba, Milan, Italy). The SSA was calculated by the method of Brunauer-Emmet-Teller (Brunauer *et al.* , 1938), which takes multilayer adsorption into account. The pore volume and the pore distribution was determined by the Dollimore-Heal method (Dollimore & Heal, 1964).

3.4.2 Scanning Electron Microscopy (SEM)

Scanning electron microscopy (SEM) was generally employed to study the morphology of the CNF deposit, as well as the IL coatings of the supports. The microscope employed was a JSM-6300F (JEOL ltd, Tokyo, Japan and Philips XL 30SFEG, The Netherlands) operated at voltage of 5-10 kV.

3.4.3 High-Resolution Transmission Electron Microscopy (HRTEM)

High Resolution Transmission Microscopy (HRTEM) was used to study the morphology of CNF and Pd nanoparticles synthesized. The system used was a CM300UT FEG (Philips, Amsterdam, The Netherlands) equipped with a energy dispersive X-ray (EDX) analyzer.

3.4.4 Temperature Programmed Oxidation (TPO)

Carbon deposits on $SMF_{Inconel}$ were characterized by temperature programmed oxidation (TPO) in the Micromeritics AutoChem 2910 analyzer provided with a quartz plug-flow reactor, a scheme of the setup is shown in Figure 3.6. The gas-analysis at the outlet was done on-line with a quadrupole mass spectrometer, MS (ThermoStar-200, Pfeiffer Vacuum Technology AG, Berlin, Germany). The samples were exposed to a flow of 2 vol% O_2 in He during a temperature increase (20 ml(STP)/min, ramp rate 10 K/min from room temperature up to 1373 K). Previous to the TPO run the reactor was purged with He for 30 min at room temperature.

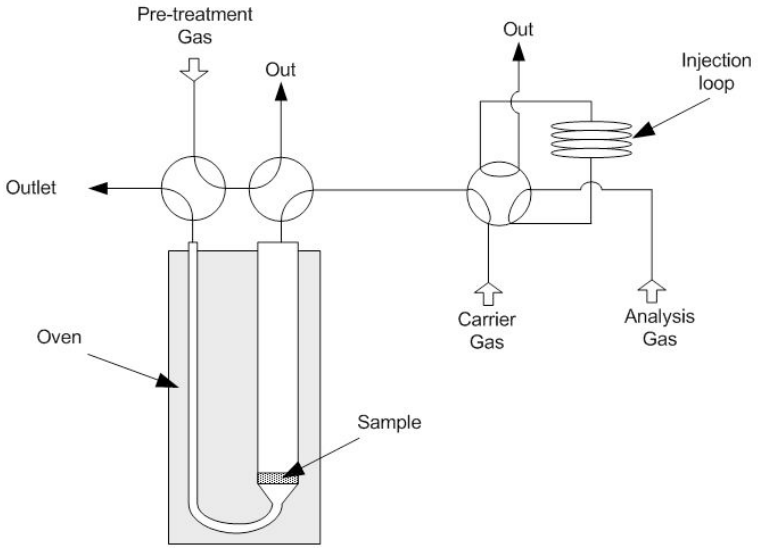

Figure 3.6: Scheme of the Micromeritics AutoChem 29100 system.

TPO characterize the carbon deposits based on their oxidation reactivity, which is closely related to the structural morphology of the deposits. Generally in the TPO profile multiple CO_2 peaks can be distinguished, reflecting the presence of both less ordered as well as highly ordered carbon deposits. The position of the peak of CO_2 in the TPO profiles for the samples studied was used as a reference for comparing the degree of cristallinity of CNF synthesized on $SMF_{Inconel}$.

3.4.5 Temperature Programmed Desorption (TPD) of CO and CO_2

The functional groups formed by oxidative treatment of $CNF/SMF_{Inconel}$ were characterized by temperature programmed desorption (TPD) in He (20 ml(STP)/min from room temperature up to 1273 K) using a a Micromeritics AutoChem 2910 described in 3.4.4. The amounts of CO and CO_2 desorbed were monitored with a quadrupole mass spectrometer, MS (ThermoStar-200, Pfeiffer Vacuum Technology AG, Berlin, Germany), calibrated using gas mixtures of known composition. Previous to the TPD runs the reactor was purged with He for 30 min at room temperature. The profile of both gases produced were integrated over time and the results were used for a qualitative and quantitative characterization of the carbon surface functional groups.

Step-wise TPD coupled with XPS measurements were carried-out with a different set-up, at the premises of the Fritz-Haber-Institut (FHI) of Berlin. The system is described in detail in 4.4.3.

3.4.6 X-ray Photoelectron Spectroscopy (XPS)

X-ray photoelectron spectroscopy (XPS) performed with an AXIS Ultra ASCA (Kratos, Manchester , UK) was employed to determine the chemical composition of the surfaces. The measures were performed using a monochromatic Al-Kα radiation.

3.4.7 X-ray Diffraction (XRD)

X-ray diffraction (XRD) was used to study the ME-synthesized Pd nanoparticles crystallinity and size. Spectra were acquired on a D500 Siemens powder diffractometer (Munich, Germany) in a 2θ range of 35-90°, using a monochromatic Cu-Kα radiation source (λ = 0.15405 nm). The angle was varied with a step size of 0.04° and a step time of 4 s. For calculating the Pd particle size, the Scherrer equation was used.

3.4.8 Atomic Absorption Spectroscopy (AAS)

The wt.% of Pd on the catalysts synthesized by ion-exchange with Na_2PdCl_4 was determined by the analysis of the residual Pd content of the aqueous solution after the deposition. The analysis was performed by atomic absorption spectroscopy (AAS) at 246 nm on a Shimadzu AA-6650 spectrometer with an air-acetylene flame.

3.4.9 CO Chemisorption

CO chemisorption was used to calculate the dispersion of Pd nanoparticles deposited on CNF/SMF$_{Inconel}$. This method was performed in a Micromeritics AutoChem 2910 described in 3.4.4. The CO concentration at the outlet was monitored by means of a thermal conductivity detector (TCD), calibrated using mixtures of known composition. The ratio Pd/CO used to calculate the dispersion and the particle size is 5/3.

3.4.10 Nuclear Magnetic Resonance (NMR)

NMR spectroscopy was carried out to provide insight into the nature of the homogeneous catalytic species in the IL phase and for determining the gas solubilities in [bmim][PF_6]. All the measurements were performed under oxygen-free conditions using standard Schlenk techniques with N_2 protective

gas. Medium-pressure sapphire NMR tubes were employed [186, 187]: this type of NMR tubes can be pressurized up to at least 150 bar, and measurements can be carried out with spinning samples. The *in-situ* studies of processes under pressure are allowed with good on-line resolution. ^{1}H, ^{13}C and ^{31}P NMR spectra were recorded on a Bruker DRX 200 NMR spectrometer. The spectra were fitted with WINNMR, GNMR 4.0 and NMRICMA/MATLAB programs on a PC (nonlinear least squares fit to determine the spectral parameter and the differences between measured and calculated spectra minimized).

Chapter 4

Development of CNF/SMF$_{Inconel}$ Structured Supports

4.1 Introduction

Carbon nanofibers based materials (CNF) received increasing interest in catalysis, because they form aggregates with high surface area (100-200 m^2/g) and high pore volume (0.5-2 cm^3/g), without the presence of micropores [3, 27]. In order to take advantage of the excellent thermic, mechanic and electrical properties of CNF (see 2.2.5) in heterogeneous catalysis, structured supports with immobilized CNF on the surface have been recently synthesized and applied in gas and liquid media. Growing CNF directly on metal grids, foams or fibers resulted in a very versatile structured material for catalytic applications [15, 49, 84]. The use of metals, which are active catalysts for the growth of CNF (Ni, Fe, Co), allows to obtain the composite support in a one-step synthesis, without previous catalyst deposition or further purification. With the CNF synthesized directly upon the support material to be used for catalytic application, the processes of dispersal and reattachment of CNF to support materials become unnecessary. The previous research activity, carried out by Tribolet [4], to deposit CNF on sintered metal fiber (SMF) filters resulted in a composite material with a uniform CNF layer strongly anchored the metal surface. The objective of the study described in this Chapter was to follow-up this research effort, in order to optimize the synthesis and the characterization of CNF/SMF. A comparative study between two different carbon precursor was therefore conducted, the mechanism of growth of CNF was better elucidated and a new method of functionalization of the surface of CNF was applied. For the first

time, functionalized CNF were characterized by step-wise heating in a UHV chamber, with a coupled TPD and XPS method.

4.2 Chemical Vapor Deposition (CVD) Synthesis of CNF on SMF$_{Inconel}$

The SMF$_{Inconel}$ filters were at the same time support and catalyst for the growth of CNF, but two different pretreatment steps were necessary prior to the synthesis of CNF on their surface. First of all, the filters were calcinated: the oxidation of the metal surface increased the roughness, creating surface break-ups and cracks which were useful for generating the catalytic sites needed for the CNF synthesis. Metal oxides formation induced significant surface fracturing, with many features exhibiting an increased density of crystal defects [188]. After the oxidation step the filters were reduced *in-situ*, in order to have the catalytic sites in their metallic form Me^0. Upon reduction the catalyst nucleation is relegated to surface defects and grain boundaries, proving the benefit of the prior oxidation step to have a uniform catalytic layer on the surface.

The metal particles on the surface are involved in the formation of CNF from the decomposition of a carbon precursor at high temperature. Most probably the relatively large metal particles are fragmented further during the CVD. Initially carbon is deposited from the carbon precursor decomposition on the metal surface, then it diffuses into the metal grains and precipitates at the grain boundaries (see 2.2.4). Due to the mechanical stresses induced by the carbon, the metal grains are fragmented and CNF start to grow.

4.3 Carbon Precursor Comparison: Ethane or Ethylene

The nature of the carbon precursor for the CVD is one of the most important parameters of the synthesis, because it influences the morphology and the structure of the CNF grown on SMF$_{Inconel}$. During this work, ethane and ethylene were chosen as carbon precursors and compared because from a preliminary screening both provided stable and homogeneous CNF deposits [4]. The comparison is furthermore interesting, due to the difference in reactivity of the two hydrocarbons. Synthesis temperature and time were varied, in order to optimize the CNF synthesis.

Table 4.1: Summary of the experimental conditions and yield for the CNF formation on SMF$_{Inconel}$, C-source :H_2:Ar = 3: 17: 80 (total flow 600 ml(STP)/min).

C-precursor	*T range[K]*	*t range[min]*	*C yield [wt.%]*
ethane	873-973	10-240	0.12-20.5
ethylene	873-973	15-60	7.3-52.2

4.3.1 CNF Yield and Synthesis Temperature

The morphology of the CNF/SMF$_{Inconel}$ composite, after synthesis at 923 K, observed by SEM is presented in Figure 4.1. The whole surface of the starting Inconel fibers is covered by a dense network of CNF with different diameters. The CNF are highly entangled with diameters in the range of 50-200 nm and lengths up to several microns. Metal particles can be seen on the top of the single CNF. The macrostructure of the filter is nevertheless maintained, as well as the porosity of the composite. Since ethylene is much more reactive than ethane, the thickness of the layer and the length of CNF dramatically increased when ethylene was employed (Figure 4.1 C). Indeed, the yield of carbon (as the ratio between carbon weight and SMF weight) from ethylene is almost ten times higher at this synthesis temperature (see Figure 4.2).

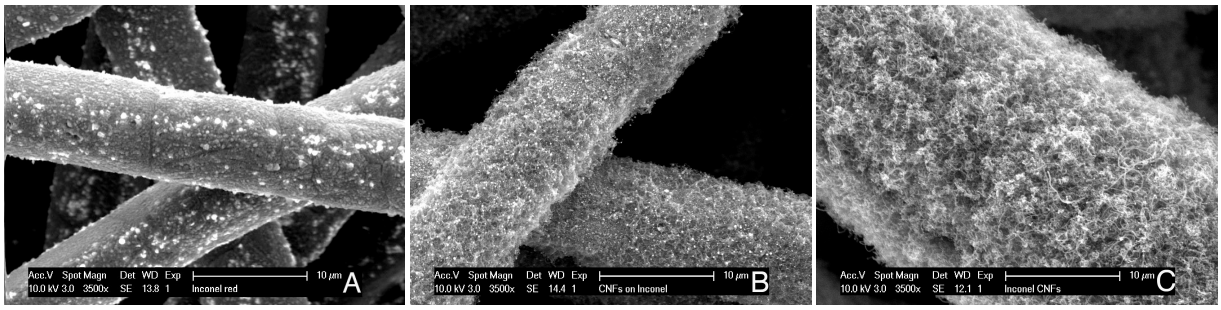

Figure 4.1: SEM micrographs (3500x) of: A) SMF$_{Inconel}$ oxidized, B) CNF/SMF$_{Inconel}$ from ethane CVD at 923 K for 1 hour, C) CNF/SMF$_{Inconel}$ from ethylene CVD at 923 K for 1 hour.

Figure 4.2 shows how the carbon yield on the SMF$_{Inconel}$ increased with the synthesis temperature for both the precursor employed. As already observed from the morphology of the CNF deposits in Figure 4.1, the faster ethylene decomposition resulted in higher carbon yield at the same temperature compared to the ethane decomposition.

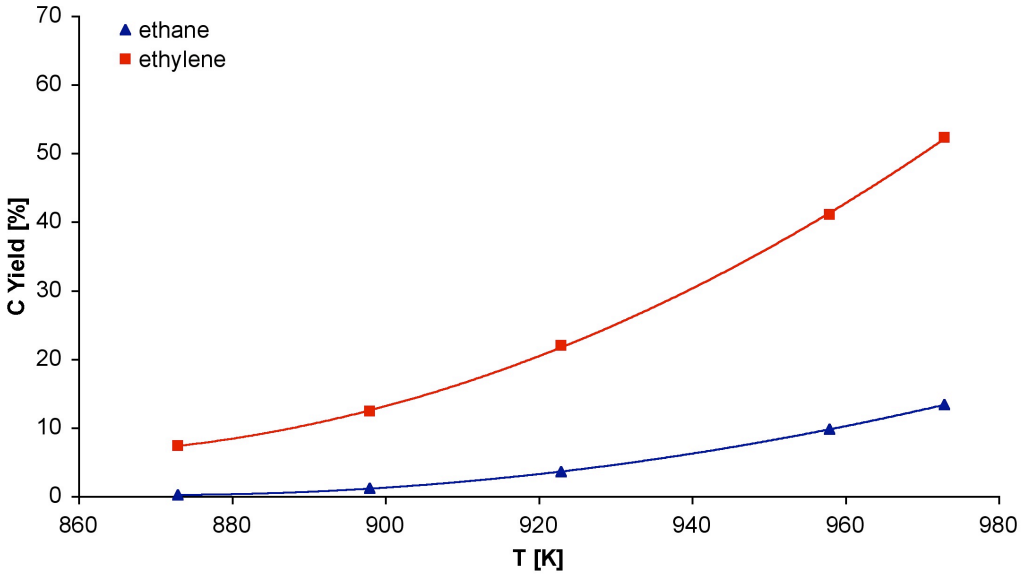

Figure 4.2: Carbon yield of 1 hour-CVD on SMF$_{Inconel}$ as a function of synthesis temperature: (▲) ethane and (■) ethylene

The same carbon yield from ethane CVD at 958 K could be obtained by ethylene decomposition at 873 K. Since the morphology of the CNF layer didn't change except for the thickness, ethylene CVD is energetically favorable compared to ethane CVD. Interestingly, no saturation phenomenon could be observed with increasing the synthesis temperature until 975 K.

4.3.2 Synthesis Time and CNF growth

To get a better insight on the growth mechanism SEM images were taken after 5, 10 and 60 minutes of ethane decomposition. The thickness of the CNF layer varied following the C yield on the filter. After 5 min of reaction the metal fiber presented a rougher surface, due to the carbon deposition and accumulation to the grain boundaries (Figure 4.3 A). A closer look to the surface at this stage is shown in Figure 4.4-A: the metallic surface is seen fragmented in small particles and clearly CNF started to grow lifting the catalytic particle up, but itself remaining attached to the original structure, probably *via* the penetration of the CNF into the Inconel fiber. The catalytic particles had been expelled from the crystalline units because of the stress forces brought about by dissolution of large amounts of carbon. This mechanism is very similar to the octopus-like formation described by Louis *et al. [189]*. In the herein reported case the graphitic planes likely originated from more than one monocrystalline region,

due to which many defects are built in, causing the variable diameter and roughness of the CNF. The Inconel fragmentation in sub-particles is obviously not a homogeneous process, because it depends on the composition of the alloy and on the size of the original grains on the surface. Indeed, after 10 min of reaction the CNF layer is not homogeneous on the metal fiber (Figure 4.3 B), showing some zones where the CNF have grown and entangled and others where the metallic surface is clearly visible and not yet covered by CNF. After 60 min of reaction, the CNF layer is complete and the Inconel surface is totally covered by the mesoporous structure created by the CNF network (see Figure 4.3 C and 4.4 B).

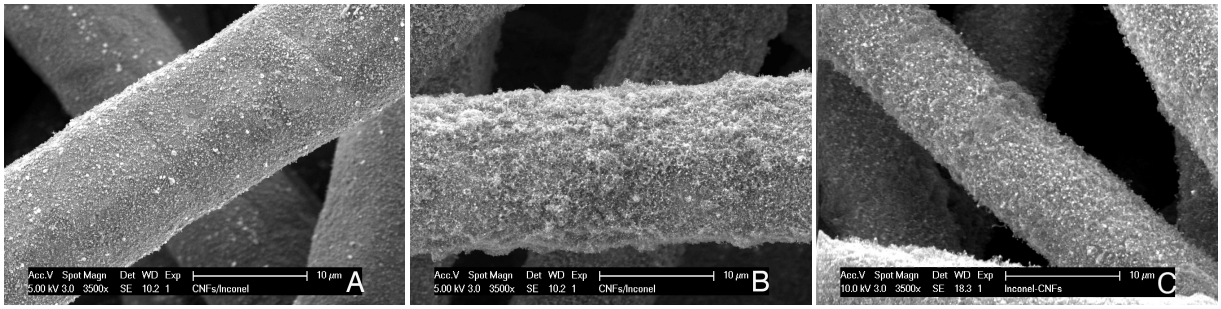

Figure 4.3: SEM micrographs (3500x) of CNF/SMF$_{Inconel}$ from ethane CVD at 923 K: A) after 5 min, B) after 10 min, C) after 60 min

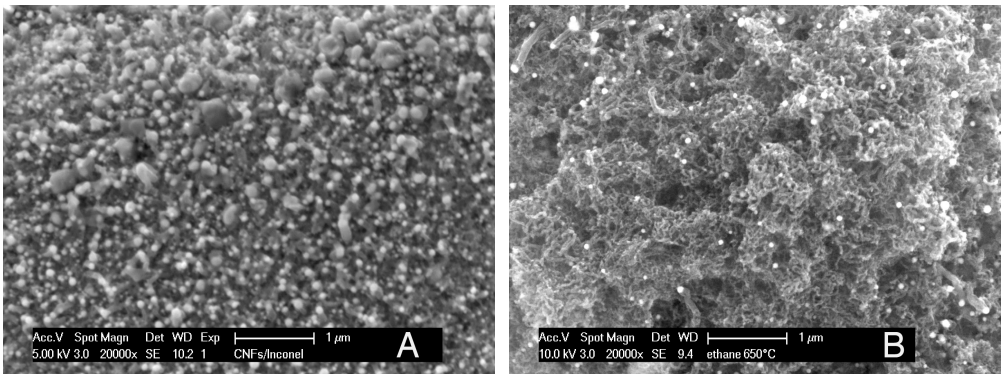

Figure 4.4: SEM micrographs (20000x) of CNF/SMF$_{Inconel}$ from ethane CVD at 923 K: A) after 5 min, B) after 60 min.

On the top of the CNF one can distinguish the metal particles from which the CNF originated, *in-situ* EDX analysis revealed that they are Ni-particles. Being encapsulated by several layers of graphitic carbon (see Figure 4.5), they are "inactive" for further adsorption of molecules when the composite material is employed as catalytic support. The TEM observation allowed to confirm that the structure of the CNF formed from SMF$_{Inconel}$ was platelet-like, as already observed by Tribolet *et al. [4]*.

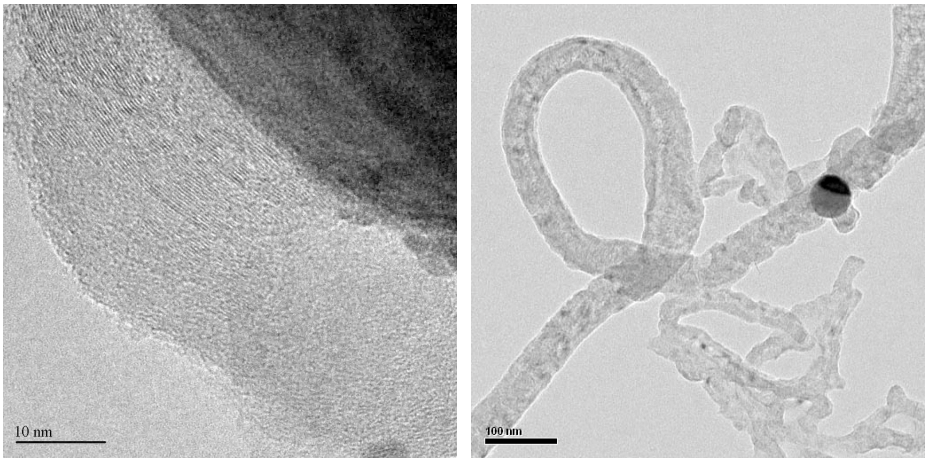

Figure 4.5: TEM micrograph (200000x and 50000x) of graphite layer on top of a metal particle and CNF detached from CNF/SMF$_{Inconel}$.

4.3.3 Cristallinity degree of CNF by TPO

The TPO technique, described in 3.4.4, allows one to assess the overall cristallinity of carbons and facilitates the distinction between structured and non-structured carbon. In the absence of metals, which may catalyze the oxidation, the onset for gasification of amorphous carbon to CO_2 occurs at 823 K, while the corresponding point for graphite is 1133 K [190, 191]. An increasing order in the carbon structure is accompanied by an elevation of the temperature at which gasification is induced. Nevertheless the presence of metals on the composite CNF/SMF$_{Inconel}$ can catalyze the oxidation and the onset temperature can shift at lower values. Higher cristallinity of CNF means less defects in the graphitic structure, which can be an advantage for supporting metal catalyst, due to the electronic interaction between metal particles and graphene layers.

The results of the TPO analysis are summarized in Figure 4.6. The experiments on CNF/SMF$_{Inconel}$ synthesized with ethylene at different temperatures showed that the maximum of the CO_2 peak was shifted toward higher values, compared to samples synthesized at the same temperatures but with ethane as precursor. When highly ordered carbon is required for supporting metal catalysts, ethylene is thus the best candidate for the synthesis of CNF/SMF$_{Inconel}$.

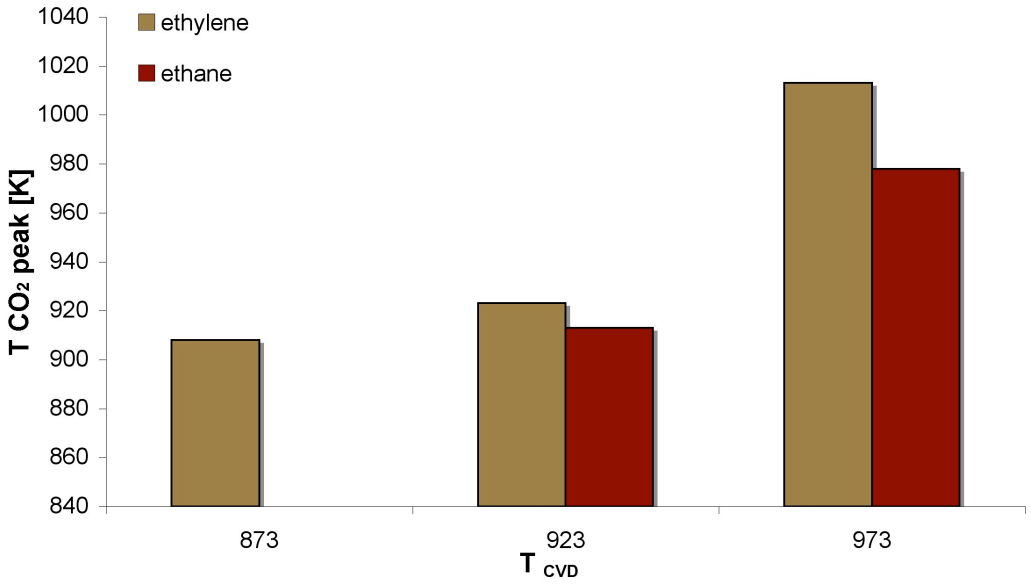

Figure 4.6: Temperature of the maximum CO_2 evolution during the TPO of CNF/SMF$_{Inconel}$ samples synthesized by ethane and ethylene CVD, respectively, at different synthesis temperatures.

In addition, increasing the synthesis temperature appeared to have enhanced the graphitic nature of the carbon deposited with both precursors, since the temperature of the maximum CO_2 evolution was higher. Hamwi *et al.* already observed an increasing order in carbon nanomaterials when graphitized at elevated temperatures: the treatment provoked significant structural changes and realized an improvement in order with the formation of rigid parallel layers [192].

4.3.4 BET Analysis

BET measurements, outlined in 3.4.1, were carried out on two samples of CNF/SMF$_{Inconel}$ synthesized from both C-precursors. The samples were synthesized at two different temperatures to take in account the higher reactivity of ethylene and to have similar morphology of CNF deposit for comparison. BET surface and pore volume should be attributed only to CNF, since the metallic surface of the filter is not porous and its SSA is not measurable (< 5 m^2/g). The results are presented in Table 4.2. Both isotherms obtained were characteristic of multilayer adsorption/desorption accompanied by capillary condensation in relatively large mesopores, causing a hysteresis loop [193] . The shape of the loops indicated a distribution of cylindrical pores.

Table 4.2: Characteristics of the CNF/SMF$_{Inconel}$ after 1 h synthesis.

C-source	$T_{synthesis}$ *[K]*	*C-Yield [wt.%]*	$SSA_{composite}$ *[m^2/g]*	SSA_{CNF} *[m^2/g]*	*Pore volume of CNF [ml/g]*
Ethane	923	3.5	15.2	434	0.41
Ethylene	873	7.3	37.6	516	0.24

The SSA of the CNF from ethane CVD was slightly lower than the value of 472 m^2/g reported by Tribolet [4, 15], most probably because the C-yield on the support was lower in the herein reported synthesis. SSA of the CNF from ethylene CVD was definitely higher, reaching the value of 516 m^2/g. Despite the higher amount of carbon deposited from ethylene, the accessibility of nitrogen to the inner part of CNF deposit was not compromised and the SSA increased with the increased production of CNF. The total pore volume decreased with the amount of CNF on the SMF$_{Inconel}$. The entanglement of CNF, which is the cause of mesoporosity, was higher for deposits from ethylene. Thus the resulting composite material was denser, but with higher SSA.

4.3.5 Pressure Drop in the Fixed-Bed Reactor

In 2.1.1 it has been mentioned the importance of minimizing the pressure drop through the catalytic bed in order to maintain the process energetically favorable. Thus, in order to successfully develop the CNF/SMF$_{Inconel}$ composite for catalytic applications, it is important to maintain the characteristic high porosity of SMF. The pressure drop of a gas flowing through the CNF/SMF$_{Inconel}$ has been measured as a function of the gas superficial velocity for CNF deposits from ethane and ethylene decomposition between 873 K and 920 K for 1 hour (see Fig. 4.7). The gas flow was varied and the pressure drop was measured by means of a U-tube containing water, which was connected to the tubular reactor charged with CNF/SMF$_{Inconel}$. Although the presence of a CNF layer on SMF did not change the behavior of the fluid through the filter, an increasing yield of CNF contributed to dramatically increase the pressure drop through the reactor. With a similar experiment conducted for CNF deposits from ethane CVD, a good compromise was found between permeability of the catalytic bed and pressure drop for a yield of CNF $\sim$ 6 wt.% [4, 84].

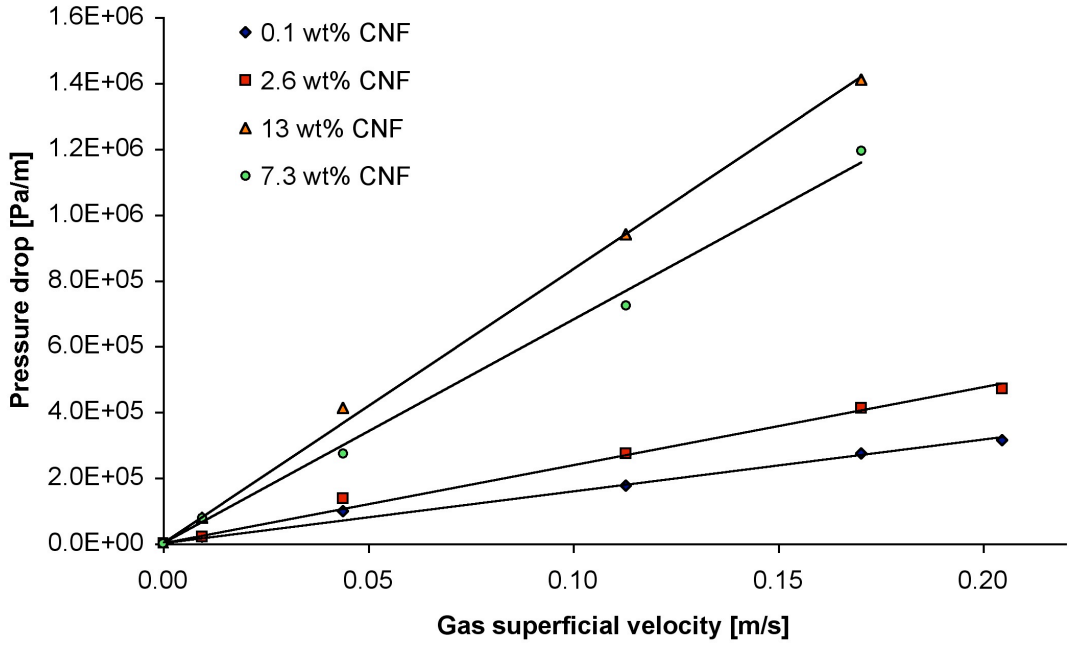

Figure 4.7: Pressure drop in the reactor as a function of the inlet gas flow rate.

When using ethane as carbon precursor, suitable CNF deposits can be synthesized at 923 K during 1 hour of CVD. On the other hand, when using ethylene as carbon precursor, the synthesis time or the temperature should be decreased, otherwise the permeability of the composite material can be compromised.

4.4 CNF/SMF$_{Inconel}$ Surface Functionalization

4.4.1 Oxidative Treatments

For some applications the use of CNF/SMF$_{Inconel}$ as catalyst support is conditioned by the modification of the CNF surface, as mentioned in 2.3.2. The use of oxidizing agents to introduce acidic surface oxides in graphite is well studied, concentrated nitric acid at its reflux temperature being the most common choice. Lakshminarayanan [194] carried out the oxidation of vapor grown nanofibers by nitric acid. Surface oxygen groups were reported to increase 3-fold within 10 min of oxidation with this procedure. More recently the oxidation of CNF by various oxidizing agents has been examined (oxidants used: 6 M HNO_3, $KMnO_4$, RuO_4, and a mixture of concentrated H_2SO_4/HNO_3) by Rasheed *et al.* [195] in order to correlate the oxidant strength to the defect sites, acidic sites, and yield of functional groups on the

surface of CNF. This kind of treatments are also used to purify CNF from their metal catalyst precursors. That is why they cannot be used for the composite CNF/SMF$_{Inconel}$, otherwise they would cause the dissolution of the macroscopic metallic structure of the material. For this purpose, milder oxidizing agents have been employed to functionalize CNF, such as H_2O_2 and its aqueous solutions [84].

In the herein reported study, CNF/SMF$_{Inconel}$ were treated with two oxidizing agents, which modified the surface of CNF without any influence on the metallic support (see 3.1.4):

- boiling 35% H_2O_2 solution for 4 hours.
- Plasma-generated O_3 from air for 30 min.

The type and the concentration of surface oxygen groups obtained by these two oxidative treatments were determined by TPD and XPS techniques.

4.4.2 Preliminary Characterization of the Surface by TPD

A preliminary characterization of the activated-CNF surface was conducted by TPD and interpreted based on the literature data available. This technique is easy and offers straightforward quantitative analysis of the desorbed species, in addition to being the most convenient way to study the thermal stability of surface oxides. Using this technique [95, 196–199] the following general trends were observed:

- CO_2 forms from carboxylic acids at lower temperatures, or from lactones at higher temperatures
- Carboxylic anhydrides form both CO and CO_2 peaks at the same time
- Phenols, ether, and carbonyls produce CO peaks

Figure 4.8 shows the TPD profiles obtained under flowing gas conditions, with the procedure outlined in 3.4.5. Both oxidation methods formed O-containing groups, which decomposed during TPD run giving CO and CO_2. The results obtained were dependent on the heating rate [90, 197], but the release of CO_2 at temperature < 650 K could be attributed to carboxylic groups [196, 200]. The CO_2 peaks at higher temperature are possibly related to acid derivatives like lactone and anhydride groups' decomposition. CO evolution is supposed to come from phenolic, carbonyl and quinone groups at temperature > 800 K [197, 201].

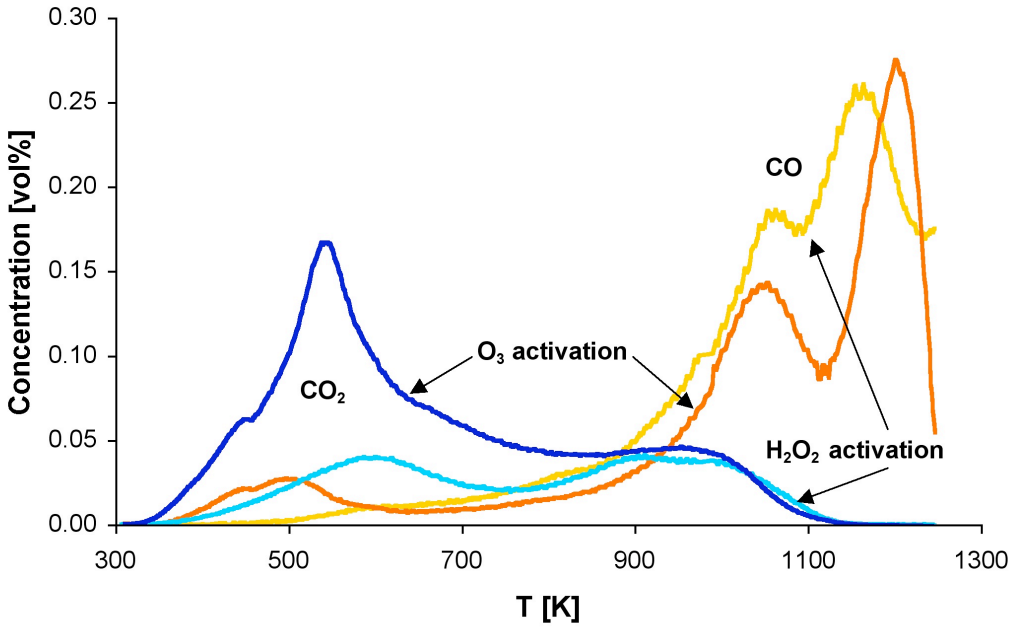

Figure 4.8: TPD profiles of CNF/SMF$_{Inconel}$ samples (0.2 g) activated with plasma-generated O_3 at room temperature for 30 min and with boiling 35% aqueous solution of H_2O_2 for 4 hours.

The total amount of functional groups was calculated by integration of the area under the TPD curves. It was found almost the same value for both activation treatments, but the O_3-based treatment gave higher yield of O-groups which leaded to CO_2 during the TPD < 700 K. It is therefore proved that this new treatment is suitable for the activation of CNF/SMF$_{Inconel}$ supports, supposedly leading to high yield of carboxylic groups.

The further characterization of the functional groups by coupled TPD and XPS analysis was carried-out, in order to have a clearer insight on the nature of the groups present on the CNF surface after the oxidative treatments. The experimental procedure and results are reported in the next section.

4.4.3 Step-wise TPD followed by XPS Analysis in Ultra High Vacuum (UHV) Chamber

4.4.3.1 Experimental

The samples were mounted on a sample holder made of sapphire (Figure 4.9). This material is a good choice for our experiments and for UHV systems in general because of its chemical inertness, mechanical stability, and unique thermal conductivity behaviour. It has a high thermal conductivity below room

temperature which helps in cooling the sample where needed. On the other hand at elevated temperatures it has a low thermal conductivity; this reduces the heat loss by conductance from the sample. Sapphire is an electrical insulator, too. This is essential in applying the used approach for temperature heating (by electron impact) and measurement (by k-type spot thermocouple welded on a Pt foil) and applying bias voltage in photoemission measurements.

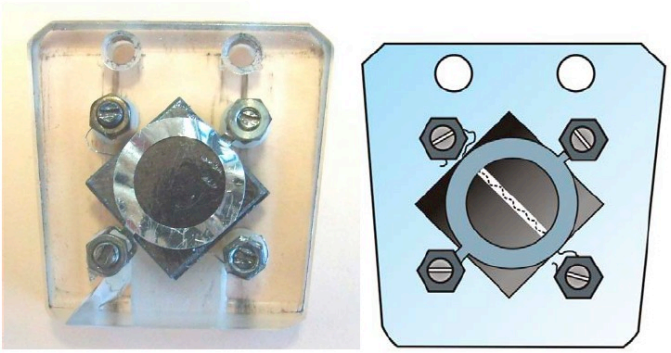

Figure 4.9: CNF/SMF$_{Inconel}$ sample mounted on the sapphire sample holder.

The rear face of the CNF/SMF$_{Inconel}$ sample was pressed on a Pt foil, which prevented the direct contact of the sample with the electron beam and protected the filament from the desorbing gases of the sample. In the UHV chamber (3×10^{-10} mbar), the sample was heated up to 1373 K using electron bombardment by a filament which was placed just behind the sample. The contact between the sample and the Pt mask was not optimized, so the heating was not perfectly homogeneous, generating temperature gradients on the sample. The observation of inhomogeneous glowing of the samples at measured T > 1043 let suppose that part of the sample reached higher temperatures than the measured ones. Because of the presence and release of oxygen on the sample (from the metal oxides of SMF), at such high temperatures part of the carbon burned-off on the rear face of the sample, as seen in Figure 4.10. Results at T > 890 K were discarded because of the burning-off of CNF on the samples. The metal oxides on the surface were likely reduced by carbon, consequently evolving CO.

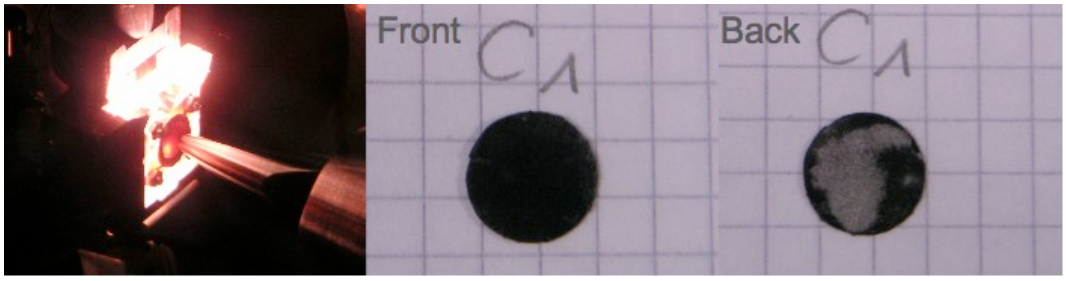

Figure 4.10: CNF/SMF$_{Inconel}$-C1 sample in the UHV chamber heated at 1043 K and after the experiment (front and back face).

The UHV chamber was equipped with a differentially pumped OMS-200 quadrupole mass spectrometer (MS, Pfeiffer Vacuum), in order to monitor CO and CO_2 desorbed. Temperature programmed analysis were performed by placing the sample at $\sim$ 1 mm from the aperture of the differentially pumped MS, which was shielded against desorption from the sample.

After each heating step, XPS measurements were carried out at room temperature. During the TPD, a temperature distribution was generated on the sample surface and the MS-measured gas most likely desorbed from a different area than the one analyzed by XPS. As a consequence, quantitative correlations between TPD and XPS results were not precise. The XP spectra were recorded at room temperature, using a non-monochromatized Mg Kα radiation (1253.6 eV) for excitation and a hemispherical sector analyzer (Phoibos, SPECS). The X-ray anode was kept at voltage of 10 kV during the analysis. An overview spectra (0-1000 eV) and both narrow regions of C1s (270-330eV) and O1s (520-540 eV) with longer scanning time were recordered. The deconvolution of the main O1s peak was performed by means of CasaXPS software. After subtraction of a Shirley background, the peaks were fitted using a nonlinear, least squares routine with mixed Gaussian-Lorentz functions. Each peak should correspond to a different surface functionality. The deconvolution of the main peak of the C1s region is generally more difficult to carry out, because the relative contribution of the peaks from oxygenated groups compared to graphitized carbon is too small to be isolated from the spectra itself. Instead, the C1s difference spectra between untreated and activated samples were calculated by direct subtraction.

Table 4.3: Samples of activated CNF/SMF$_{Inconel}$ analyzed through the study reported in the herein Section.

Sample ID	Oxidant	Analysis
A1	-	XPS
C1	H_2O_2	TPD
C2	H_2O_2	XPS-TPD
C3	H_2O_2	TPD
D1	O_3	TPD
D3	O_3	TPD
D4	O_3	XPS-TPD
SMF$_{Inconel}$	-	TPD

Table 1 summarizes the characteristics of the samples of activated CNF/SMF$_{Inconel}$ analyzed. Firstly, surveys of TPD at the heating rate of 13 K/min from samples C1, C3 and D1, D3 were carried out to estimate at which temperatures CO and CO_2 evolved. After getting the whole MS-spectra from room temperature till 1200 K, the heating step were chosen. Secondly, step-wise TPD with subsequent XPS measurements were performed on two samples (C2 and D4). Blank TPD and XPS measurements were performed on CNF/SMF$_{Inconel}$ without oxygen-functionalities (A1).

4.4.3.2 TPD results

From a qualitatively point of view, the comparison of the TPD profiles of CO_2 in the UHV chamber and under flowing He (see 4.4.2) confirmed that the heating of the samples under UHV conditions was not uniform, as shown in Figure 4.11. Indeed the onset temperature for the different peaks is the same, but the peak areas are much broader in the first case, proving that on the sample a temperature gradient was generated and the measured temperature did not correspond to the actual temperature at which the gas desorbed.

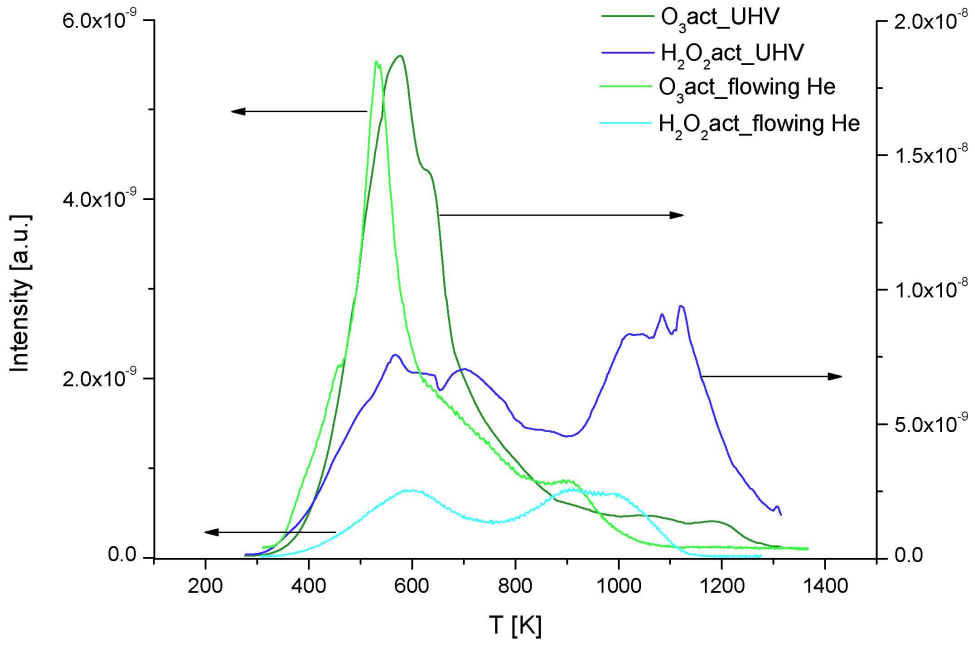

Figure 4.11: Comparison of CO_2 spectra from TPD in UHV chamber or under flowing He. Samples activated with plasma-generated O_3 at room temperature for 30 min and with boiling 35% aqueous solution of H_2O_2 for 4 hours.

The results of the desorption experiments on sample C1 and D3 are presented in Figure 4.12, showing the profiles of CO and CO_2 evolving while the samples were heated. The most remarkable difference between the two samples was related to the CO_2 desorption: from sample D3 the gas evolved mainly in the lower temperature range (< 800 K), with a maximum at about 600 K, while a broader but less intense CO_2 evolution from sample C3 was observed at low temperature, as well as at higher temperature until 1000 K. In the literature, the evolution of CO_2 at low temperature is usually assigned to the carboxylic functional group, while at temperatures higher than 700 K the CO_2 evolution is attributed to the decomposition of anhydride and lactone groups; CO formation is usually assigned to the decomposition of phenols, ethers and carbonyl/quinones at high temperatures > 800 K (for reference see 4.4.2). Nevertheless the interpretation of TPD profiles in the literature is ambiguous. In the herein reported experiment, a small fraction of CO evolved also at lower temperature from sample D4 concomitant to the CO_2 desorption. At temperature higher than 890 K, the CO formation increased so steeply that it was difficult to distinguish the contribution coming from either the decomposition of functional groups on the CNF surface, or the "burning-off" of the CNF themselves.

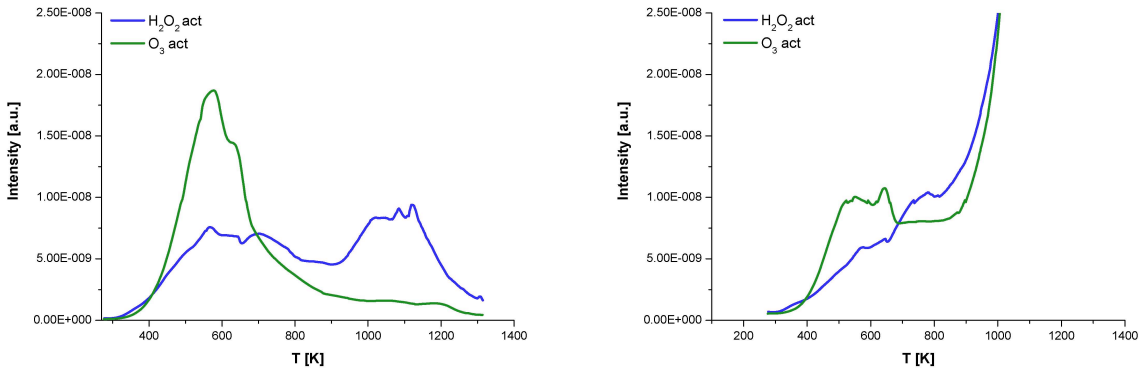

(a) Evolution of CO_2

(b) Evolution of CO

Figure 4.12: TPD spectra of samples D3 and C1, in UHV chamber.

From the analysis of the TPD profiles shown in Figure 4.12, the heating steps were chosen in order to analyze the surface composition corresponding to the maxima and shoulders in the TPD spectra. The results of step-wise heating of samples C2 and D4 are presented in Figure 4.13, they show a good agreement with the complete TPD spectra in Figure 4.12.

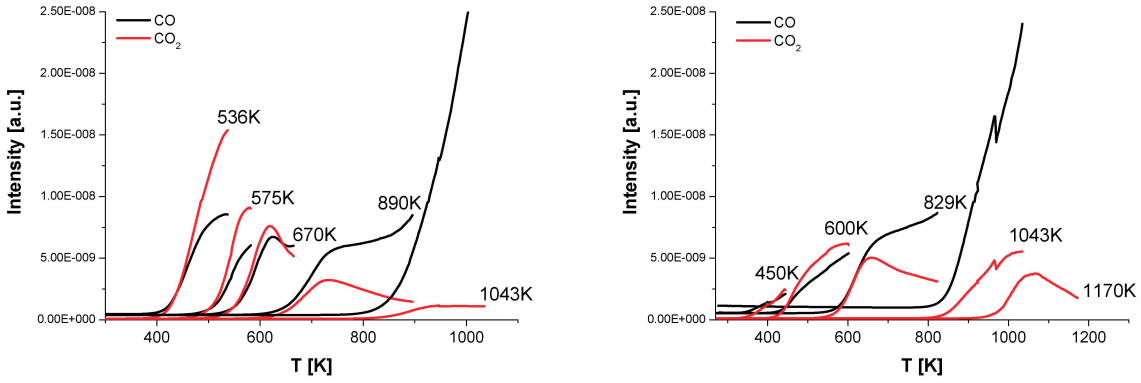

(a) O_3 activated

(b) H_2O_2 activated

Figure 4.13: Step-wise TPD spectra of CO (black line) and CO_2 (red line) evolution from samples D4 (a) and C2 (b).

The quantification by integration of the TPD signal was carried out and compared with the XPS O1s intensities: the correlation found was quite good, taking in account the temperature gradients through the sample and its heterogeneous surface.

4.4.3.3 XPS results

Overview spectra in the range of 0-1000 eV were recorded in order to identify the surface elements present on the samples. The major constituents identified were carbon and oxygen for the samples of C and D series. No oxygen peak was observed in the spectra of the sample A1, showing that the surface oxygen content of untreated CNF/SMF$_{Inconel}$ is negligible.

Figure 4.14 presents the superposition of the XP spectra in the C1s region for samples A1, C2 and D4, before any heating and the difference spectra between raw and oxidized samples. The observation of the changes in the C1s spectra allowed to elucidate the degree of oxidation of the surface, indeed the oxidizing process could be related to the presence of defective sites in the graphene layers, thus to a lower degree of graphitization [87, 88].

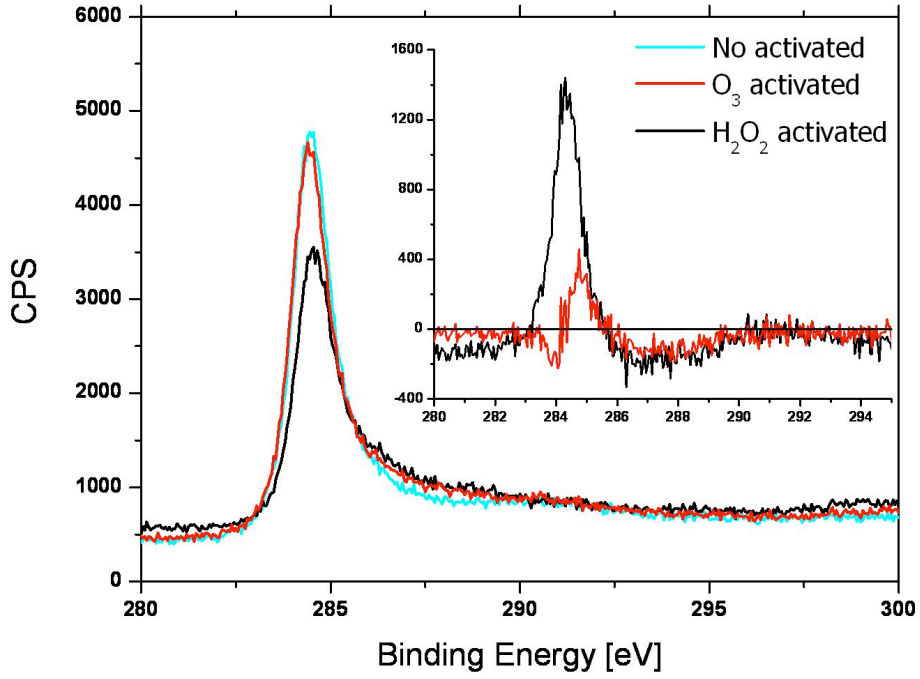

Figure 4.14: C1s spectra of samples A1, C2 and D4 before heating in the UHV chamber, with inset of the difference spectra between untreated and oxidized samples

The intensity of the peak associated to graphitic carbon (284.5 eV) decreased passing from the untreated carbon to the activated ones, showing the modification of the surface. The contribution of oxidized

carbon could be better observed on the difference spectra at higher binding energy (286-289 eV), where deconvoluted peaks are generally assigned to carbon functionalities [201–203]. On the difference spectra of sample D4 another contribution could be observed at ∼283.9 eV and identified with Ni_3C [204], which is the active phase for the formation of CNF on SMF$_{Inconel}$ (see 2.2.4).

In the O1s spectra, although the shifts associated to the different functionalities are generally very small, it is somehow easier to reveal the overlapping features corresponding to the functional groups because the relative contributions of each peak to the spectra are in the same order of magnitude i.e. no difference spectra are necessary as for the analysis of the C1s range. The fittings of O1s spectra of samples C2 and D4, before heating, are shown in Figure 4.15.

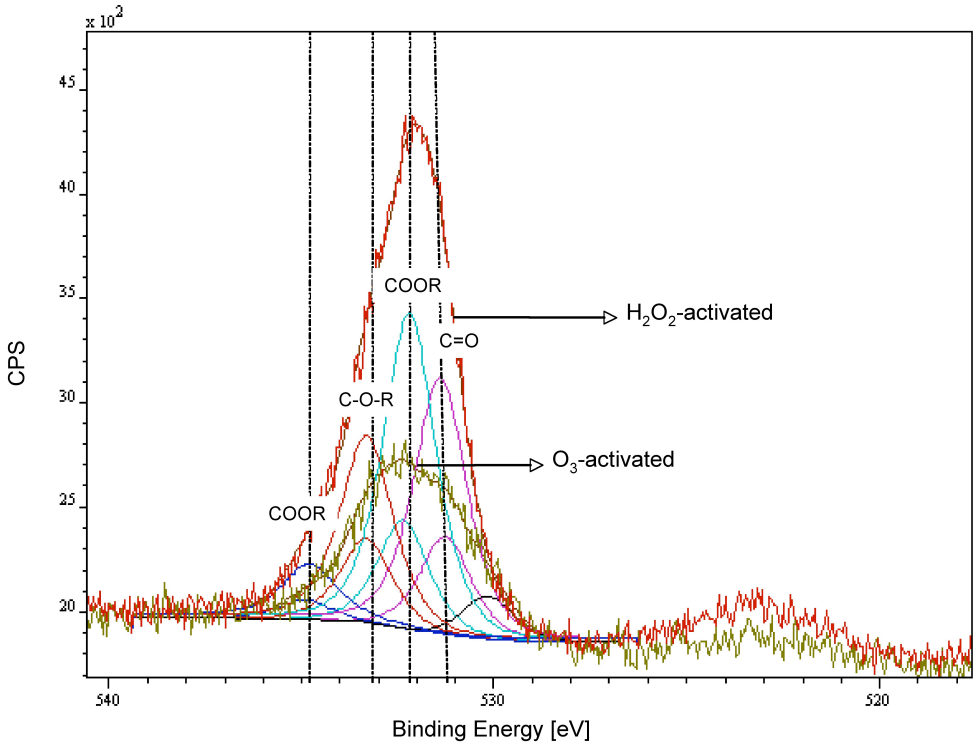

Figure 4.15: Superposition of O1s spectra of samples differently activated before heating in the UHV chamber, fitted with the software CasaXPS.

A set of at least four peaks were observed for both samples (**A** at 531.2 eV, **B** at 532.2 eV, **C** at 533.3 eV, **D** at 534.8 eV), while for D4 an additional peak at lower binding energy (530.3 eV) resulted from the fitting. The data reported in literature assign peak **A** to carbonyl groups, peak **B** to carbonyl oxygen atoms in esters and anhydrides or to oxygen atoms in phenol or ethers, peak **C** to ether oxygen atoms in

esters or anhydrides, and peak **D** to carboxylic groups [201,203]. The peak at BE 530.3 eV of sample D4 was supposedly assigned to oxygen atoms bonded to the metal present on the sample, which should be insensitive to the heating treatment. The oxygen/carbon atomic ratios calculated from the C1s difference spectra were always in the range of 0.5-1.5. The wide error bar of the difference spectra did not allowed any further quantification.

4.4.3.4 Effect of step-wise heating on XPS results

Following the heat treatment, the surface of CNF lost part of the functional groups created by the oxidative treatments. The interpretation of the results of the TPD experiments did not allow univocally identifying the nature of oxygenated groups on the CNF surface, based on their thermal stability. So, following the step-wise heating, XPS analysis of the surface were carried out.

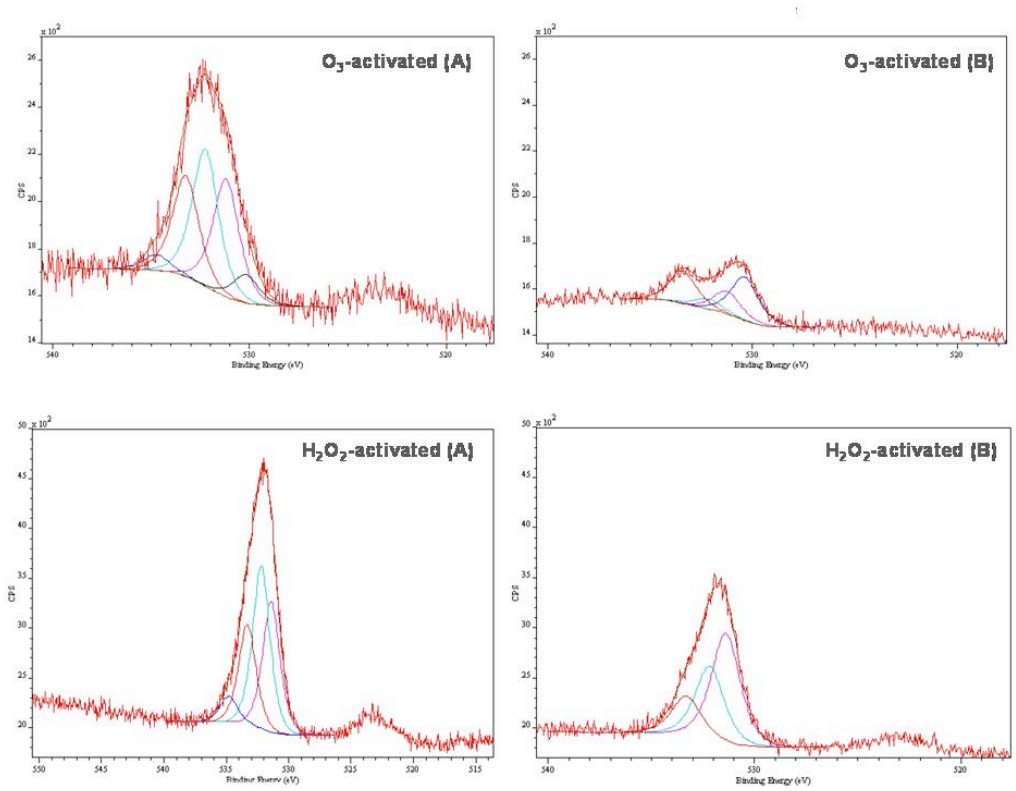

Figure 4.16: O1s spectra of samples D4 and C2, (A) before heating and (B) after step-wise heating till 1043 K in the UHV chamber.

Subsequently, the relative change in the deconvoluted O1s spectra were calculated, in order to qualitatively link the CO and CO_2 desorption to the relative decrease in intensity of the peaks in the O1s region. Figure 4.16 shows an example of deconvoluted O1s spectra, before and after step-wise heating. The intensity of all peaks decreased, as expected, except for the peak at BE 530.3 eV (sample D4). This feature is therefore confirmed to be insensitive to the thermal treatment. As already visible on Figure 4.16, the two samples showed different decrease in intensity of the deconvoluted O1s spectra. So, the variation of the fitted peak areas for both samples was reported as function of the step-wise heating in Figure 4.17. At temperatures lower than 700 K the evolution of CO_2 and CO during the TPD of sample D4 could be related to the loss of groups giving peaks **A** and **B** in the O1s spectra. The decrease in intensity of the peaks **A** and **B** was much steeper at lower temperatures for sample D4 than for sample C2, explaining why at lower temperature the gas desorption from sample C2 is less pronounced (see Figure 4.13). At higher temperatures, the intensity of peak **C** decreased fast for both samples, but the intensity of peak **B** decreased faster for sample C2 than for sample D4. It could therefore be supposed that the groups corresponding to peak **B** decomposed mainly giving CO_2 both at low and high temperatures.

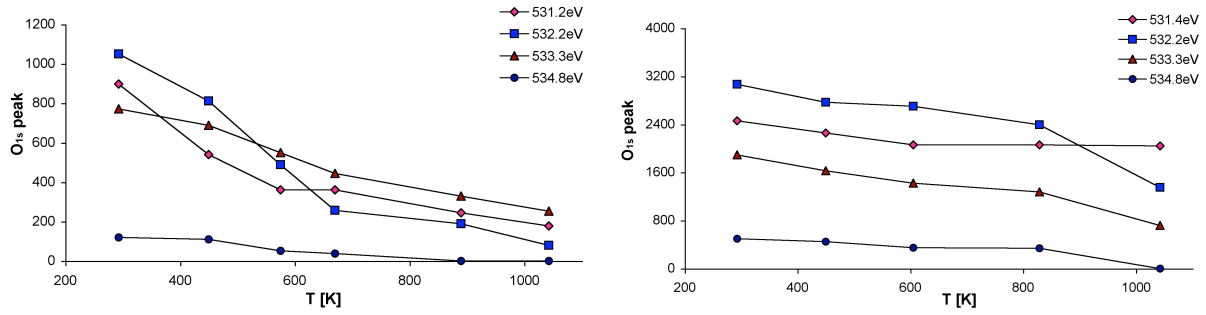

(a) O_3 activated

(b) H_2O_2 activated

Figure 4.17: Variation of the area of XPS fitted peaks from O1s spectra of samples D4 and C2, after step-wise heating in the UHV chamber.

From this analysis peak **B** could be supposedly related to carbonyl oxygen atoms in anhydrides, lactones, and carboxylic acid, which decomposed over all the range of temperature to CO_2 and partly to CO. The distinction among the three different functionalities form the XPS results was not straightforward. Nevertheless, following this hypothesis, sample D4 contained a higher relative percentage of carboxylic groups which decomposed at lower temperatures, compared to sample C2. The results obtained by the interpretation of the TPD experiments were thus confirmed.

4.5 Conclusions

CNF/SMF$_{Inconel}$ structured supports prepared from the CVD of ethane or ethylene were compared in terms of CNF-yield, cristallinity degree of CNF, SSA, and pressure drop in a fixed bed reactor. Due to its higher reactivity, ethylene CVD yielded a higher quantity of CNF and a wider SSA than ethane, at the same reaction conditions. Thus, in order to obtain a suitable support for catalytic applications, employing ethylene as carbon precursor allowed to decrease the temperature of the synthesis, which was favorable from an energetic point of view. Furthermore, the CNF formed from the ethylene decomposition showed a higher degree of cristallinity, which, when applied as noble metal supports, could provide a better electronic interaction (π-interaction) between the carbon nanostructured surface and the supported metal species. Despite the favorable properties of the material prepared by ethylene CVD, it has been decided to use ethane as carbon precursor for the further applications because for CNF loadings higher than 6 wt.% the pressure drop caused by the material in the reactor was too high and the permeability of the support was compromised. The characterization of the CNF/SMF$_{Inconel}$, synthesized at different reaction time, allowed us to confirm the mechanism of growth octopus-like, which involves the fragmentation of the metal catalyst into sub-particles during the growth of CNF on the SMF.

The activation of CNF surface was carried out with two different oxidizing methods: H_2O_2-based and O_3-based. Both were found suitable to activate the material, but from the characterization of the surface functionalities by TPD it was found that the O_3 -activation provided a higher yield in carboxylic acidic groups. The combined application in a UHV chamber of step-wise TPD followed by XPS analysis was found a highly useful, but not definitive method to identify O-containing functional groups on the surface. It provided further evidence for the higher amount of carboxylic groups on the surface activated with O_3, which start to decompose to CO_2 around 450 K. This feature is important, because the acidity of the support can modify the catalytic properties of the active phase deposited, so at high reaction temperature the catalyst can behave differently because of the decomposition of carboxylic groups and consequently the diminished acidity of the support. Thus, the influence of the acidity of the CNF/SMF$_{Inconel}$ on the catalytic properties of supported Pd nanoparticles for the acetylene hydrogenation is reported in Chapter 6.

Chapter 5

Structured Fibrous Supports for SILP Catalysis used in Continuous Gas-Phase Hydrogenation

5.1 Introduction

Supported ionic liquid phase (SILP) has attracted increasing attention in the chemical reaction engineering field, especially for applications in continuous-flow reactors [124, 125, 130, 205]. The SILP concept has been illustrated in 2.4.3, the main advantage consists in the reduced amount of IL needed to dissolve the catalytic active phase and its multiple reuses, being economically and environmentally beneficial. The feasibility of the SILP catalysis has been demonstrated by several authors on granulated silica randomly packed [205, 206] in fixed-bed reactors [133, 138, 139], in which the catalyst is stationary and the reactants pass over it. Moreover, most of the reactions tested were in liquid/solid-phase with only few reported in gas-phase [133, 138]. Coupling the SILP concept with catalytic beds with a regular (structured) catalyst arrangement present multiple advantages. Structured supports usually show low pressure drop during the fluid passage through the reactor and an even flow distribution, resulting in a narrow residence time distribution (RDT). This property is very important for complex reactions with an intermediate as target product. High selectivity can be achieved, leading to the process intensification and favorable environmental impact. In this Chapter it is reported how the SMF-based materials have been applied as structured support for the IL phase containing a homogeneous catalyst. The feasibility of the structured-SILP catalysis for gas-phase reactions was tested in the hydrogenation of 1,3-cyclohexadiene

to cyclohexene. This reaction is selectively catalyzed by rhodium based complexes [207] and is a valid model of hydrogenation of a diene to form a monoene, especially because in some IL the monoene is less soluble than the diene so the selectivity of the catalytic system should be improved [208]. Different IL were tested for the reaction in analysis. Furthermore the influence of the support nature and morphology was investigated in order to find the most active and selective catalytic system. Finally the ^{1}H NMR and ^{1}H[^{31}P] NMR spectroscopy was used to provide insight into the nature of the active catalytic species.

5.2 Preparation and Characterization of the SSILP (Structured SILP) Catalyst

The SMF plates consist of uniform metallic filaments sintered into a homogeneous 3-dimensional structure, with porosity up to 80-90% which provides high permeability (see 3.1.1). The fibrous matrix exhibits high mechanical strength combined with chemical and thermal stability. It also acts as a static micromixer to prevent gas channeling within the catalytic bed. Due to the small fiber diameter ($\sim 2 - 20\mu m$), SMF filters are suitable supports for micrometer-thickness films of a catalytically active phase [14]. This catalyst design decreases internal diffusion limitations, reducing the amount of catalyst required. The high thermal conductivity of the SMF provides a radial heat transfer twice that of randomly packed catalytic beds [209], leading to nearly isothermal conditions during isotherm reaction operations.

Figure 5.1 shows a schematic representation of the structured SMF support in application to IL phase catalysis during gas-phase hydrogenation. The SMF filter can be used as it is, or its surface can be modified to improve the homogeneous spreading of IL.

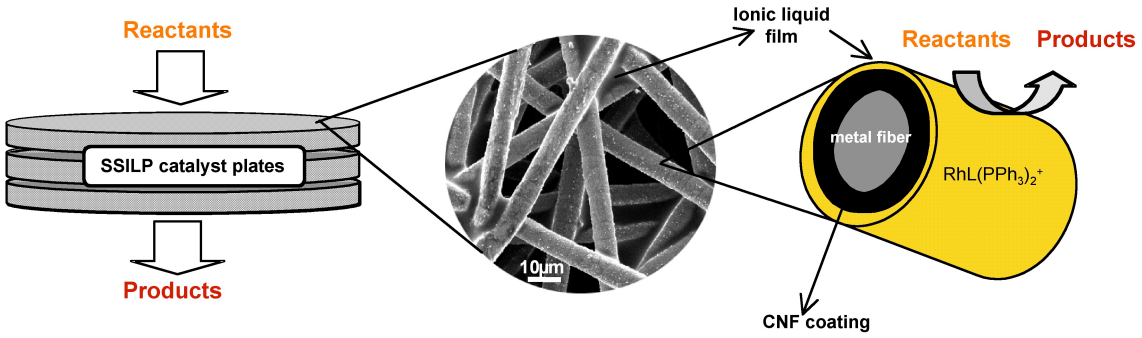

Figure 5.1: Schematic representation of structured SMF support applied for IL-phase catalysis during gas-phase hydrogenation in fixed-bed reactor.

During the study reported in this Chapter, different modified SMF were used as IL phase supports. The deposition of IL phase is described in detail in 3.2. The surface morphology of the supports were characterized by SEM. The images at different magnifications are shown in Figure 5.2 and Figure 5.3. As seen, the SMF$_{Inconel}$ filter consists of uniform metal fibers of $8\mu m$ in diameter, whereas the SMF$_{Fecralloy}$ has fibers up to $\sim 20\mu m$ in diameter. Some grain boundaries can be seen on the metal surface, indicating the formation of metal oxides after SMF oxidation. The Fecralloy fibers were rougher because of the formation of an $\alpha - Al_2O_3$ layer on the surface during the high-temperature treatment; aluminum diffused from the bulk toward the surface where it is oxidized, generating an oxide film [182]. The SMF filters presented an open macrostructure with high porosity after the coating of their surface by CNF or zeolites. As seen in Figures 5.2 (B) and (D), and 5.3 (B) and (D), the liquid phase completely covered the metal fibers. However, the homogeneity of the coverage strongly depends on the fiber surface morphology. On relatively smooth Inconel fibers an excess of IL tended to form meniscuses at fibers crossing points, whereas the mesoporous layer of CNF on the metal surface allowed an easy spreading, leading to uniform IL layers. The same phenomenon was found when observing at SEM the SMF$_{Fecralloy}$ and ZSM-5/SMF$_{Fecralloy}$. Zeolites on the metal fibers form a network in which IL could be easily deposited, resulting in an uniform film.

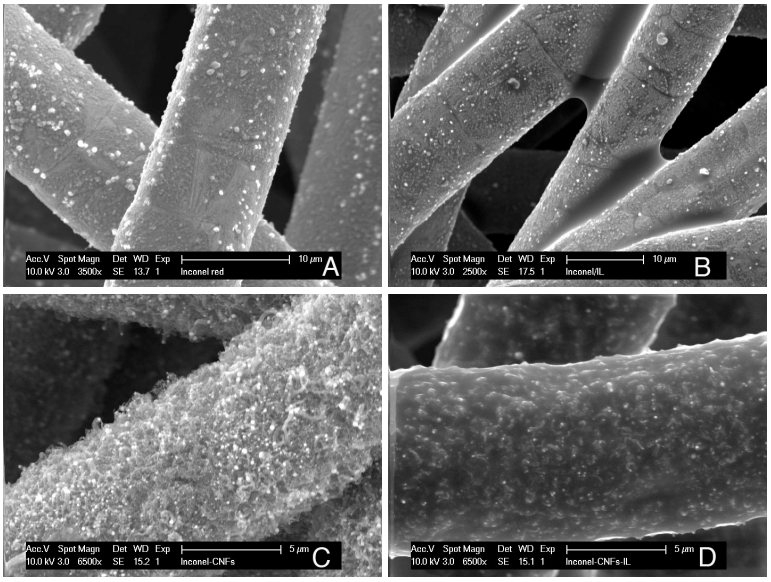

Figure 5.2: SEM images of SMF$_{Inconel}$: (A) SMF oxidized, (B) IL/SMF, (C) CNF/SMF, (D) IL/CNF/SMF$_{Inconel}$.

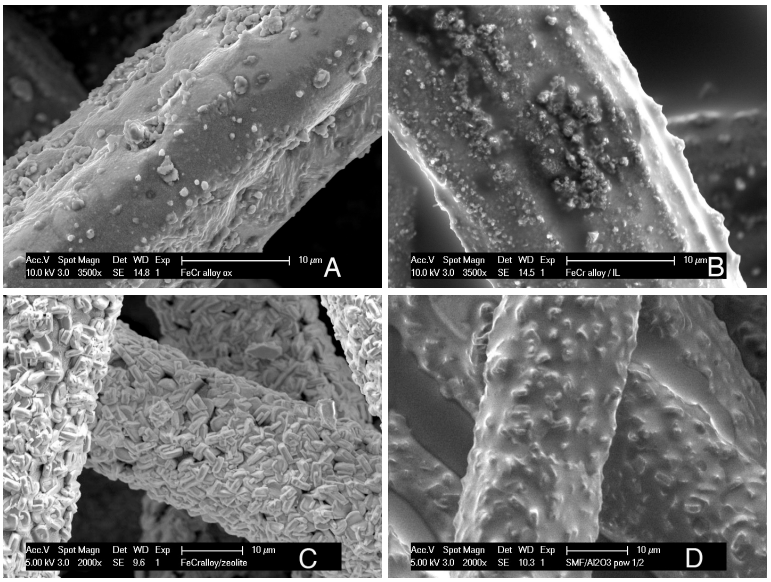

Figure 5.3: SEM images of SMF$_{Fecralloy}$: (A) SMF oxidized, (B) IL/SMF, (C) ZSM-5/SMF, (D) IL/ZSM-5/SMF.

In order to demonstrate that $\sim$10% of IL supported on SMF does not affect the gas permeability compared with the support itself, the pressure drop in the reactor was measured at different velocities of flowing Ar. The results are presented in Figure 5.4. The pressure drop slightly increased when the reactor was charged with SMF filters as catalytic bed, but it remained almost the same after the IL deposition.

Thus, the presence of the IL phase on the supports did not change the permeability of the catalytic bed. From an energetic point of view, this results prove that SILP catalysts employing SMF as supports are superior to the conventional granulated packed bed.

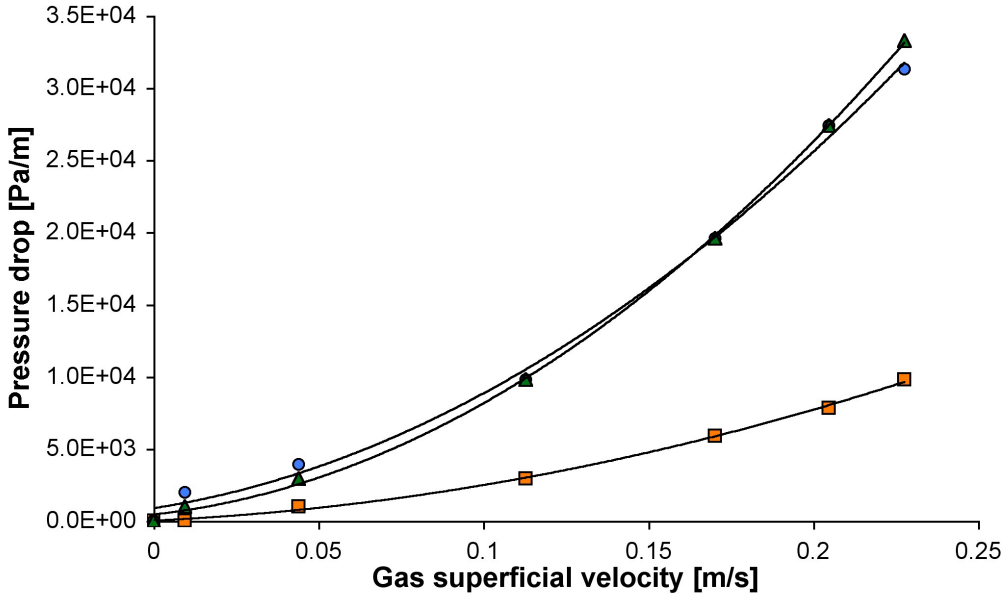

Figure 5.4: Pressure drop as a function of the inlet gas flow rate: (□) empty reactor, (△)SMF$_{Inconel}$, (○) IL/SMF$_{Inconel}$.

5.3 Catalytic Performance towards the Hydrogenation of 1,3 Cyclohexadiene

5.3.1 Test Reaction: Selective Hydrogenation of 1,3 Cyclohexadiene

Hydrogenation processes are an important class of reactions which can benefit from the optimization of homogeneous catalytic systems, especially in the fine chemical manufacturing. Following this trend our scope aimed on proving the feasibility of the concept of structured-SILP (SSILP) for industrial meaningful hydrogenations.

The selective hydrogenation of 1,3 cyclohexadiene to cyclohexene, outlined in Figure 5.5, was carried out in gas-phase at 333 K and ambient pressure as described in 3.2.

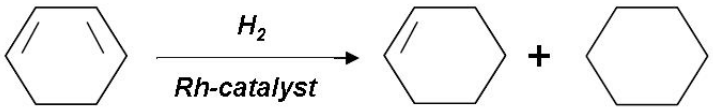

Figure 5.5: Hydrogenation of 1,3-cyclohexadiene to cyclohexene catalyzed by Rh complexes.

It is a classical test reaction of selective hydrogenation of a conjugated diene to form a monoene. For our scope, it is all the more interesting since diolefins are more soluble in IL than the corresponding monoalkene. The characteristics of this hydrogenation are essentially the same as those of 1,3-butadienes. Since IL are known to dissolve charged species, the hydrogenation of 1,3 cyclohexadiene can be performed using the homogeneous Osborn complex, [Rh(nbd)(PPh_3)$_2$][X], as cationic catalyst precursor [210]. Other Rh based complex, such as [Rh(COD)L_n]$^+$ and [Rh(TFB)L_n]$^+$, yield the same catalytic active species for the hydrogenation, but the rate of reduction of the diene is some 10^2 faster with [Rh(nbd)(PPh_3)$_2$]$^+$ than with [Rh(COD)(PPh_3)$_2$]$^+$ [211]. The same catalytic system was investigated by Chauvin *et al.* in unsupported IL [212, 213] and by Mehnert *et al.* both in SILP on silica and in unsupported biphasic system [130]. The superior catalytic performance in IL, compared to that observed in organic solvent, was proved. Furthermore the SILP system showed enhanced activity compared to the unsupported one.

5.3.2 TOF and Selectivity

The optimized SSILP catalyst showed suitable activity during continuous operation along with high selectivity to cyclohexene (> 96%). High selectivity was previously reported by Chauvin *et al*. [213] in the unsupported catalytic system: the diene is more soluble in IL than the monoene, this allows cyclohexene to escape from the IL phase before being hydrogenated. The consecutive overhydrogenation to cyclohexane is disfavored and the selectivity is potentially improved. As seen in Figure 5.6, the SSILP catalyst attained a quasi-steady state after 2 hours on stream, the corresponding values of the specific reaction rate (at diene conversion of $\sim$20-30% and calculated according to 5.1) could be used to compare the efficiencies of different catalytic systems. When the kinetics of the reaction was not influenced by the mass transport, the specific reaction rate was considered the catalyst turnover frequency (TOF). Nevertheless a slow deactivation after 3 hours on stream was observed.

$$R = \frac{F_{C_6H_8} \cdot X_{C_6H_8}}{n_{Rh}} \tag{5.1}$$

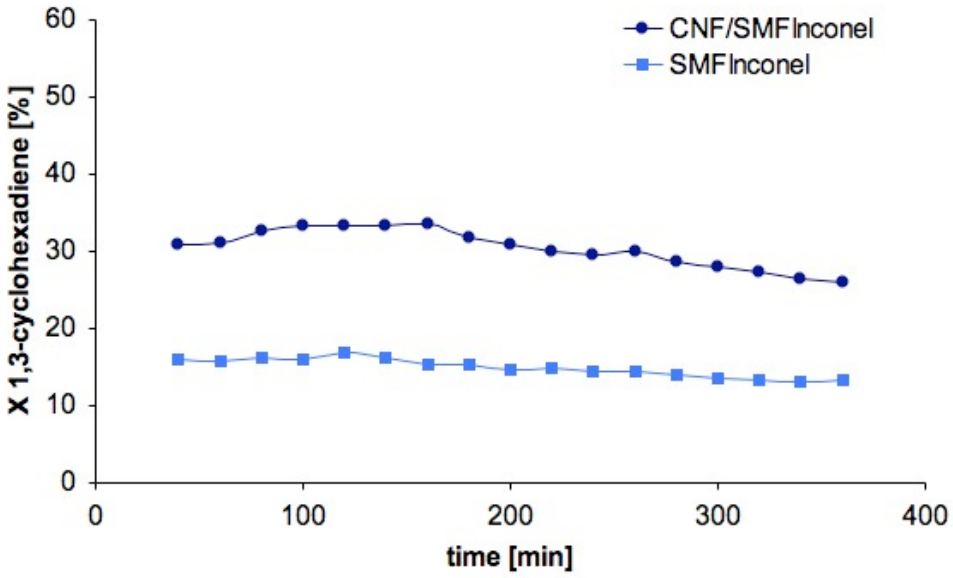

Figure 5.6: Evolution of the conversion versus the time on-stream of the catalysts $[Rh(nbd)Cl]_2$ + PPh_3/[bmim][BF_4]/HBF_4 (Rh 0.06 wt.%, HBF_4/[bmim][BF_4] ratio 0.5) supported on CNF/$SMF_{Inconel}$ and on $SMF_{Inconel}$. Selectivity to cyclohexene is for both catalysts > 96%.

Table 5.1 presents the values for catalyst activity and selectivity with varying parameters: SMF and IL used, acid/IL molar ratio, PPh_3/Rh molar ratio, and Rh loading (wt. %). [bmim][PF_6] and [bmim][BF_4] were chosen because they are hydrophobic and hydrophilic, respectively, and they are easy to handle. Nevertheless, the morphology of the SSILP catalysts did not change and the spreading of IL on the supports was similar for the two system tested.

Table 5.1: $[Rh(nbd)(PPh_3)_2]^+$-based SSILP catalysts for 1,3-cyclohexadiene hydrogenation, Rh loading 0.06 wt.%. (*) $[bmimSO_3H][CF_3SO_3]$

Entry	*Support (SMF)*	*[bmim][X]*	*IL (wt.%)*	*Acid/IL ratio*	*PPh_3/Rh ratio*	*R (h^{-1})*	*S (%)*
1	Inconel	PF_6	10	-	8	<1	-
2	Inconel	PF_6	10	0.3 (H_3PO_4)	8	20	93
3	Inconel	PF_6	11	0.5 (H_3PO_4)	8	85	>96
4	Inconel	PF_6	11	1.0 (H_3PO_4)	8	35	96
5	2%CNF/Inc	PF_6	11	0.5 (H_3PO_4)	8	140	>96
6	Inconel	BF_4	11	0.5 (HBF_4)	2	75	70
7	Inconel	BF_4	11	0.5 (HBF_4)	4	115	78
8	Inconel	BF_4	11	0.5 (HBF_4)	6	150	90
9	Inconel	BF_4	11	0.5 (HBF_4)	8	130	96
10	2%CNF/Inc	BF_4	12	0.5 (HBF_4)	8	285	>96
11	Fecralloy	PF_6	8	0.5 (H_3PO_4)	8	55	95
12	6%ZSM-5/Fecr	PF_6	7	0.5 (H_3PO_4)	8	115	95
13	Inconel	sulfonic IL*	10	-	8	60	>96

All of the Rh-based SSILP catalysts were found to be active for the gas-phase hydrogenation only in presence of acidic species. When an acid was added to the solution used to impregnate the supports, the resulted catalyst was able to reach the specific reaction rate of 140 h^{-1} (entry 5) for $[bmim][PF_6]/H_3PO_4$. When $[bmim][BF_4]/HBF_4$ was used, the observed reaction rate increased up to 285 h^{-1} (entry 10). On changing the molar ratio of acid /IL for $[bmim][PF_6]/H_3PO_4$ (entries 1, 2, 3, and 4), an optimal ratio of 0.5 was found (see 5.3.4). The same ratio was then used for the $[bmim][BF_4]/HBF_4$ catalytic system; the activity was higher for $[bmim][BF_4]/HBF_4$ than for $[bmim][PF_6]/H_3PO_4$ (entries 4, 9 and 5, 10).

5.3.3 Influence of the Support and Mass Transfer Limitations

The results presented in table 5.1 shows that the support used affected the catalyst activity. The reason could be linked to the chemical nature and/or the morphology of the support. The latter parameter is known to control the wetting properties of IL, influencing the thickness of the catalytic-phase film. Thin

film spread over high-SSA supports should preclude diffusion limitations, increasing the overall reaction rate.

To verify whether the reaction kinetics are influenced by diffusion, several catalysts with different IL phase loadings (2-12 wt. %) and the same Rh loading in IL (0.9 wt.%) were synthesized. The results, presented in Figure 5.7, show that the activity of the catalysts supported on CNF/SMF$_{Inconel}$ was directly proportional to the catalyst loading up to 12 wt.%. This indicated that the reaction is not affected by gas diffusion in the IL film. However, the catalysts supported on SMF$_{Inconel}$ showed the influence of diffusion for IL phase loading > 4 wt. %. The increased IL loading led to a decrease in activity, which indicated that the catalyst was operating under mass transfer limitations.

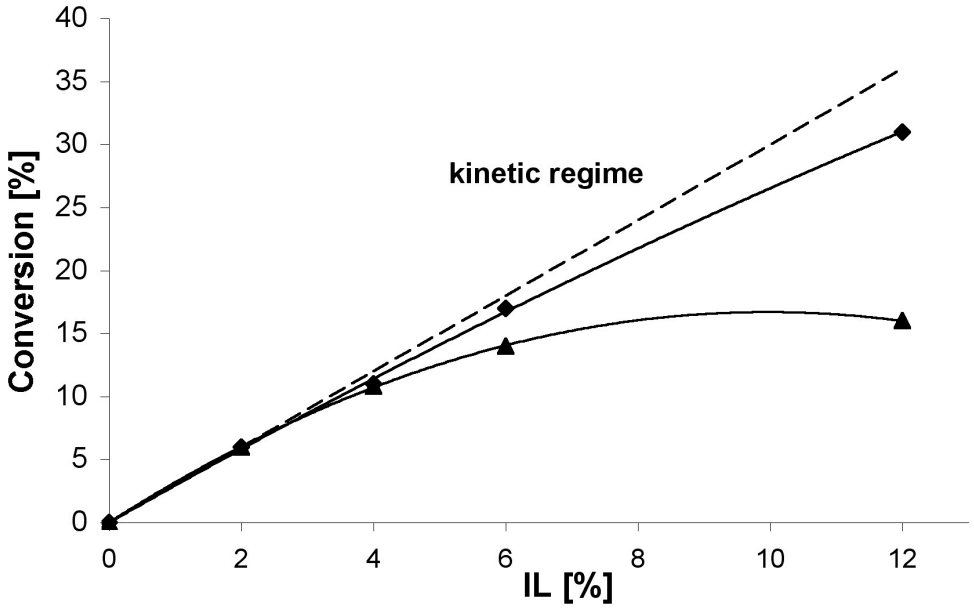

Figure 5.7: Conversion of 1,3-cyclohexadiene as a function of the loading of IL plus the Rh catalyst (0.9 wt.% Rh in IL, PPh_3/Rh ratio 8, HBF_4/[bmim][BF_4] ratio 0.5) on the supports ♦ CNF/SMF$_{Inconell}$ and ▲ SMF$_{Inconel}$.

These results explained the observed difference in catalytic activity and its dependence on the SMF supports. As seen in table 5.1, for the same catalytic system supported on SMF$_{Inconel}$, the specific reaction rate was always lower than that of the CNF/SMF$_{Inconel}$ support (entries 3, 5 and 9, 10). The same phenomenon was observed for SMF$_{Fecralloy}$ support compared to ZSM-5/SMF$_{Fecralloy}$ (entries 11 and 12). The latter catalyst showed higher activity, which could also be due to the formation of the thinner and homogeneous IL film detected by SEM, as on the CNF/SMF$_{Inconel}$ support. Thus, the

thinness of the IL layer decreased the influence of the mass transfer. Nevertheless, the same catalytic system on CNF/SMF$_{Inconel}$ support (entry 5) provided higher activity and selectivity compared with ZSM-5/SMF$_{Fecralloy}$ (entry 12). The effect of the nature of the support surface influenced somehow the Rh-complex activity. Indeed the chemical inertness of the CNF prevented any interaction between the support and the active species dissolved in IL. At the same time, the surface acidic groups of the zeolite coating could interact with the phosphine ligands, affecting the activity/selectivity of the catalytic system. Riisager *et al.* observed a similar phenomenon with a similar catalytic system [139]; they pointed out that the effect of the support was directly related to the irreversible reaction between the ligand with the acidic silanol surface group of the chosen support.

For the herein reported catalytic system, the effect of the ligand on catalysts activity and selectivity is explained in detail in 5.3.5.

5.3.4 Influence of the Acidity of the Catalytic Media

The observation that an excess of [H$^+$] activates the catalysts (see 5.3.2) gave an insight on the nature of the active species in the diene hydrogenation. Osborn and Schrock reported that the Rh$^+$ active center coordinated molecular hydrogen, giving catalytically active species [207], as described by the following equilibrium 5.2:

$$[Rh(H)_2L_n]^+ \rightleftharpoons RhHL_n + H^+ \tag{5.2}$$

In the herein reported catalytic system, providing an excess of [H$^+$], the equilibrium is shifted to the left, suggesting that the cationic dihydride is the active species, whereas the monohydride species gives poor catalytic activity. The classical Osborne cycle is based on the "hydride" mechanism for catalytic hydrogenation, in which reversible H_2 addition to the active catalyst is followed by the substrate biding and transformation.

To verify this hypothesis, a sulfonic acid functionalized IL, [bmimSO_3H][CF_3SO_3], was used as a solvent for the Rh complex. It appeared that even without the addition of an acid, the catalyst was active and selective toward the cyclohexene formation (Table 5.1, entry 13). This results is promising because the addition of acid to the IL phase can cause the decomposition of the IL itself. Strong HF can be formed, by the decomposition of the fluorinated anions. Of course HF is a very aggressive agent on the metallic supports and its formation should be avoided. The use of a functionalized IL allowed to overcome this

drawback, even if the catalytic activity was slightly lower than for systems with a great excess of $[H^+]$ (Table 5.1, entries 3, 9, and 13).

5.3.5 Influence of the Phosphine Ligand

The catalyst performance was found to depend on the presence of PPh_3 in the catalytic phase. The bottom part of table 5.1 presents activity and selectivity values for various PPh_3/Rh molar ratios. As seen, with a stoichiometric ratio, low activity and selectivity were observed (entry 6). Improved performance was achieved for ratios between 4 and 8. For PPh_3/ Rh ratio of 8, suitable activity and high selectivity (entries 9 and 10) were attained, comparable to the selectivity observed for this catalysts in non-supported IL [212].

The effect of the PPh_3/Rh ratio is shown in Figure 5.8. The donor character of the phosphine ligands under a hydrogen atmosphere enhances the yield of dihydride species [214]. Thus, this observation agrees with the hypothesis that the dihydride species (see Eq. 5.2) is the active one for the diene hydrogenation. Indeed, the addition of phosphine ligands would shift the equilibrium in favor of the dihydride complex.

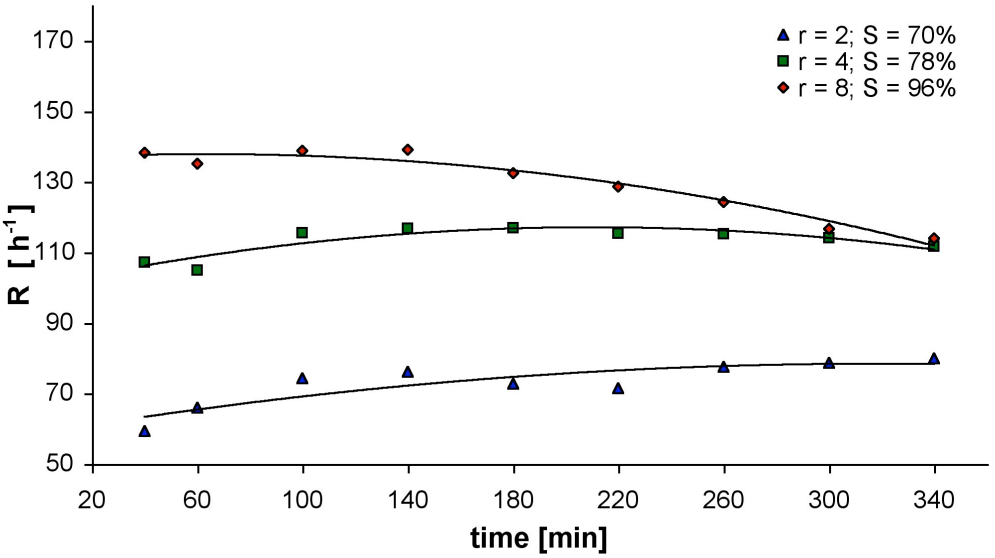

Figure 5.8: Dependence of the specific reaction rate R $[h^{-1}]$ on the PPh_3/Rh ratio, *r*. Catalyst: $[Rh(nbd)Cl]_2$ +PPh_3/[bmim][BF_4]/HBF_4 (Rh 0.06 wt.%, HBF_4/[bmim][BF_4] ratio 0.5) supported on $SMF_{Inconel}$.

A similar dependence of Rh-based SILP catalyst activity on the biphosphine ligand (sulfoxantphos) concentration was recently reported for continuous fixed-bed gas-phase hydroformilation of propene [139]. A relatively large excess of phosphine ligand was a prerequisite for active, highly selective and long-term stable SILP catalysts.

5.3.6 HP-NMR Characterization of the Catalytically Active Intermediate

NMR spectroscopy is a useful method to identify homogeneous catalytic intermediates. During this study, high-pressure NMR spectroscopy was used to identify the nature of the catalytically active rhodium species present in the SSILP under hydrogen at 100 bar.

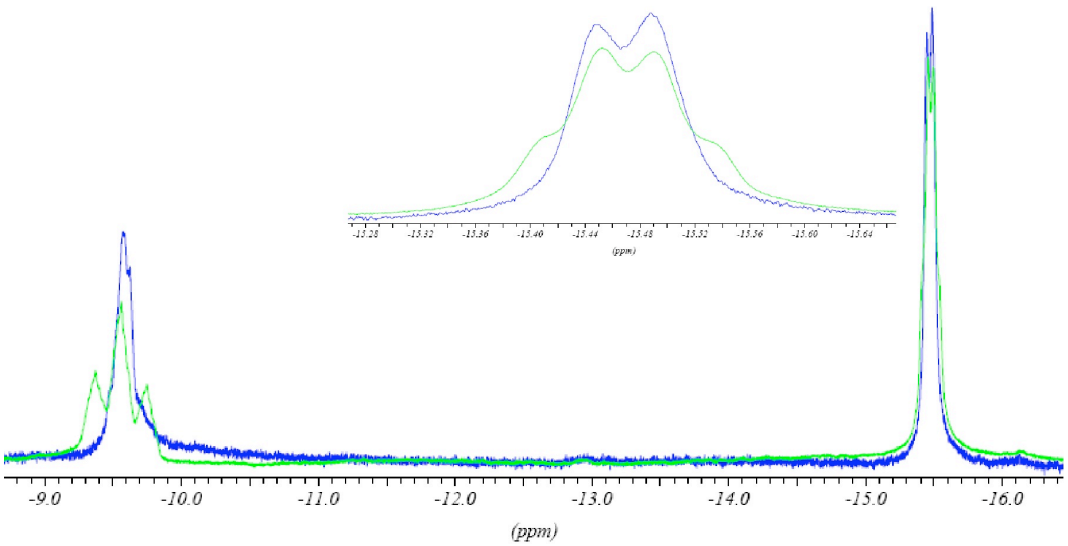

Figure 5.9: 400 MHz ^{1}H NMR spectra of the SILP phase, $[Rh(nbd)Cl]_2$ + PPh_3/bmimBF_4/HBF_4 (Rh 0.06 wt. %, PPh_3/Rh ratio 8, HBF_4/bmimBF_4 ratio 0.5), in acetone -d_6 under 100 bar H_2; green, ^{1}H NMR spectrum; blue, ^{1}H{^{31}P} NMR spectrum. For clarity, the peak at -15.5 ppm has been enlarged (inset).

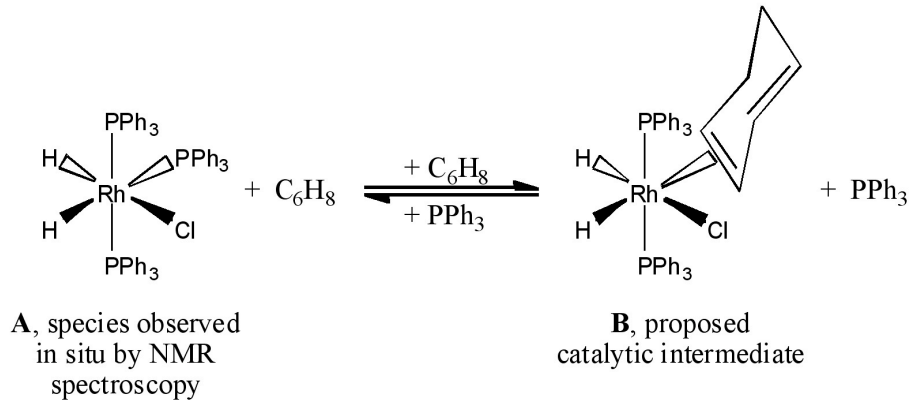

Figure 5.10: Proposed catalytically active rhodium species for the selective hydrogenation of 1,3-cyclohexadiene.

The ^{1}H NMR spectrum (Figure 5.9) exhibits a triplet at -9.6 ppm and a quartet at -15.5 ppm, which corresponds to $Rh(H)_2Cl(PPh_3)$ presented as **A** in Scheme 5.10, in agreement with literature data [215]. However, the coupling of the triplet is reduced in this experiment due to the presence of excess PPh_3, which is in rapid exchange with the PPh_3 ligand trans to the hydride. The structure of **A** was further verified by $^{1}H\{^{31}P\}$ NMR spectroscopy. It is reasonable to assume that the PPh_3 ligand trans to the hydride, that is in rapid exchange, is replaced by the cyclohexadiene substrate. Thus, **B** in the scheme 5.10 is the reaction intermediate. In the absence of acid, the catalyst rapidly decomposed, giving metallic Rh. This may explain the occurrence of catalyst deactivation without the addition of acid to the catalytic species.

5.4 Conclusions

In the herein reported study the developed SSILP Rh-based catalyst was shown to be active for the continuous-flow gas-phase hydrogenation of 1,3-cyclohexadiene, with high selectivity to cyclohexene. SMF plates with high porosity were used as structured supports. In an effort to improve the homogeneity of the IL film, the CNF/$SMF_{Inconel}$ were employed, due to their higher SSA compared to SMF itself. The thin IL film immobilized on CNF/$SMF_{Inconel}$, with large interface area, ensured the efficient use of the transition metal catalyst without mass-transfer limitations and isothermal conditions during the hydrogenation.

An excess of phosphine ligand and of acidic species in the IL phase was required to maintain catalyst activity and selectivity. The catalytic system based on a sulfonic acid functionalized IL, [bmimSO_3H]-

[CF_3SO_3], was proved to have the potential for the development of stable SSILP catalysts. The catalytic species active in the studied reaction was suggested to be $Rh(H)_2Cl(PPh_3)_3$, as follows from the high pressure ^{1}H NMR and $^1H\{^{31}P\}$ NMR spectroscopy results.

The SSILP catalyst, [$Rh(H)_2Cl(PPh_3)_3$/IL/CNF/$SMF_{Inconel}$], showed high selectivity (>96%) and TOF up to 250 h^{-1} with acceptable stability during 6 h on stream. The feasibility of the SSILP concept is therefore validated, showing the superior performance of CNF/SMF-based supports. The successful results of the herein reported study motivated us to apply the SSILP concept to Pd-based catalysts for the hydrogenation of acetylene (see Chapter 7) and to compare the novel catalytic system to IL-free catalysts (see Chapter 6).

Chapter 6

Monodispersed Pd nanoparticles supported on CNF/SMF$_{Inconel}$ for the Selective Hydrogenation of Acetylene

6.1 Introduction

The structure sensitivity of catalytic hydrogenation of unsaturated hydrocarbons over noble metal particles have already been reported [216–221]. A change of selectivity at higher turnover frequency (TOF) occur when the size of the metal particles increases. This change is explained by electronic and/or geometric effects caused by the change of the ratio of different types of metal surface atoms with variation in particle size. Larger particles possess crystal planes with atoms having high coordination numbers like terrace atoms. For small particles the surface atoms with low coordination numbers (edge and corner) predominate. When TOF is calculated not per total surface atoms but per a specific atom, the dependence of TOF on the particle size may disappear indicating which surface atoms are the active sites [222, 223]. These reactions are considered "structure sensitive" but size-independent.

Various interpretations have been offered to explain the structure-sensitivity of alkynes hydrogenations regarding the activity and the selectivity. Some reports propose the surface or subsurface carbon (Pd-C$_x$) to be responsible for the observed phenomena [161]. Recently, a detailed study on alkyne hydrogenation over Pd-catalysts demonstrated that the Pd-C$_x$ phase builds-up within the initial reaction stage and is responsible for the catalyst activity /selectivity [160]. The formation of a Pd-C$_x$ is suggested to be a

structure-sensitive reaction leading to the dependence of the catalytic properties on the size of the Pd nanoparticles. Moreover, carbonaceous overlayers on the Pd surface may serve as selectivity modifier by creating ensembles of different sizes with a variable numbers of surface atoms available for the adsorption. This leads to different adsorption geometries of the reacting molecules giving different reaction products.

The aim of the present Chapter is to report on the investigation about the size effect of acetylene hydrogenation over monodispersed Pd nanoparticles in the narrow region of 8-13 nm. Precise control over the particle diameter allows determining the critical particle size above which no size dependence of TOF is observed. Since gas-phase hydrogenations cannot be carried out over unsupported Pd nanoparticles, the composite material CNF/SMF$_{Inconel}$ was successfully applied, enabling thus the use of a continuous fixed-bed reactor. The mesoporous morphology of the CNF makes them excellent supports with low mass-transfer resistance. The strong interaction between the graphitic surface and the metal allows a direct deposition of the Pd nanoparticles without anchoring agents. Furthermore the strict temperature control during the highly exothermic acetylene hydrogenation is possible thanks to the suitable thermo conductivity of CNF/SMF$_{Inconel}$.

As illustrated in 2.5, one major issue of the reaction studied is the selectivity to ethylene. The control of the oligomerization of acetylene, which causes the deactivation of the catalyst by covering the metal surface with polyolefin (green-oil) is therefore crucial. The second part of this Chapter is dedicated to the effect of the CNF acidity on the catalyst performance. Acidity was increased by oxidative treatment of CNF/SMF$_{Inconel}$ with H_2O_2 or plasma-generated O_3 (see 4.4).

6.2 Preparation and Characterization of Pd Nanoparticles on CNF

Two methods for Pd deposition on CNF/SMF$_{Inconel}$ were used during this work, the catalysts and their characteristics are listed in Table 6.1.

Table 6.1: Characteristics of the catalysts used during the study. Dispersion was $^{(a)}$calculated by statistic method [223], $^{(b)}$measured by CO chemisorption.

Catalyst	Support	Pretreatment	Method of preparation	Pd loading [%]	Pd particle size [nm]	Pd dispersion [%]
A	CNF/SMF	-	ME	0.18	8	16.9^a
B	CNF/SMF	-	ME	0.18	11	13.7^a
C	CNF/SMF	-	ME	0.18	13	11.9^a
D	CNF/SMF	H_2O_2	ME	0.18	11	13.7^a
E	CNF/SMF	O_3	ME	0.18	11	13.7^a
F	CNF/SMF	H_2O_2	Ion exchange	0.15	5.5	19.8^b
G	AC	-	-	10	3.2	35.0^b

Catalysts A-E were prepared via impregnation of CNF/SMF$_{Inconel}$ supports with Pd nanoparticles colloidal solutions prepared beforehand following the procedure described in 3.3.2. This proposed method of preparation avoided the expensive energy/time-consuming calcination step and preserved the uniform particle size. More than 99.5% of surfactant could be removed during the washing procedure as reported by Semagina *et al.* [222]. Pd nanoparticles deposited on catalysts A-E were monodispersed (< 25% deviation from average size) as confirmed by HRTEM. The specimen sample observed by HRTEM consisted of supported Pd nanoparticles on CNF. They were previously reduced with 10 vol.% H_2 in Ar (total flow 150 ml(STP)/min) at 423 K for 1 hour, which was the same treatment performed *in-situ* before the catalytic measurements. They were then removed from SMF$_{Inconel}$ by ultrasonication bath in methanol for 2 h and then deposited on a carbon film of a copper grid used in the HRTEM. Figure 6.1 shows two HRTEM micrographs of the sample observed. A bundle of CNF with Ni particles on the top are visible. Ni particles are the catalyst for the CNF growth from the bulk Inconel, as explained in 4.3.2, and they do not detach from CNF/SMF$_{Inconel}$ support. The CNF structure correspond to a platelet-type with diameter up to 100 nm [15, 224]. The micrographs show the monodispersed 11nm-sized Pd nanoparticles deposited on CNF confirmed by *in-situ* EDX. Some smaller (5 nm) unsupported particles were also observed, but *in-situ* EDX analysis revealed the Fe nature of these particles, which most likely leached from SMF$_{Inconel}$ support during the ultrasonic treatment.

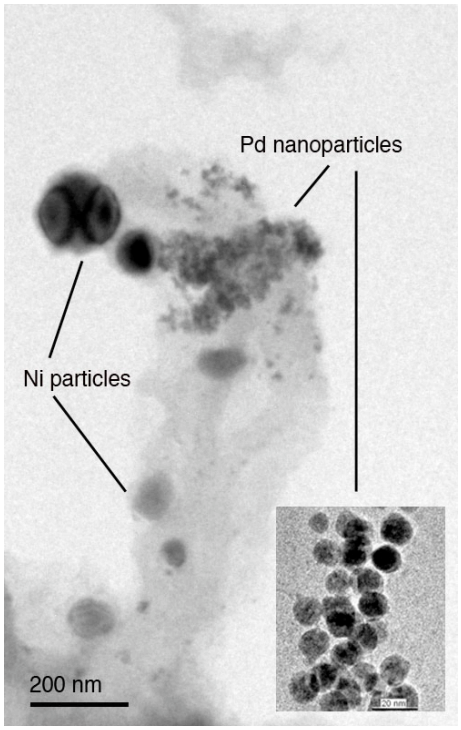

Figure 6.1: HRTEM micrographs of 11 nm-sized Pd nanoparticles supported on CNF.

The Pd crystallinity and particle size was also confirmed by XRD in a 2θ range of 35-90°, Figure shows the typical spectra obtained for ME synthesized Pd nanoparticles. XRD patterns at 2θ of 40°, 46.5°, 67.9°, 81.8°, 86.4° showed characteristic peaks of {111}, {200}, {311}, {222} planes of Pd f.c.c. structure, respectively. The calculation of the mean particle size was performed using Scherrer equation 6.1, where λ is the wavelength of the x-ray, $B_{\frac{1}{2}}$ is the full width at half maximum peak intensity (FWHM) and θ the diffraction angle. For the particles synthesized at water-to-surfactant ratios of 4 and 7, it gave values of 8.3 and 12.7 nm, respectively.

$$d = \frac{0.9\lambda}{B_{\frac{1}{2}} cos\theta} \tag{6.1}$$

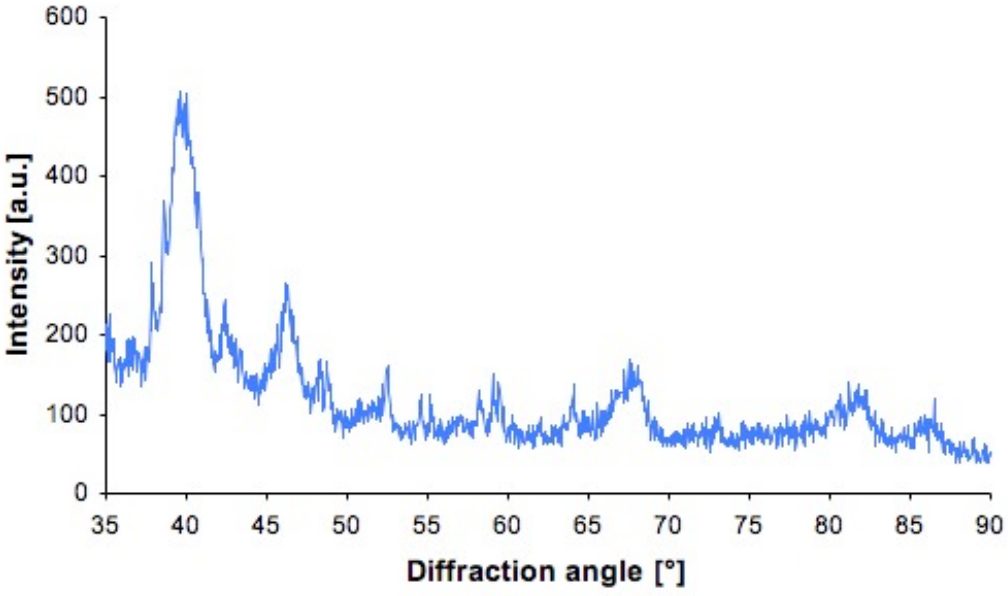

Figure 6.2: X-ray powder diffraction pattern of 13 nm-Pd nanoparticles synthesized with ME-technique

The Pd dispersion was calculated as the ratio between the total number of atoms of the particle (N_T) and the number of surface atoms (N_S) considering the statistic of the surface atoms on a f.c.c. max-B_5 crystallite [223]. The crystallite size parameter d_{rel} was determined as the ratio between the particle diameter d_p and the atom diameter d_a according to Eq. 6.2 and N_T in the crystallite according to Eq. 6.3

$$d_{rel} = \frac{d_p}{d_a} \tag{6.2}$$

$$N_T = \left(\frac{d_{rel}}{1.105}\right) \tag{6.3}$$

N_T can be calculated also from a polynomial in the number of atoms lying on an equivalent edge (m) as shown in Figure 6.3, so the m corresponding to each particle diameter has been determined and the number of surface atoms (N_S) could be calculated from the corresponding polynomial in m.

	m				
	3	4	5	6	>6
N_{BASIC}	201	586	1289	2406	$16m^3-33m^2+24m-6$
N_{AD}	24	102	240	438	$30m^2-132m+150$
N_T	225	688	1529	2844	$16m^3-3m^2-108m+144$
N_B	87	370	965	1974	$16m^3-33m^2-84m+210$
N_S	138	318	564	870	$30m^2-24m-66$
$N(C_4^{9,10})$	0	6	0	0	0
$N(C_5^7)$	24	0	0	0	0
$N(C_6^6)$	24	72	96	96	96
$N(C_7^5)$	24	72	120	192	$24(3m-10)$
$N(C_7^y)$	12	24	60	96	$12(3m-10)$
$N(C_8^{4,5})$	6	0	0	6	$6(m-5)^2$
$N(C_9^4)$	0	24	24	24	24
$N(C_9^3)$	0	24	96	216	$24(m-3)^2$
$N(C_{10})$	48	72	120	168	$24(2m-5)$
$N(C_{11})$	0	24	48	72	$24(m-3)$

Figure 6.3: Formulae for the numbers of different surface atoms for f.c.c. max-B_5crystallite [223].

Since the Pd nanoparticles were supported on CNF it was hypothesized that the face of the crystallite anchored to the support corresponds to the (111) plane; the number of atoms of one of these planes ($N_{3,9}$) was thus subtracted from the value of N_S and eventually the dispersion was obtained (see Table 6.1).

Catalyst F was prepared depositing Pd on activated CNF/SMF$_{Inconel}$ via ion-exchange as illustrated in 3.3.3, but in this case it was not possible to apply the same statistical method to calculate Pd dispersion because a particle size distribution was observed. Pulse CO chemisorption measurements at 323 K allowed estimating the metal dispersion after the reductive treatment with 10% H_2 in Ar (total flow 150 ml(STP)/min) at 448 K overnight. A sequence of pulses of 3% CO in He (injection loop volume between 0.5 and 1 ml at 383 K) was sent to the reactor shown in 3.4.9 , and the injection was stopped when the detector measured 3 identical pulses in a row. This means that the Pd surface is saturated with CO and the difference between the mol of CO injected and measured at the outlet gives the quantity of CO adsorbed on the surface. The particle size has to be considered as an average using the number of Pd atoms exposed on the surface layer.

6.3 Catalytic Performance of Pd Nanoparticles on CNF/SMF$_{Inconel}$

6.3.1 Reaction conditions

After a proper calibration of the MFC, the reaction mixture of 2 vol% of C_2H_2, 4 vol% of H_2 in Ar (total flow 700 ml(STP)/min) was used throughout the study and fed to the catalytic reactor. The low ratio of C_2H_2/H_2 was chosen in order to limit the formation of coke on the catalyst surface which is maximum when the ratio is close to one [179]. The temperature was maintained constant at 423 K and the pressure at 1.04 bar.

In order to compare the activity of the different catalysts, the concept of turnover frequency (TOF) has been adopted according to Eq.6.4 where the number of active sites is the number of Pd atoms in contact with the gas-phase.

$$TOF = \frac{nb_{molecules_{C_2H_2}reacted}}{nb_{activesites} \cdot s} \tag{6.4}$$

The number of active sites was calculated using the dispersion of the catalysts described in 6.2:

$$n_{activesites} = \frac{m_{cat} \cdot w_{Pd}}{MM_{Pd}} \cdot dispersion \tag{6.5}$$

Eventually the activity can be expressed as a function of the reaction rate (Eq. 3.10):

$$TOF = \frac{-R_{C_2H_2} \cdot MM_{Pd}}{dispersion} \tag{6.6}$$

6.3.2 Size Sensitivity of Acetylene Hydrogenation

During the acetylene hydrogenation over Pd nanoparticles, the activity increases with particle size up to 5 nm. Above 5 nm no important changes occur in the fraction of exposed atoms, however, the activity is still reported to increase [216, 218]. Borodzinski [159] reported the activity increase with Pd size up to 26 nm over Pd/SiO_2 catalyst with Pd diameter of 4, 5, 7, 16, and 26. It is important to note that all studies on the size-effect during acetylene hydrogenation have been carried out with polydispersed Pd nanoparticles. Indeed different preparation methods and different support natures, together with nanoparticle size distribution may disguise the size-effect. Important advances in colloidal preparation of metal nanoparticles bring new opportunities for studies on the size-effect relations.

The Pd size effect on the acetylene hydrogenation was studied over monodispersed particles of 8, 11 and 13 nm prepared by ME-method. As showed in Figure 6.4 , the initial TOF (calculated by means

of the equation 6.6 at 20 minutes on stream) of acetylene hydrogenation increased with particle size from 8 to 11 and practically did not change from 11 to 13 nm. At particle size greater than 5 nm Pd shows bulk-metallic electronic properties [216,218], so the electronic effect cannot explain this behavior. Nevertheless at lower Pd dispersion the "geometric effect" can still influence the activity of the catalyst, indeed carbonaceous deposit on the metal surface, formed in the initial stage of the reaction, diminishes the surface available for the adsorption of acetylene [169]. Recently, it has been confirmed that the carbon deposition and the formation of a Pd-C_x surface phase are structure-sensitive reactions [160]. On smaller particles the ratio between surface C and Pd is higher, the available surface for the reaction is restricted and consequently the observed TOF are lower. Therefore, in line with the hypothesis of Borodzinsky [159], the herein reported results suggests the "geometric factor" as the most probable cause for the antipathetic structure-sensitivity of the acetylene hydrogenation over Pd catalysts.

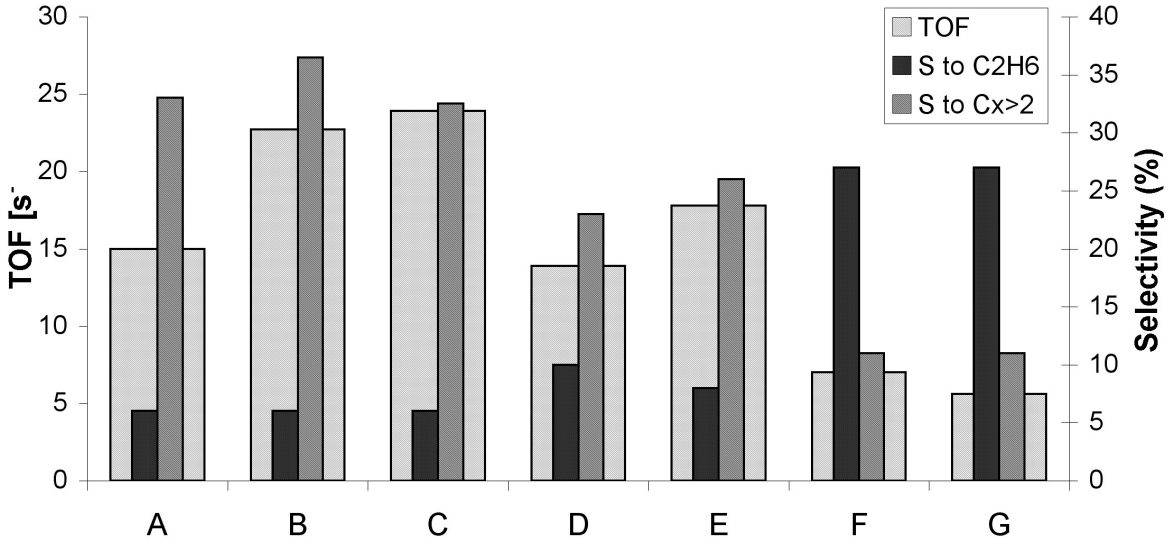

Figure 6.4: Initial turnover frequency and selectivity toward ethane and oligomers at 20 minutes on stream. 423 K, total flow 700 ml(STP)/min (2% C_2H_2, 4% H_2 in Ar).

As showed in Table 6.2, the TOF of the reaction carried out with 11 and 13 nm particles were almost the same. This result proved that 11 nm is a "critical" size above which nanoparticles' specific activity is not size-dependent. It was a significant finding, as it allowed to specify the size at which Pd nanoparticles show bulk catalytic activity in acetylene hydrogenation. A similar approach was recently applied to the 1-hexyne hydrogenation [225], where unsupported 14 nm particles approached Pd-black in catalytic ac-

tivity. This again confirms the "geometric factor" governing the size-sensitivity: the optimal adsorption of larger 1-hexyne molecules requires more space on Pd surface than acetylene.

Table 6.2: Catalytic performance of the samples tested for acetylene hydrogenation at 423 K, total flow 700 ml(STP)/min (2% C_2H_2, 4% H_2 in Ar).

Catalyst	**Initial TOF [s^{-1}]**	**Initial conversion [%]**	**Initial selectivity [%]**
A	15	36	61
B	23	47	59
C	24	43	62
D	14	31	64
E	18	39	64
F	7	24	60
G	6	20	62

The network of reactions taking place during the hydrogenation of acetylene is depicted in Figure 6.5, where three possible paths are outlined. The desired product ethylene is obtained via path **a**. The over-hydrogenation of acetylene takes place via the consecutive ethylene hydrogenation or in parallel via path **b** directly to ethane. The products distribution was analyzed in terms of selectivities towards the different products during the initial stage of the reaction, because the catalysts are known to deactivate over time due to the green-oil deposition. The initial selectivity to ethylene (after 20 min on stream) was 60$\pm$2%, as shown in Table 6.2 for catalysts A, B and C, independently on the Pd dispersion. The results were in line with the reported for 1-hexyne hydrogenation, where the selectivity did not change with particle size [225]. As shown in Figure 6.4 for catalysts A, B, and C the byproducts distribution was also independent on the Pd dispersion. These results suggests that the particle size does not change the reaction mechanism and/or the adsorption mode of acetylene and ethylene during the initial stage of the reaction. The "geometric" nature of the size effect was thus furthermore confirmed.

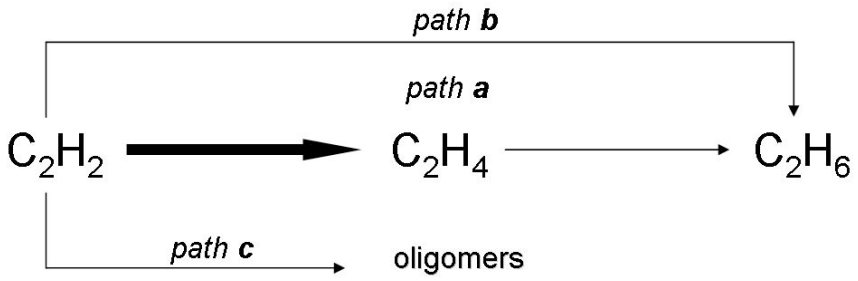

Figure 6.5: Scheme of the mechanism of acetylene hydrogenation [153]

6.3.3 Influence of the Support on the Catalytic Behavior

The nature of the catalyst support is known to influence the catalytic behavior introducing a different morphology and surface chemistry [226]. However, studies of the catalyst support effect are often complicated due to the difference in active metal dispersion. In this work, Pd nanoparticles of 11 nm were prepared via microemulsion technique and then deposited on differently activated CNF supports (see Table 6.1, catalysts B, D and E). As the Pd dispersion was kept constant, the effect of the catalyst support on the catalytic properties can be observed.

After the oxidative treatment (see 4.4), the total acidity of the catalyst supports D and E increased. Carboxylic, quinone and lactone groups are acidic, while phenolic, carbonyl and ether groups are weakly acidic to neutral. Since the catalytic test have been performed at 423 K in presence of H_2, the support functionality could be different compared to the fresh one. Therefore, the TPD profile shown in 4.4, Figure 4.8, of two supports (pretreated with O_3 and H_2O_2, respectively) have to be compared after treating them at the reaction conditions. The results are shown in Table 6.3 and Figure 6.6. The difference between the two samples in yield of O-groups evolving CO_2 during TPD was negligible after the reduction, most probably because during the reductive treatment at 423 K part of the functional groups created by oxidation with O_3 was decomposed. It can be therefore concluded that under the reaction conditions applied the O_3-pretreated supports become slightly less acidic than the H_2O_2-pretreated ones. This is an important findings, because it shows how the support functionalities can change with the different reactive conditions applied to the catalyst.

Table 6.3: Concentration of CO and CO_2, [mmol g^{-1}], released from CNF/SMF$_{Inconel}$ during a) TPD after oxidative treatment, b) TPD after oxidative treatment and subsequent reduction at 423 K

Activation	CO$^{a)}$	CO$^{b)}$	$CO_2$$^{a)}$	$CO_2$$^{b)}$
plasma-generated O_3	3.6	2.3	2.9	1.2
boiling aqueous H_2O_2	4.3	3.3	1.4	1.1

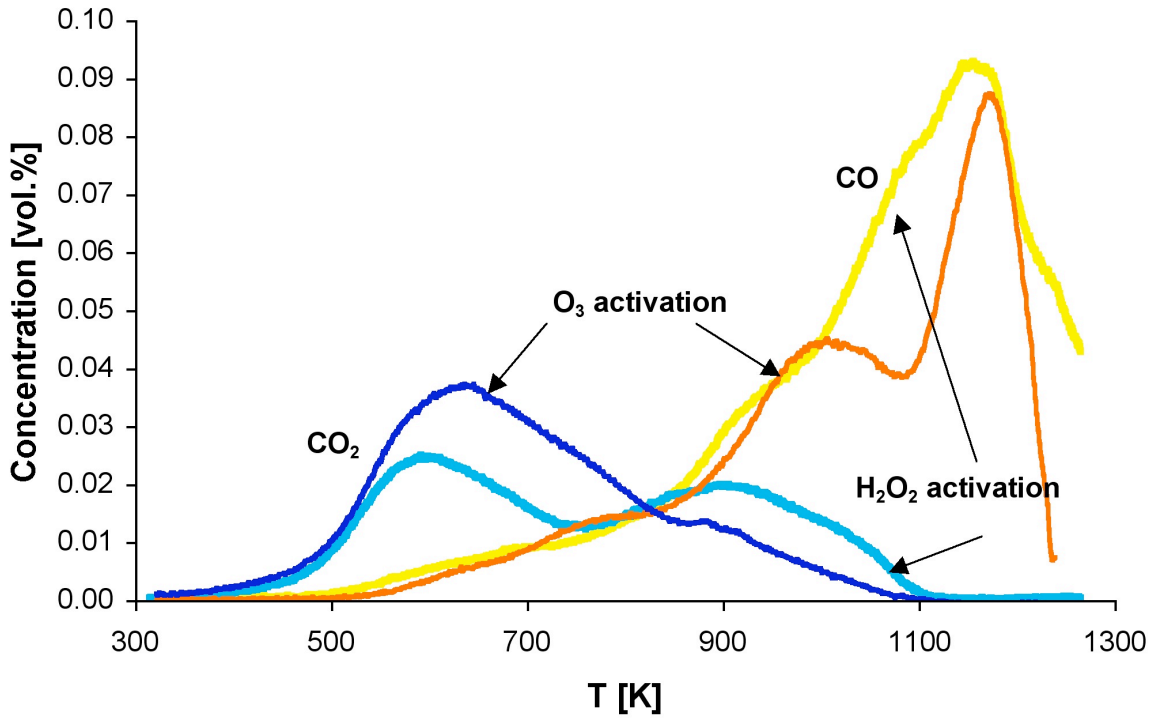

Figure 6.6: TPD profiles of CNF/SMF$_{Inconel}$ samples (0.1 g) activated with plasma-generated O_3 at room temperature for 30 min and with boiling 35% aqueous solution of H_2O_2 for 4 hours, after reduction in 10% H_2 in Ar (total flow 150 ml(STP)/min) at 423 K for 2 hours.

As shown in Table 6.2 and Figure 6.4 for catalysts B, D and E the more the catalyst was "acidic" the less it was active. Due to the lower electronic density induced on the surface of CNF by the activation [93], the electronic properties of the supported Pd nanoparticles might be affected, thus increasing the complexation of acetylene molecules. This might cause the decrease of reaction rate, resulting in lower TOF observed. These results are in line with the reported pulse-flow results for propyne hydrogenation

over acidic Pd/SiO_2 and neutral Pd/Al_2O_3 catalysts with 33% and 29% Pd dispersion, respectively [227]. During the initial reaction period, Pd/SiO_2 showed 60% lower TOF than the alumina-based catalyst.

The initial selectivity to ethylene and the byproducts distribution were also analyzed for catalysts B, D and E in order to elucidate the influence of the support acidity when Pd particle size was kept constant. As shown in Table 6.2 and Figure 6.4, it was found that the selectivity to ethylene was slightly higher on "acidic" catalysts. At the same time a smaller amount of oligomers was formed. These results are again in line with the pulse-flow results for propyne hydrogenation [227] which reported that the "acidic" catalyst retained 3 time less carbon on its surface after 1 pulse of propyne and 16 time less after reaching a steady-state. Similarly, as shown for Pd nanoparticles deposited on differently treated activated-carbons by the inelastic neutron scattering technique [228], the higher is the carbon acidity, the less carbonaceous deposits are formed. The herein observed effect of acidity on the catalyst activities can be rationalized considering a change in the adsorption strength of acetylene due to lower electronic density on the activated CNF (see 6.3.2). Indeed on "acidic" catalysts the strength of the acetylene adsorption is enhanced compared to the ethylene's one, so the over-hydrogenation via path **a** (Figure 6.5) decreases and the selectivity to ethylene slightly increases. It can be assumed that acetylene adsorption mode changes as well, so the surface intermediates which are supposed to be transformed to ethane via path **b** [153, 161, 229] are preferentially formed diminishing the formation of green-oil via path **c**. The concentration of these species on the catalyst surface during the acetylene hydrogenation should be studied *in-situ* in order to confirm this aspect.

6.3.4 Catalyst Deactivation

Figure 6.7 shows the relative reaction rate evolution during the first 70 minutes on-stream of the acetylene hydrogenation. The catalyst A, B and C, prepared by ME technique, exhibited higher deactivation rate than catalyst F prepared by ion-exchange. This can be attributed to residual, sulfur-containing AOT surfactants on the Pd surface. Presence of sulfur on the Pd surface is known to promote isomerization/oligomerization compared to over-hydrogenation [230]. On the contrary, sulfur-free catalyst F deactivated much slower. Furthermore, the organic molecules may serve as first layer of hydrocarbonaceous deposit which accelerated the formation of further layers.

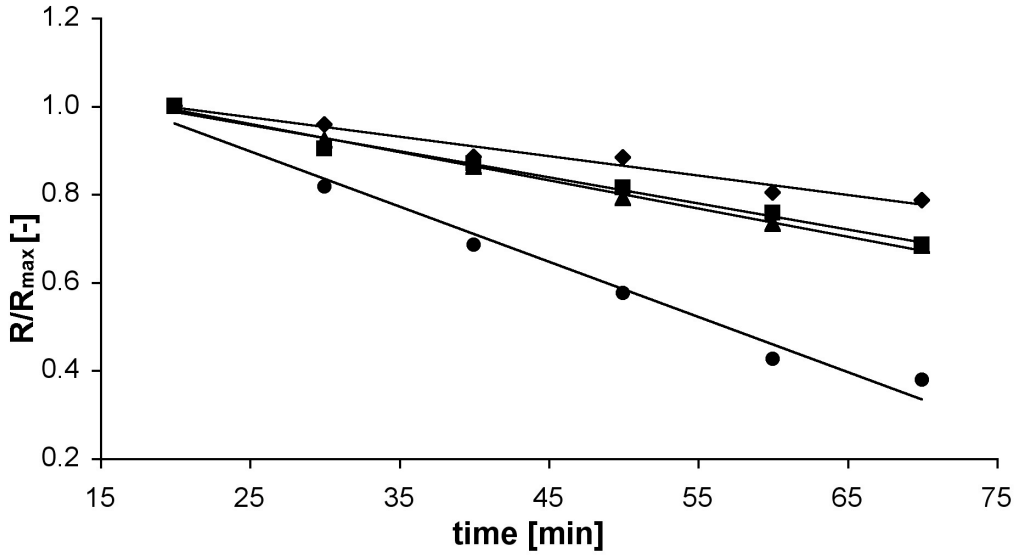

Figure 6.7: Ratio of reaction rate (R) over initial reaction rate (R_{max}) for catalysts • A, ■ B, ▲ C, ♦F and for the first 70 minutes on stream at 423 K, total flow 700 ml(STP)/min (2% C_2H_2, 4% H_2 in Ar)

Comparing the three catalysts A, B and C, prepared with the same technique but with different Pd particle size, it is clear that smaller particles (8 nm) deactivate faster because the available surface is rapidly covered by green-oil, while particles of 11 and 13 nm deactivate slower. Interestingly, the deactivation of nanoparticles with size above 11 nm was not size-dependent.

Figure 6.8 presents the products distribution over aged catalysts (after 6 hours on-stream). The selectivity to ethylene decreased drastically for catalysts A-C as compared to the initial one reported in Table 6.2, mostly in favor of ethane formation. Interestingly, the "acidic" catalysts D and E showed, after aging, a much lower decrease in selectivity to ethylene, but to ethane it increased up to $\sim$30% concomitant with less oligomers formation. For catalysts F and G the selectivity remained at its initial value. It is known that upon aging the accumulation of hydrocarbonaceous species causes the spillover of hydrogen to the adsorbed species and the rate of hydrogenation of ethylene to ethane (path **a**, Figure 6.5) increases [153, 161]. Larsson et al. proposed that coke formed on the catalyst could be of two types [178]: one harmful (formed in the lack of hydrogen) which causes the formation of ethane via path **a**, and another harmless which does not modify the selectivity. It can therefore be assumed that harmful coke formed much more on non-"acidic" catalysts and did not form at all on catalysts F and G. As was shown for the initial period, oligomers forms much less on the "acidic" catalysts, so the hydrogen spillover should be

less pronounced. The enhanced ethane formation is therefore supposed preponderant via path **b** (direct over-hydrogenation of acetylene to ethane), instead of path **a.**

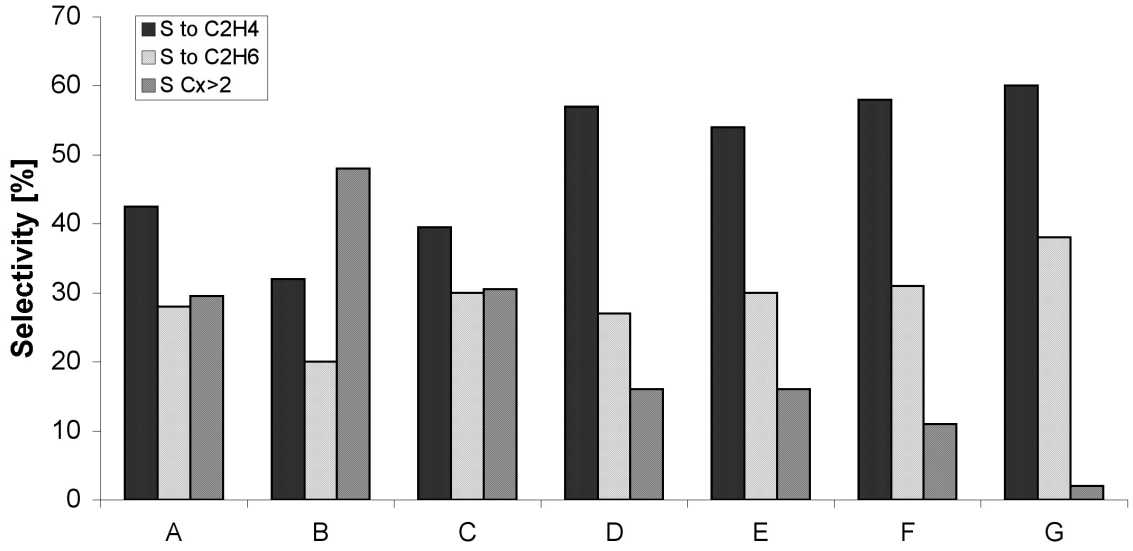

Figure 6.8: Distribution of products at 6 h on-stream represented as catalyst selectivities to ethylene, ethane and oligomers during acetylene hydrogenation. 423 K, total flow 700 ml(STP)/min (2% C_2H_2, 4% H_2 in Ar).

The need of lower quantity of oligomers for maintaining high selectivity to ethylene was confirmed by catalyst F and G, since they did not show any change in selectivity to ethylene after 6 hours on-stream due to twice lower oligomers formation than ME-derived catalysts.

6.4 Conclusions

During the work described in this Chapter monodispersed Pd nanoparticles, prepared from reverse ME and supported on CNF/SMF$_{Inconel}$, were applied for studying the size effect during acetylene hydrogenation. TOF was found to increase from 15 s^{-1} to 24 s^{-1} with particle size increasing in the range of 8-13 nm. The 11nm-diameter was found to be "critical", above which nanoparticles' specific activity is not size-dependent. The size effect below 11 nm was suggested to be "geometric" in nature, due to the size-sensitive formation of a Pd-C_x phase. For smaller particles the C/Pd ratio is higher and carbonaceous deposit might block part of the active Pd surface. The products distribution was found independent on particle size confirming the "geometric" nature of the size-effect.

The deactivation of Pd, due to the green oil formation, was found to vary with the particle size and the presence of sulfur traces coming from AOT-surfactant used during the ME-preparation of the nanoparticles. Smaller particles (8 nm) deactivated faster than the bigger ones (11-13 nm). The catalysts based on ME-derived nanoparticles deactivated faster than the catalysts with Pd deposited by ion-exchange.

The influence of the support nature on the catalytic activity was investigated by comparing the initial TOF of 11 nm Pd nanoparticles supported on differently modified CNF/SMF$_{Inconel}$. The initial TOF was found to decrease with increasing acidity of the CNF surface, while the selectivity to ethylene slightly increased. The byproducts (ethane and oligomers) distribution was found shifted toward the ethane formation on "acidic" supports. The observed effects were attributed to the lower electronic density of the activated CNF, which might affect the strength and mode of acetylene adsorption.

After 6 hours on stream, coke formation on the catalyst caused a decrease in activity and selectivity to ethylene. This decrease was less pronounced for CNF-based supports with higher acidity, obtained by oxidative pre-treatment with H_2O_2 or with plasma-generated O_3.

Chapter 7

SILP Pd Nanoparticles on CNF/SMF$_{Inconel}$ for the Selective Hydrogenation of Acetylene

7.1 Introduction

Supported Pd-based catalysts are the most widely used for the selective hydrogenation of acetylene (see 2.5.3). They are object of intensive investigation, especially to increase the selectivity of the process, to generate richer streams in ethylene and to suppress the catalyst deactivation due to the acetylene oligomerization [157, 173, 174, 221]. In the previous Chapter it was shown how the catalytic activity, selectivity and stability of supported Pd nanoparticles are strongly influenced by the nature of the support material and by the preparation method. Indeed, the application of Pd nanoparticles with a narrow size distribution is very important because the acetylene hydrogenation has been proved to be structure sensitive (see 6.3.2), in agreement with the literature available [159, 216, 217, 220]. However, nanoparticles need to be stabilized because they tend to aggregate thus loosing their catalytic properties. Several methods have been studied to achieve a complete stabilization, as elegantly summarized by R.G. Finke [231]. Most recently, transition metal nanoparticles with a narrow size distribution have been synthesized in imidazolium-based IL and applied to various multiphase catalytic processes (see 2.4.2). The IL acts in this case as a template for the formation of nanoscale structures and stabilizes the metallic surface by the formation of "protective" anionic and cationic layers [116]. The application of Pd nanoparticles in imidazolium-based IL is very promising for the selective hydrogenation of

acetylene, but, in order to use a fixed-bed reactor for the continuous gas-phase process, a heterogeneous catalytic system is required. The SILP concept can be suitable in this case, because it minimizes the use of IL [128, 130, 131, 134, 205, 232]. In Chapter 5, the successful application of SILP catalyst on CNF/SMF$_{Inconel}$ structured supports was demonstrated for gas-phase hydrogenations. The advantage of such a configuration, besides a low pressure drop through the reactor and an even flow distribution, consisted in the homogeneity and stability of the SILP layer, isothermal conditions during the exothermic evolution of the reaction, and the absence of chemical interaction between the support and the SILP catalyst. Following the positive results obtained for the hydrogenation of 1,3 cyclohexadiene with the SILP Rh-based catalyst, it was decided to test the SILP concept for the selective hydrogenation of acetylene.

The study reported in this Chapter aimed on the application of Pd nanoparticles, prepared in SILP on CNF/SMF$_{Inconel}$, to the hydrogenation of acetylene. Two different imidazolium-based IL have been used, in order to find a more effective way to synthesize the nanoparticles directly on the support and to elucidate the influence of the IL nature on the catalytic activity toward the chosen reaction. Furthermore the NMR technique has been used to determine the gas solubilities in [bmim][PF_6] and to clarify the mass transfer from the bulk gas flow to the catalytic active phase on the support.

7.2 Characterization of the SILP Catalysts

The SILP catalysts used through this study were prepared following the procedure described in 3.3.4.

7.2.1 Support Morphology and Comparison between Pd/[bmim][PF$_6$] and Pd/[bmimOH]-[Tf$_2$N]

The morphology of the IL layer on the CNF was observed at SEM for different IL loadings on the support. Figure 7.1 shows that at low IL loading it is possible to maintain the mesoporous structure of the CNF network (Fig. 7.1A), while increasing the IL content the CNF are completely submerged by the liquid (Fig. 7.1 C). At higher magnification (Fig. 7.2) one can better observe the difference in porosity between IL loading of 3 wt.% and 6 wt.%. For slow reaction kinetics, when the reactants have sufficient time to diffuse into a thicker layer of liquid the configuration of Fig. 7.1 C is preferred because it provides higher quantities of the active phase on the support, while maintaining the homogeneity of the IL layer [233]. For fastest kinetics, as for the acetylene hydrogenation, the morphology of Fig. 7.1A/B is better because it provides a higher surface area in contact with the gas phase and a thinner layer of IL where the Pd nanoparticles are embedded.

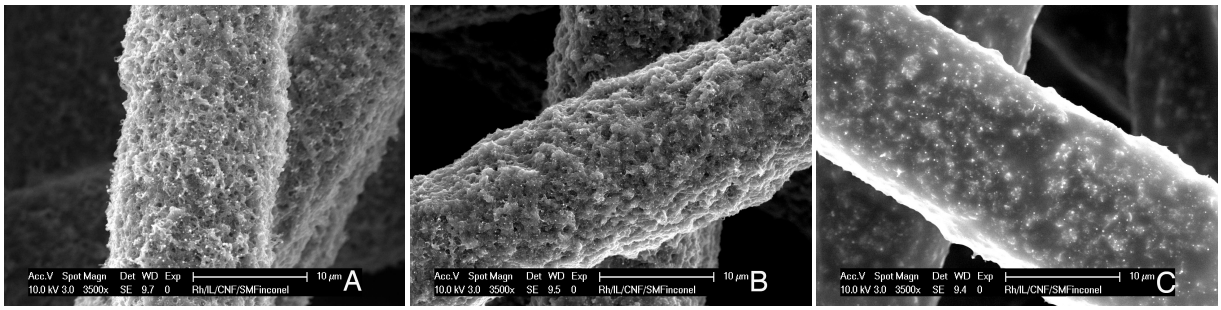

Figure 7.1: SEM micrographs (3500x) of IL/CNF/SMF$_{Inconel}$ fibers with different IL loadings: A) 3 wt.%, B) 6 wt.%, C) 9 wt.%

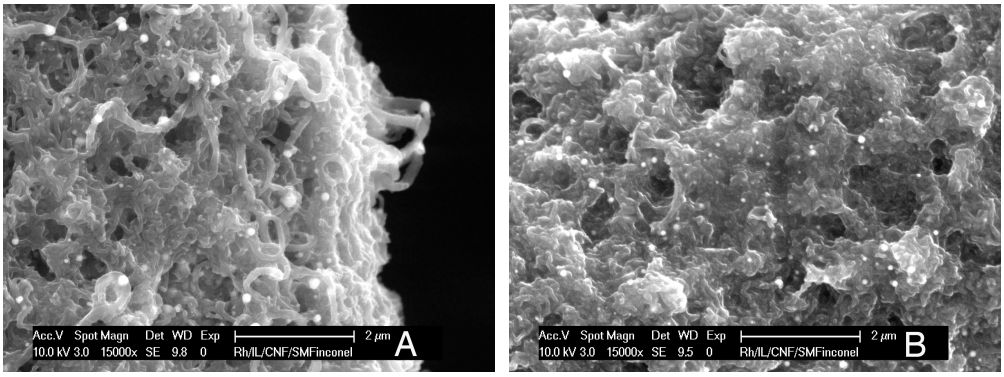

Figure 7.2: SEM micrographs (15000x) of IL/CNF/SMF$_{Inconel}$ fibers with different IL loadings: A) 3 wt.%, B) 6 wt.%.

Figure 7.3 shows HRTEM images of Pd nanoparticles (confirmed by in-situ EDX) with a narrow size distribution formed in the two systems studied. The reduction of Pd(acac)$_2$ with H_2 in [bmim][PF_6]/CNF/-SMF$_{Inconel}$ gave 10 nm-sized particles, while without adding H_2 in [bmimOH][Tf_2N]/CNF/SMF$_{Inconel}$ the reduction process afforded 5 nm-sized particles.

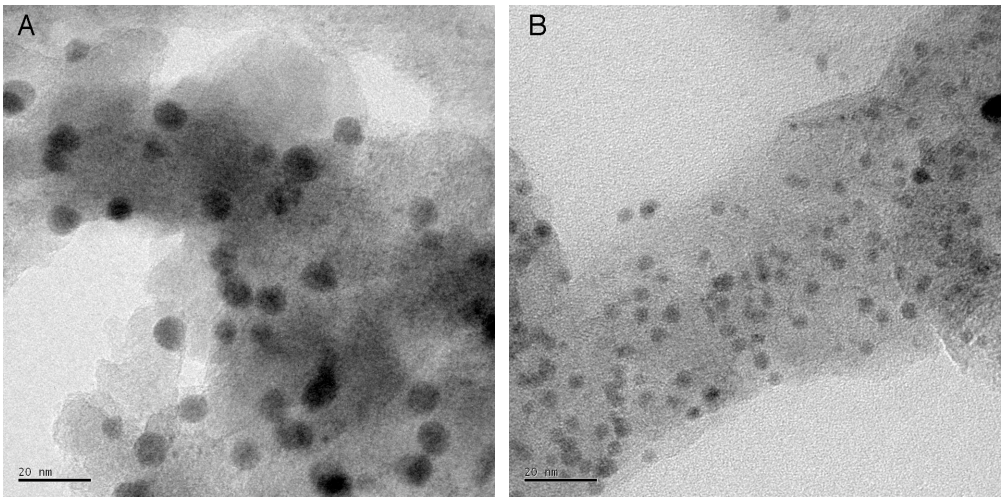

Figure 7.3: HRTEM micrograph (120000x): A) 10 nm-sized Pd-nanoparticles formed in [bmim][PF_6]/CNF/SMF$_{Inconel}$, B) 5 nm-sized nanoparticles formed in [bmimOH][Tf_2N]/CNF/SMF$_{Inconel}$.

The OH-functionality of the imidazolium moiety was hypothesized responsible for the formation of nanoparticles, via a redox reaction with the metal ions Pd(II) precursor, as depicted in Scheme 7.4

adapted from [234]. The formation of Pd nanoparticles was thus achieved and stabilized in IL-phase without the intervention of an external reducing agent, similarly to the polyol reduction process [235].

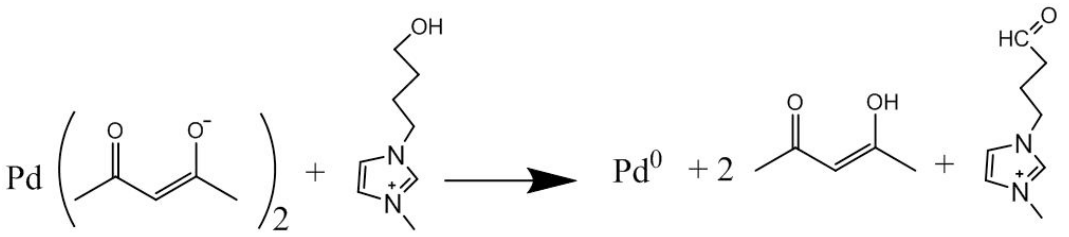

Figure 7.4: Hypothesized Pd(acac)$_2$ reduction to Pd^0 by the alcohol functionality of the imidazolium moiety.

The supramolecular structure of IL provided a good protection against agglomeration, thanks to the anionic and cationic layer surrounding the nanoparticles [236, 237]. It has recently been demonstrated that the IL anions have the highest influence in the stabilization of metal nanoparticles and that the particle size can be related to the molecular volume of the anion [116, 117]. In our case this is true for particles formed in [bmim][PF_6] because the anions form the first shell around the electrophilic particle, according to the DLVO theory [238]. In [bmimOH][Tf_2N] the carrier for the coordination center is the imidazolium cation, since the hydroxylic group is responsible for the formation of the nanoparticles. Thus, the order of the ionic layers surrounding the particle during its nucleation and growth may change and the molecular volume of the anion can no longer be related with the particle size. As a result, smaller clusters than expected were formed. Nevertheless the DLVO model cannot extensively describe the stabilization properties of the IL, since it treated counterions as point charges and was not designed to account for sterically stabilized systems [239].

7.2.2 NMR Determination of the Reactant/Product Solubility in [bmim][PF_6]

The solubility of C_2H_2, C_2H_4, C_2H_6 in [bmim][PF_6] was determined using ^{13}C and ^{1}H NMR spectroscopy (see 3.4.10) at a pressure of 1 atm and at two temperatures 298 K and 348 K, in order to be as close as possible to the reaction conditions (see 7.3). The integral of ^{13}C and ^{1}H peaks in relation to the peak corresponding to the CH_2 carbons of the butyl chain or the two 4,5 CH protons of [bmim][PF_6] was determined by a non-linear least-squares iterative fitting application. The results are presented in Table 7.1 as the measured gas concentrations in IL, where the errors were estimated from five parallel experiments.

Table 7.1: Measured concentrations of dissolved gas under 1 atm pressure in [bmim][PF_6] at 298 K and 348 K.

Gas	Mole fraction $\cdot 10^{-3}$at 298 K	Mole fraction $\cdot 10^{-3}$at 348 K
Acetylene	74±7	57±6
Ethylene	6.5±2	2.8±1
Ethane	3.5±1	1.6±1

Following the general trend of gas solubility in liquids, the three gases were found less soluble as the temperature increased, corresponding to an exothermic solvatation process. When comparing the concentrations in IL, the trend C_2H_2 > C_2H_4 > C_2H_6 was observed. The results for ethylene and ethane are consistent with available literature data: Anthony *et al.* measured the solubilities by gravimetric microbalancing [143], while Camper *et al.* used an apparatus for measuring the pressure difference while injecting the gas in a chamber containing IL [240]. To the best of our knowledge, the herein reported measurements are the first attempt to measure the solubility of acetylene in IL. Indeed, the amount of dissolved acetylene was found more than ten times higher than that of ethylene, confirming that hydrocarbons with the same number of carbon atoms but with increasing saturation show lower solubility in [bmim][PF_6]. As previously observed by Umpierre *et al.* for the hydrogenation of 1,3-butadiene, the difference of solubility in IL between the highly unsaturated reactant and the intermediate/target product of a consecutive hydrogenation has a positive effect on the selectivity of the reaction taking place in the IL phase [236]. The herein reported results encouraged thus the use of the SILP nanoparticles applied to the selective hydrogenation of acetylene.

7.3 Catalytic Performance for the Hydrogenation of Acetylene

After a proper calibration of the MFC, the reaction mixture of 4 vol.% of C_2H_2, 4-30 vol.% of H_2 in Ar was used throughout the study and fed to the catalytic reactor. The temperature was set between 343 K and 423 K and the pressure at 1.04 bar. The catalytic activity was expressed in terms of specific reaction rate, R, as the moles of acetylene converted *per* second and *per* gram of Pd on the catalyst.

7.3.1 Catalyst Activity and Stability

The catalytic system based on SILP Pd nanoparticles on CNF/SMF$_{Inconel}$ was found active toward the studied reaction in both IL tested (see Table 7.2). Although analogous specific reaction rates were observed for IL-free Pd nanoparticles supported on CNF/SMF$_{Inconel}$ (see Chapter 6), on Pd-SILP catalysts acetylene was converted only to ethylene and ethane, as confirmed by molar balance from the GC analysis. The oligomerization of acetylene to green-oil ($C_{x>2}$), which is known to deactivate the catalyst [157, 173], was not observed. Consequently the activity and selectivity did not change significantly over 6 hours on-stream (as shown in Figure 7.5).

Table 7.2: Characteristics of Pd/IL/CNF/SMF$_{Inconel}$ catalysts for the hydrogenation of acetylene. Feed mixture 4 vol.% C_2H_2, 10-30 vol.% H_2 in Ar, Q_{tot} = 250 ml(STP)/min.

Entry	**IL**	**IL [wt.%]**	**Pd/CNF [wt.%]**	**T [K]**	**C_{H_2}[vol.%]**	**$S_{C_2H_4}$[%]**	**R [mol/(g_{Pd}s)]**
1	[bmim][PF_6]	3	1.7	343	10	60	3.2E-03
2	[bmim][PF_6]	3	1.7	343	30	65	7.0E-03
3	[bmim][PF_6]	3	1.7	423	10	78	2.0E-02
4	[bmim][PF_6]	3	1.7	423	30	85	3.7E-02
5	[bmimOH][Tf_2N]	6	2.7	343	10	70	4.7E-03
6	[bmimOH][Tf_2N]	6	2.7	423	10	77	3.4E-02
3*	[bmim][PF_6]	3	1.7	423	10	80	2.5E-02
6*	[bmim][PF_6]	6	2.7	423	10	73	3.0E-02

* in C_2H_4 rich stream (2 vol.% C_2H_2, 40 vol.% C_2H_4, 10 vol.% H_2in Ar; Q_{tot}= 150 ml(STP)min)

The external ionic layers presumably control the access to the nanoparticles and can sterically hinder part of the surface, preventing the formation of active site-ensembles, known to facilitate the oligomerization of acetylene [161]. Most likely, the supramolecular structures created by the IL around the particle promote the surface segregation into small sites, which also enhance the selectivity to ethylene. Furthermore, as the catalyst did not show any deactivation, it was possible to reuse it for several runs even after exposure to air. Indeed, it is known that the interaction of IL with the metal surface enhances the stability of the nanoparticles via electrosteric effect [116, 241].

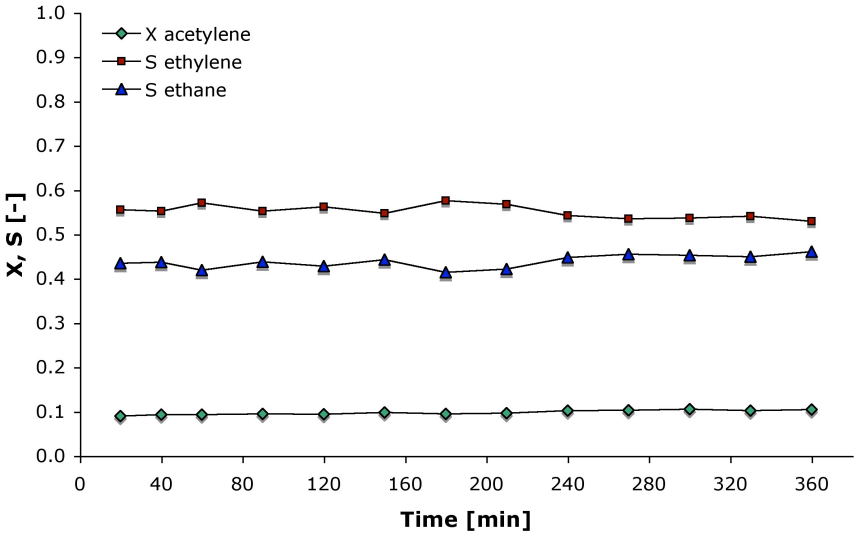

Figure 7.5: Conversion of acetylene, selectivity to ethylene and to ethane as function of time on-stream. Pd nanoparticles in [bmim][PF_6]/CNF/SMF$_{Inconel}$, C_2H_2 : H_2 : Ar = 4: 10: 86, Q_{tot} = 250 ml(STP)/min.

Two different IL, [bmim][PF_6] and [bmimOH][Tf_2N], were employed in the study and Table 7.2 shows the observed activity for the catalysts based on them. The hydrogenation rate is apparently more sensitive to the nature of IL in which nanoparticles are embedded than to the particle size. The activity is slightly higher in [bmimOH][Tf_2N] (entries 5 and 6), because the Pd surface area exposed and active is higher for smaller nanoparticles. The coordinating power of the anions, which form the first layer of the "protective shell" around the nanoparticle, influences the accessibility of reactants to the particle, thus modifying its catalytic activity. The Tf_2N^- anion is known to be less coordinating than $PF_6{}^-$ [242], the nanoparticles surface is more accessible and consequently the catalytic activity increases [118]. Thus the nature of the IL employed influences not only the formation of nanoparticles, but also their catalytic activity.

7.3.2 Mass Transfer Limitations

The presence of an IL layer on the support, in which Pd nanoparticles are embedded, influences the activity of the catalyst compared to the IL-free systems, since the process of hydrogenation can be mass transfer controlled [141, 142, 212]. In order to test the mass transfer limitations, three different catalysts were prepared with increasing amounts of IL (Pd(acac)$_2$/IL ratio constant) and tested at 373 K. As

shown in Figure 7.6, the specific reaction rate decreased with the increasing layer of IL, clearly showing an influence of the mass transfer on the kinetic of the process.

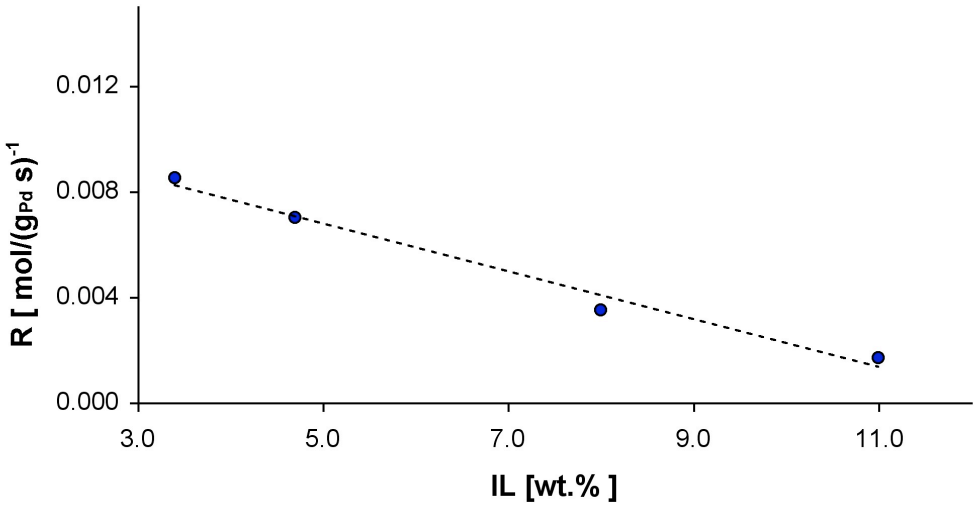

Figure 7.6: Specific reaction rate as a function of IL loading, Pd nanoparticles in [bmim][PF_6]/CNF/SMF$_{Inconel}$, C_2H_2 : H_2 : Ar = 4: 30: 56, Q_{tot} = 250 ml(STP)/min, T = 373 K.

In order to exclude the limitation of the convective mass transport from the bulk gas phase to the IL phase, the total volumetric flow was varied between 50 and 500 ml(STP)/min, consequently reducing the residence time on the catalyst and improving the external mass transfer of the gas reactants to the active phase. No major changes on the specific reaction rate were measured, so the convection term of the mass transfer could be neglected relative to the diffusion term. Since the catalyst particles are embedded in the IL phase the diffusion term governs the internal mass transfer. The diffusion of gas species into the IL phase is linearly related to their solubility. As observed in various studies [143–145], the solubility of hydrogen in [bmim][PF_6] is relatively small compared to hydrocarbons. The Henry's constant at 298 K and 1 atm is 5380 bar [145] compared to 173$\pm$17 bar and 355$\pm$36 bar for ethylene and ethane respectively [143]. Despite the fact that the solubility of hydrogen increases with increasing temperature [144], it is highly probable that the reaction in the herein reported study was limited by the diffusion of hydrogen through the IL film. This inference was also confirmed by the higher activity shown by the [bmimOH][Tf_2N]-based catalyst (see 7.3.1), due to the enhanced accessibility of the reactants to the nanoparticles. Indeed, the solubility of hydrogen has been demonstrated to be higher in IL with the Tf_2N^- anion, regardless of the cation [145, 243]. As the results in Table 7.2 show, we can hypothesize

that the catalytic system herein reported worked in a mixed regime only in part limited by the diffusion of hydrogen into the IL phase.

7.3.3 Catalyst Selectivity towards Ethylene

The nature of the IL employed appeared to influence the selectivity towards ethylene (Table 7.2): at the lower temperature (343 K), the nanoparticles immobilized in [bmimOH][Tf_2N] were more selective than the ones in [bmim][PF_6], but with increasing temperature the selectivity to ethylene reached just the value of 77%. Indeed the solubility of reagents and products depends on the nature of the IL [243]. The difference in solubility between reactants and products in the IL phase (see 7.2.2) can drive the selectivity of the reaction toward the desired products. Consequently, working in a partly limited mass transfer regime at high temperature can induce the system towards better selectivity, as shown in Figure 7.7. Selectivity to ethylene up to 85% could be achieved at 423 K with the nanoparticles in [bmim][PF_6], compared to the 60 % achieved with IL-free supported Pd nanoparticles (see Chapter 6) and can be rationalized from the difference in solubility of reactants and products. With increasing temperatures the hydrocarbon solubility decreases, as confirmed by the herein reported NMR spectroscopy study and by Anthony *et al.* [143], while hydrogen solubility increases [144]. Ethylene can thus leave the IL layer faster, before having the time to be hydrogenated to ethane, but the overall specific reaction rate increases. The inhibition of the consecutive hydrogenation to ethane is a direct consequence of the presence of the IL layer in which the Pd nanoparticles are embedded.

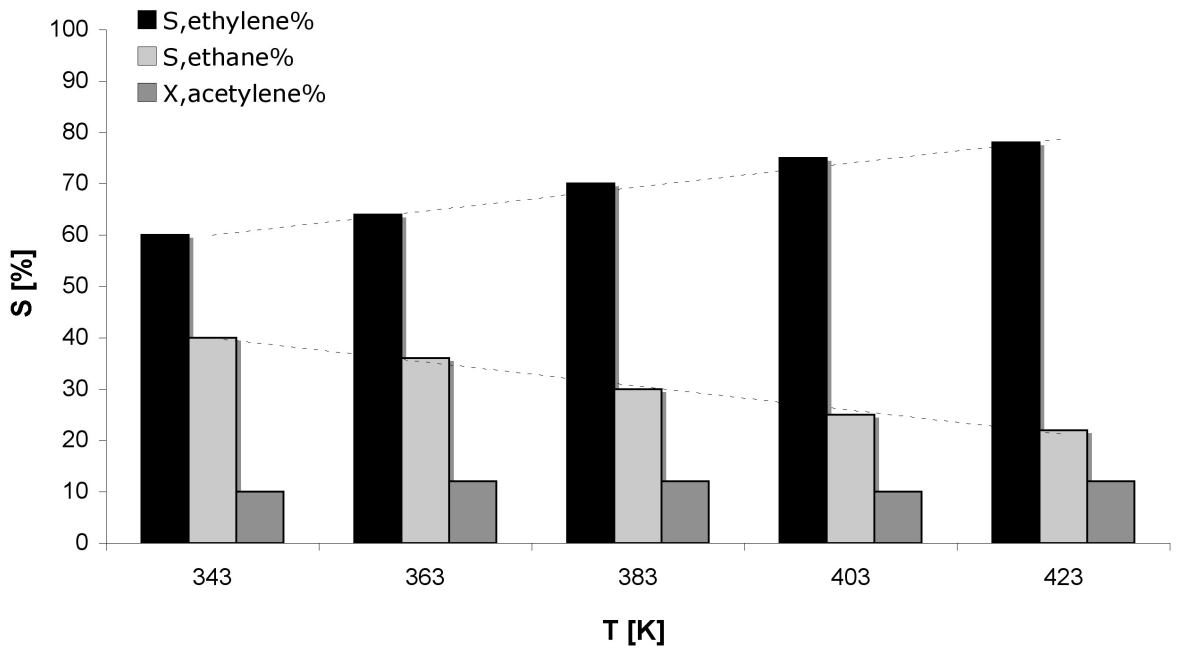

Figure 7.7: Influence of temperature on the selectivity to ethylene and to ethane at constant acetylene conversion ($\sim$10%). Pd nanoparticles in [bmim][PF$_6$]/CNF/SMF$_{Inconel}$, C_2H_2 : H_2 : Ar = 4: 10: 86

To verify this hypothesis the selectivity to ethylene was observed while changing the residence time on the catalyst, thus the acetylene conversion. The selectivity to ethylene did not decreased on increasing conversion, confirming that the consecutive route to ethane was negligible.

7.3.4 Catalytic Performance in Acetylene-Ethylene Mixtures

The major objective for the hydrogenation treatment of industrial ethylene streams is to maximize the conversion of the acetylene impurities without loss of ethylene from the main stream (see 2.5). The catalyst herein developed were therefore tested for the hydrogenation of acetylene in an ethylene-rich feed (2 vol.% of C_2H_2, 40 vol.% of C_2H_4 10 vol.% of H_2 in Ar). Due to the large excess of ethylene in the mixture, small changes of this component in the gas phase were difficult to detect, so the catalytic measures were taken at a slightly higher residence time, in order to have appreciable conversions. The selectivity to ethylene in this case could not be calculated according to Eq. 3.4, because the measures of $C_{C_2H_4-out}$ did not corresponded only to the ethylene produced by the hydrogenation of acetylene. However, the true selectivity to ethylene was much more difficult to estimate, because it was not possible to distinguish between ethane directly converted from acetylene or produced through the ethylene hy-

drogenation. The approximated expressions frequently used in industrial plants do not take into account the direct hydrogenation to ethane [179], but an attempt to evaluate the selectivity from the mass balance of hydrogen is illustrated according to Eq. 7.1.

$$S'_{C_2H_4} = \frac{(C_{H_2-in} - C_{H_2-out}) - 2C_{C_2H_6-out}}{C_{C_2H_2-in} - C_{C_2H_2-out}} \tag{7.1}$$

Nevertheless this is as well an approximated evaluation, because it postulates negligible the amount of ethylene present in the feed which is converted to ethane. The temperature of 423 K was chosen in order to profit of the positive effect of the increasing temperature on the selectivity and in order to accelerate the conversion of acetylene.

The ethylene concentration was always found to be higher at the outlet than at the inlet, so the amount converted from the traces of acetylene was always higher than the losses. The results are summarized in Table 7.2 (entries 3* and 6*) and show that for both catalytic systems the selectivity to ethylene is close to those observed for the ethylene-free feed (entries 3 and 6). The difference was comparable with instrumental error ($\leq$5%) in determining the species concentration. Therefore the supposition made for the evaluation of the selectivity (equation 7.1) was appropriate and the losses of ethylene from the inlet feed could be neglected. Indeed, if part of the ethane measured at the outlet were formed from the hydrogenation of ethylene present in the feed, the selectivity calculated according to Equation 7.1 would have been underestimated. By means of the catalysts reported herein, the ethylene stream could be then easily purified from acetylene traces without compromising the yield of the further polymerization process.

7.4 Conclusions

In this Chapter we reported about the synthesis of SILP Pd nanoparticles on CNF/SMF $_{Inconel}$ and their application for the selective hydrogenation of acetylene. The SILP provided a favorable environment for the formation of metal nanoparticles with small size and narrow size distribution, thanks to the electro-sterical stabilization given by the supramolecular structure of the cation-anion networks. The use of two different IL, one of which OH-functionalized, allowed carrying out the reduction of the metallic precursor with and without the presence of an external reducing agent, partly simplifying the synthesis procedure:

- 10 nm-sized nanoparticles were formed by H_2 reduction of Pd $(acac)_2$ in [bmim][PF_6]

- 5 nm-sized nanoparticles were formed by heating treatment of Pd(acac)$_2$ in [bmimOH][Tf$_2$N]

As IL have extremely low vapor pressure, *in situ* SEM, TEM and *XPS* analysis of the nanoparticles dispersed in IL could be carried out. The loading of SILP on CNF/SMF$_{Inconel}$ could be related with the qualitative SEM observation of the layer's thickness on the support. XPS characterization of the catalysts showed the presence of Pd (II) not reduced in both SILP systems prepared.

The catalytic activity of SILP Pd nanoparticles toward the selective hydrogenation of acetylene was found to be comparable to that of IL-free nanoparticles described in the previous Chapter (between $3{\cdot}10^{-3}$ and $3{\cdot}10^{-2}$mol/(g$_{Pd}$·s)). Although the IL layer didn't block the catalytic surface providing a suitable activity, its presence influenced the accessibility of the reactants to the particle surface, and to certain active sites. As a result no green-oil formation was observed, providing a higher stability of the catalyst compared to the ones reported in Chapter 6. The coordinating power of the anion was supposed responsible for the accessibility to the particles surface, thus the weaker coordinating Tf$_2$N provided higher catalytic activity, since the catalyst surface was more exposed. In the SILP catalytic system the reaction rate was more sensitive to the IL nature than to the particle size.

Under the reaction conditions applied (low H$_2$ pressure) the reaction rate was found mass transfer controlled, where the diffusion of H$_2$ was considered to be the rate determining step. The partial solubility of reactants and products in the SILP was nevertheless found advantageous, because the desired product ethylene could be extracted avoiding the consecutive hydrogenation to ethane. NMR spectroscopy experiments, carried out to measure the gas concentrations in IL at different temperatures, confirmed that ethylene is more soluble than acetylene and that the solubility decreases with increasing temperature. As a result selectivity of 85% toward ethylene could be reached at high temperature (423 K), inhibiting the consecutive route to ethane.

Given the promising properties of the herein reported catalytic system, it was tested for the hydrogenation of acetylene-ethylene mixtures, thus approaching the industrial conditions for cracked hydrocarbon streams (see 2.5). The selectivity to ethane was maintained between 70% and 80%, depending on the IL employed, and the losses of ethylene due to its hydrogenation were confirmed to be negligible.

Chapter 8

Conclusions and Outlook

The aim of the work described in this thesis has been the exploration of the potential of CNF/SMF$_{Inconel}$ as structured catalyst support material, notably for the design of novel catalytic systems for hydrogenations. This composite material should show superior properties compared to the standard granulated material used in the fixed-bed reactor technology [4]. At this purpose the development of the synthetic route of CNF on SMF$_{Inconel}$ was carried out varying C-precursor, temperature and synthesis time for the CVD of CNF, as well as the optional functionalization of CNF by oxidative treatment. Highly graphitized CNF were obtained with ethylene as C-precursor and at relatively high temperature (973 K). The absence of defects in the graphitic structure of the CNF is a convenient property when depositing metal nanoparticles for the strong interaction between CNF and metal, which helps to reduce the mobility of the metal and prevent the sintering. Nevertheless, the permeability of the composite was optimized, thus minimizing the pressure drop in the fixed-bed reactor, when using ethane, instead of ethylene, as C-precursor. When the catalytic application required the activation of the CNF surface, we discovered that the treatment with plasma-generated O_3 gave a higher yield of carboxylic groups compared to the treatment with boiling H_2O_2. The acidity of the material was thus enhanced, but at temperature higher than 423 K this difference disappeared because the carboxylic groups were found as the most thermally unstable, evolving CO_2 at temperatures lower than 700 K.

In the quest for a more efficient and well-defined catalyst for the selective hydrogenation of acetylene, Pd nanoparticles with monodispersed size, synthesized by reverse ME technique, were supported on CNF/SMF$_{Inconel}$ and on functionalized CNF/SMF$_{Inconel}$. Their catalytic performance for the chosen reaction was found dependent on the particle size and on the support acidity. The activity increased with the particle size up to 11 nm, while the deactivation of the catalyst followed the reverse trend.

Pd nanoparticles supported on "acidic" supports were less active but slightly more selective to ethylene, moreover their deactivation was less pronounced due to the lower quantity of green-oil formed on the surface. The selectivity of the herein described catalyst was compromised in the long-term by the presence of oligomers.

During the course of the thesis work, the CNF/SMF$_{Inconel}$ were employed for the development of a novel structured SILP catalytic system, which allowed the "heterogenization" of a TMC catalyst dissolved in IL and to test it in a fixed-bed reactor. Through the study and the optimization of the catalytic system, we proved that the performance in the gas-phase hydrogenation of 1,3-cyclohexadiene to cyclohexene (test reaction) was enhanced compared to systems based on different structured supports. By tailoring the thickness of the IL layer on the mesoporous surface of the support and thanks to the chemical inertness of the CNF layer, we improved the efficiency of the catalyst, reaching TOF up to 250 h^{-1} and selectivity > 96%. Indeed, mass transfer limitations due to the diffusion of reactants in the IL layer were reduced and no sequestration of the active phase by interaction with the support was allowed.

Based on the successful results of the SSILP catalytic system for the hydrogenation of 1,3-cyclohexadiene, the synthesis of monodispersed Pd nanoparticles was then carried out in SILP on CNF/SMF$_{Inconel}$. The formation of nanoparticles could be achieved in the absence of any reducing agent, by employing an IL containing an OH functionality which is supposed to reduce the Pd-ionic precursor. The synthetic route was then greatly simplified. The presence of the IL stabilized the nanoparticles and its nature determined their size. The catalytic activity was comparable with the one of the IL-free nanoparticles, but the presence of the IL layer around the particle allowed to modify the selectivity of the process. No green-oil formation was observed and we succeeded in developing a highly stable catalyst for the hydrogenation of acetylene, reusable after multiple runs. The selectivity to ethylene was also improved, reaching values up to 85% at 423 K, thanks to the lower solubility of ethylene in IL. The over-hydrogenation of the produced ethylene to ethane was inhibited because ethylene tended to escape from the IL layer before having the time to be hydrogenated. Testing this catalyst in a rich-ethylene stream allowed us to approach the industrial conditions and prove that the stream could be purified from acetylene residuals, without losses of ethylene.

Summarizing, the results described in this thesis have shown the potential of CNF/SMF$_{Inconel}$ as catalyst support for the novel application of SSILP catalysis, both with homogeneous TMC and metal nanoparticles as active species. However, an optimization of the nanoparticle synthesis in IL would be desirable, in order to have a better control on the size of the nanoparticles. Future research in this promising area

could amongst others be devoted to *in-situ* observations of the adsorbed species on both Pd and SILP-Pd nanoparticles, to further corroborate the hypothesis on the reaction mechanism. From the perspective of the use of SILP catalyst on CNF/SMF$_{Inconel}$ in liquid phase reactions, the functionalization of IL or CNF could be envisaged in order to enhance the stability of the IL layer on the CNF surface and thus preventing the leaching of active species in the substrate/product phase.

Bibliography

[1] *Fundamentals of Industrial Catalytic Processes (2nd edition)* (Wiley-Interscience, 2006).

[2] Auer, E., Freund, A., Pietsch, J. & Tacke, T. Carbons as supports for industrial precious metal catalysts. *Applied Catalysis A-General* **173**, 259–271 (1998).

[3] Serp, P., Corrias, M. & Kalck, P. Carbon nanotubes and nanofibers in catalysis. *Applied Catalysis A-General* **253**, 337–358 (2003).

[4] Tribolet, P. *Nanofibres de carbone sur filtre métallique comme support catalytique structuré*. Ph.D. thesis, EPFL (2006).

[5] Riisager, A., Fehrmann, R., Haumann, M. & Wasserscheid, P. Supported ionic liquid phase (silp) catalysis: An innovative concept for homogeneous catalysis in continuous fixed-bed reactors. *European Journal of Inorganic Chemistry* 695–706 (2006).

[6] Astruc, D. (ed.) *Nanoparticles and Catalysis* (Wiley-VCH, 2008).

[7] Ott, L. S. & Finke, R. G. Transition-metal nanocluster stabilization for catalysis: A critical review of ranking methods and putative stabilizers. *Coordination Chemistry Reviews* **251**, 1075–1100 (2007).

[8] Matatov-Meytal, Y. & Sheintuch, M. Catalytic fibers and cloths. *Applied Catalysis A-General* **231**, 1–16 (2002).

[9] Ahlstrom-Silversand, A. F. & Odenbrand, C. U. I. Modelling catalytic combustion of carbon monoxide and hydrocarbons over catalytically active wire meshes. *Chemical Engineering Journal* **73**, 205–216 (1999).

[10] Satterfield, C. *Heterogeneous Catalysis in Industrial practice* (McGraw-Hill, New York, 1991).

[11] Vorob'eva, M. P., Greish, A. A., Ivanov, A. V. & Kustov, L. M. Preparation of catalyst carriers on the basis of alumina supported on metallic gauzes. *Applied Catalysis A-General* **199**, 257–261 (2000).

[12] Louis, B., Reuse, P., Kiwi-Minsker, L. & Renken, A. Synthesis of zsm-5 coatings on stainless steel grids and their catalytic performance for partial oxidation of benzene by n2o. *Applied Catalysis A-General* **210**, 103–109 (2001).

[13] Louis, B. *et al.* Synthesis and characterization of mcm-41 coatings on stainless steel grids. *Catalysis Communications* **3**, 159–163 (2002).

[14] Yuranov, I., Renken, A. & Kiwi-Minsker, L. Zeolite/sintered metal fibers composites as effective structured catalysts. *Applied Catalysis A-General* **281**, 55–60 (2005).

[15] Tribolet, P. & Kiwi-Minsker, L. Carbon nanofibers grown on metallic filters as novel catalytic materials. *Catalysis Today* **102**, 15–22 (2005).

[16] Davis, W. R., Slawson, R. J. & Rigby, G. R. An unusual form of carbon. *Nature* **171**, 756–756 (1953).

[17] Baker, R. T. K. Catalytic growth of carbon filaments. *Carbon* **27**, 315–323 (1989).

[18] Kroto, H. W., Heath, J. R., Obrien, S. C., Curl, R. F. & Smalley, R. E. C-60- buckminsterfullerene. *Nature* **318**, 162–163 (1985).

[19] Iijima, S. Helical microtubules of graphitic carbon. *Nature* **354**, 56–58 (1991).

[20] Tibbetts, G. G. Why are carbon filaments tubular. *Journal of Crystal Growth* **66**, 632–638 (1984).

[21] Kratschmer, W., Lamb, L. D., Fostiropoulos, K. & Huffman, D. R. Solid c-60 - a new form of carbon. *Nature* **347**, 354–358 (1990).

[22] Bethune, D. S. *et al.* Cobalt-catalyzed growth of carbon nanotubes with single-atomic-layerwalls. *Nature* **363**, 605–607 (1993).

[23] Iijima, S. & Ichihashi, T. Single-shell carbon nanotubes of 1-nm diameter. *Nature* **364**, 737–737 (1993).

[24] Thess, A. *et al.* Crystalline ropes of metallic carbon nanotubes. *Science* **273**, 483–487 (1996).

[25] O'Connell, M. *Carbon nanotubes: properties and applications* (Taylor and Francis, New York, 2006).

[26] Endo, M. *et al.* The production and structure of pyrolytic carbon nanotubes (pcnts). *Journal of Physics and Chemistry of Solids* **54**, 1841–1848 (1993).

[27] De Jong, K. P. & Geus, J. W. Carbon nanofibers: Catalytic synthesis and applications. *Catalysis Reviews-Science And Engineering* **42**, 481–510 (2000).

[28] Maruyama, S., Kojima, R., Miyauchi, Y., Chiashi, S. & Kohno, M. Low-temperature synthesis of high-purity single-walled carbon nanotubes from alcohol. *Chemical Physics Letters* **360**, 229–234 (2002).

[29] Nolan, P. E., Lynch, D. C. & Cutler, A. H. Catalytic disproportionation of co in the absence of hydrogen - encapsulating shell carbon formation. *Carbon* **32**, 477–483 (1994).

[30] Park, C. & Baker, R. T. K. Catalytic behavior of graphite nanofiber supported nickel particles. 2. the influence of the nanofiber structure. *Journal of Physical Chemistry B* **102**, 5168–5177 (1998).

[31] Park, C. & Keane, M. A. Catalyst support effects in the growth of structured carbon from the decomposition of ethylene over nickel. *Journal of Catalysis* **221**, 386–399 (2004).

[32] Anderson, P. E. & Rodriguez, N. M. Influence of the support on the structural characteristics of carbon nanofibers produced from the metal-catalyzed decomposition of ethylene. *Chemistry of Materials* **12**, 823–830 (2000).

[33] Corrias, M. *et al.* Carbon nanotubes produced by fluidized bed catalytic cvd: first approach of the process. *Chemical Engineering Science* **58**, 4475–4482 (2003).

[34] Meyyappan, M., Delzeit, L., Cassell, A. & Hash, D. Carbon nanotube growth by pecvd: a review. *Plasma Sources Science and Technology* **12**, 205–216 (2003).

[35] Zhou, D., Anoshkina, E. V., Chow, L. & Chai, G. Y. Synthesis of carbon nanotubes by electrochemical deposition at room temperature. *Carbon* **44**, 1013–1016 (2006).

[36] Baker, R. T. K., Barber, M. A., Waite, R. J., Harris, P. S. & Feates, F. S. Nucleation and growth of carbon deposits from nickel catalyzed decomposition of acetylene. *Journal of Catalysis* **26**, 51 (1972).

[37] Baker, R. T. K., Harris, P. S., Thomas, R. B. & Waite, R. J. Formation of filamentous carbon from iron, cobalt and chromium catalyzed decomposition of acetylene. *Journal of Catalysis* **30**, 86–95 (1973).

[38] Rodriguez, N. M. A review of catalytically grown carbon nanofibers. *Journal of Material Research* **8**, 3233–3250 (1993).

[39] Sacco, A., Thacker, P., Chang, T. N. & Chiang, A. T. S. The inintiation and growth of filamentous carbon from alpha-iron in h2, ch4, h2o, co2, and co gas-mixtures. *Journal of Catalysis* **85**, 224–236 (1984).

[40] Alsturp, I. A new model explaining carbon-filament growth on nickel, iron, and ni-cu alloy catalysts. *Journal of Catalysis* **109**, 241–251 (1988).

[41] Baird, T., Fryer, J. R. & Grant, B. Carbon formation on iron and nickel foils by hydrocarbon pyrolysis-reactions at 700 degrees c °. *CARBON* **12**, 591–602 (1974).

[42] Hofmann, S., Ducati, C., Robertson, J. & Kleinsorge, B. Low-temperature growth of carbon nanotubes by plasma-enhanced chemical vapor deposition. *Applied Physics Letters* **83**, 135–137 (2003).

[43] Hofmann, S., Csanyi, G., Ferrari, A. C., Payne, M. C. & Robertson, J. Surface diffusion: The low activation energy path for nanotube growth. *Physical Review Letters* **95** (2005).

[44] Rodriguez-Manzo, J. A. *et al.* In situ nucleation of carbon nanotubes by the injection of carbon atoms into metal particles. *Nature Nanotechnology* **2**, 307–311 (2007).

[45] Wei, Y. Y., Eres, G., Merkulov, V. I. & Lowndes, D. H. Effect of catalyst film thickness on carbon nanotube growth by selective area chemical vapor deposition. *Applied Physiscs Letters* **78**, 1394–1396 (2001).

[46] Helveg, S. *et al.* Atomic-scale imaging of carbon nanofibre growth. *Nature* **427**, 426–429 (2004).

[47] Jablonski, G. A., Geurts, F. W., Sacco, A. & Biederman, R. R. Carbon deposition over fe, ni, and co foils from co-h2-ch4-co2-h2o, co-co2, and co-h2-h2o gas mixtures. 1. morphology. *Carbon* **30**, 87–98 (1992).

[48] Jarrah, N. A., van Ommen, J. G. & Lefferts, L. Growing a carbon nano-fiber layer on a monolith support; effect of nickel loading and growth conditions. *Journal of Materials Chemistry* **14**, 1590–1597 (2004).

[49] Jarrah, N. A., Li, F. H., van Ommen, J. G. & Lefferts, L. Immobilization of a layer of carbon nanofibres (cnfs) on ni foam: A new structured catalyst support. *Journal of Materials Chemistry* **15**, 1946–1953 (2005).

[50] Vieira, R., Ledoux, M. J. & Pham-Huu, C. Synthesis and characterisation of carbon nanofibres with macroscopic shaping formed by catalytic decomposition of c2h6/h-2 over nickel catalyst. *Applied Catalysis a-General* **274**, 1–8 (2004).

[51] van der Lee, M. K., van Dillen, A. J., Bitter, J. H. & de Jong, K. P. Deposition precipitation for the preparation of carbon nanofiber supported nickel catalysts. *Journal of the American Chemical Society* **127**, 13573–13582 (2005).

[52] Pham-Huu, C. *et al.* About the octopus-like growth mechanism of carbon nanofibers over graphite supported nickel catalyst. *Journal of Catalysis* **240**, 194–202 (2006).

[53] Ermakova, M. A., Ermakov, D. Y., Chuvilin, A. L. & Kuvshinov, G. G. Decomposition of methane over iron catalysts at the range of moderate temperatures: The influence of structure of the catalytic systems and the reaction conditions on the yield of carbon and morphology of carbon filaments. *Journal of Catalysis* **201**, 183–197 (2001).

[54] Cassell, A. M., Raymakers, J. A., Kong, J. & Dai, H. J. Large scale cvd synthesis of single-walled carbon nanotubes. *Journal of Physical Chemistry B* **103**, 6484–6492 (1999).

[55] Lyu, S. C. *et al.* Large-scale synthesis of high-quality single-walled carbon nanotubes by catalytic decomposition of ethylene. *Journal of Physical Chemistry B* **108**, 1613–1616 (2004).

[56] Vander Wal, R. L., Ticich, T. M. & Curtis, V. E. Substrate-support interactions in metal-catalyzed carbon nanofiber growth. *Carbon* **39**, 2277–2289 (2001).

[57] Nikolaev, P. *et al.* Gas-phase catalytic growth of single-walled carbon nanotubes from carbon monoxide. *Chemical Physics Letters* **313**, 91–97 (1999).

[58] Chatterjee, A. & Deopura, B. L. Carbon nanotubes and nanofibre: An overview. *Fibers and Polymers* **3**, 134–139 (2002).

[59] Mordkovich, V. Z. Carbon nanofibers: A new ultrahigh-strength material for chemical technology. *Theoretical Foundations of Chemical Engineering* **37**, 429–438 (2003).

[60] Tan, E. P. S. & Lim, C. T. Mechanical characterization of nanofibers - a review. *Composite Science and Technology* **66**, 1102–1111 (2006).

[61] Kuriger, R. J., Alam, M. K., Anderson, D. P. & Jacobsen, R. L. Processing and characterization of aligned vapor grown carbon fiber reinforced polypropylene. *Composites Part A- Applied Science and Manufacturing* **33**, 53–62 (2002).

[62] Merino, C. *et al.* Carbon nanofibres and activated carbon nanofibres as electrodes in supercapacitors. *Carbon* **43**, 551–557 (2005).

[63] Bessel, C. A., Laubernds, K., Rodriguez, N. M. & Baker, R. T. K. Graphite nanofibers as an electrode for fuel cell applications. *Journal of Physical Chemistry B* **105**, 1115–1118 (2001).

[64] Baker, R. T. K. Graphite nanofiber catalyst for use in fuel cell electrodes (2002).

[65] Dillon, A. C. *et al.* Storage of hydrogen in single-walled carbon nanotubes. *Nature* **386**, 377–379 (1997).

[66] Chambers, A., Park, C., Baker, R. T. K. & Rodriguez, N. M. Hydrogen storage in graphite nanofibers. *Journal of Physical Chemistry B* **102**, 4253–4256 (1998).

[67] van den Berg, A. W. C. & Arean, C. O. Materials for hydrogen storage: current research trends and perspectives. *Chemical Communications* 668–681 (2008).

[68] Kowalczyk, P., Holyst, R., Terrones, M. & Terrones, H. Hydrogen storage in nanoporous carbon materials: myth and facts. *Physical Chemistry Chemical Physics* **9**, 1786–1792 (2007).

[69] Rodriguez-Reinoso, F. The role of carbon materials in heterogeneous catalysis. *Carbon* **36**, 159–175 (1998).

[70] Ledoux, M. J., Vieira, R., Pham-Huu, C. & Keller, N. New catalytic phenomena on nanostructured (fibers and tubes) catalysts. *Journal of Catalysis* **216**, 333–342 (2003).

[71] Chinthaginjala, J. K., Seshan, K. & Lefferts, L. Preparation and application of carbon-nanofiber based microstructured materials as catalyst supports. *Industrial and Engineering Chemistry Research* **46**, 3968–3978 (2007).

[72] Rodriguez, N. M., Kim, M. S. & Baker, R. T. K. Carbon nanofibers - a unique catalyst support medium. *Journal Of Physical Chemistry* **98**, 13108–13111 (1994).

[73] Chambers, A., Nemes, T., Rodriguez, N. M. & Baker, R. T. K. Catalytic behavior of graphite nanofiber supported nickel particles. 1. comparison with other support media. *Journal of Physical Chemistry B* **102**, 2251–2258 (1998).

[74] Baker, R. T. K. *et al.* Platinum/graphite nanofiber catalysts of various structure: Characterization and catalytic properties. *Journal of Physical Chemistry B* **108**, 14348–14355 (2004).

[75] Salman, F., Park, C. & Baker, R. T. K. Hydrogenation of crotonaldehyde over graphite nanofiber supported nickel. *Catalysis Today* **53**, 385–394 (1999).

[76] Toebes, M. L., Bitter, J. H., van Dillen, A. J. & de Jong, K. P. Impact of the structure and reactivity of nickel particles on the catalytic growth of carbon nanofibers. *Catalysis Today* **76**, 33–42 (2002).

[77] Hoogenraad, M. S. *Growth and Utilization of Carbon Fibrils*. Ph.D. thesis, Universiteit Utrecht (1995).

[78] Pham-Huu, C. *et al.* Carbon nanofiber supported palladium catalyst for liquid-phase reactions - an active and selective catalyst for hydrogenation of cinnamaldehyde into hydrocinnamaldehyde. *Journal of Molecular Catalysis a-Chemical* **170**, 155–163 (2001).

[79] Jarrah, N. A., van Ommen, J. G. & Lefferts, L. Mechanistic aspects of the formation of carbon-nanofibers on the surface of ni foam: A new microstructured catalyst support. *Journal of Catalysis* **239**, 460–469 (2006).

[80] Park, C., Rodriguez, N. M. & Baker, R. T. K. The use of carbon nanofibers as a novel catalyst support for hydrogenation reactions. *Abstracts of Papers of the American Chemical Society* **211**, 12 (1996).

[81] Chesnokov, V. V., Prosvirin, I. P., Zaitseva, N. A., Zaikovskii, V. I. & Molchanov, V. V. Effect of the structure of carbon nanofibers on the state of an active component and on the catalytic properties of pd/c catalysts in the selective hydrogenation of 1,3-butadiene. *Kinetics and Catalysis* **43**, 838–846 (2002).

[82] Keane, M. A. & Park, C. Carbon nanofibers as novel metal supports: Phenol hydrogenation over palladium. *Abstracts of Papers of the American Chemical Society* **226**, U403–U403 (2003).

[83] Toebes, M. L. *et al.* Support effects in the hydrogenation of cinnamaldehyde over carbon nanofiber-supported platinum catalysts: characterization and catalysis. *Journal of Catalysis* **226**, 215–225 (2004).

[84] Tribolet, P. & Kiwi-Minsker, L. Palladium on carbon nanofibers grown on metallic filters as novel structured catalyst. *Catalysis Today* **105**, 337–343 (2005).

[85] Ros, T. G., van Dillen, A. J., Geus, J. W. & Koningsberger, D. C. Surface oxidation of carbon nanofibres. *Chemistry-a European Journal* **8**, 1151–1162 (2002).

[86] Toebes, M. L., van Heeswijk, E. M. P., Bitter, J. H., van Dillen, A. J. & de Jong, K. P. The influence of oxidation on the texture and the number of oxygen-containing surface groups of carbon nanofibers. *Carbon* **42**, 307–315 (2004).

[87] Ago, H. *et al.* Work functions and surface functional groups of multiwall carbon nanotubes. *J. Phys. Chem. B* **103**, 8116–8121 (1999).

[88] Mawhinney, D. B. *et al.* Surface defect site density on single walled carbon nanotubes by titration. *Chemical Physics Letters* **324**, 213–216 (2000).

[89] Boehm, H. P., Heck, W., Sappok, R. & Diehl, E. Surface oxides of carbon. *Angewandte Chemie-International Edition* **3**, 669 (1964).

[90] Boehm, H. P. Surface oxides on carbon and their analysis: a critical assessment. *Carbon* **40**, 145–149 (2002).

[91] Pradoburguete, C., Linaressolano, A., Rodriguezreinoso, F. & Delecea, C. S. The effect of oxygen-surface groups of the support on platinum dispersion in pt/carbon catalysts. *Journal of Catalysis* **115**, 98–106 (1989).

[92] Toebes, M. L., Prinsloo, F. F., Bitter, J. H., van Dillen, A. J. & de Jong, K. P. Influence of oxygen-containing surface groups on the activity and selectivity of carbon nanofiber-supported ruthenium catalysts in the hydrogenation of cinnamaldehyde. *Journal of Catalysis* **214**, 78–87 (2003).

[93] Zhang, Y. H. *et al.* Metal particle size and structure of the metal-support interface of carbon-supported platinum catalysts as determined with exafs spectroscopy. *Journal of Physical Chemistry B* **108**, 18509–18519 (2004).

[94] Xia, W., Wang, Y., Bergstrasser, R., Kundu, S. & Muhler, M. Surface characterization of oxygen-functionalized multi-walled carbon nanotubes by high-resolution x-ray photoelectron spectroscopy and temperature-programmed desorption. *APPLIED SURFACE SCIENCE* **254**, 247–250 (2007).

[95] Zhou, J. H. *et al.* Characterization of surface oxygen complexes on carbon nanofibers by tpd, xps and ft-ir. *Carbon* **45**, 785–796 (2007).

[96] Vieira, R., Bernhardt, P., Ledoux, M. J. & Pham-Huu, C. Performance comparison of ir/cnf and ir/al2o3 catalysts in a 2 n hydrazine microthruster. *Catalysis Letters* **99**, 177–180 (2005).

[97] Vieira, R., Bernhardt, P., Ledoux, M. J. & Cuong, P. H. Carbon nanofiber composite as a catalytic hydrazine decomposition support for satellite propulsion. *Japanese Journal of Applied Physics Part 1-Regular Papers Short Notes and Review Papers* **44**, 4282–4284 (2005).

[98] Gangeri, A. *et al.* Electrocatalytic performances of nanostructured platinum-carbon materials. *Catalysis Today* **102**, 50–57 (2005).

[99] Jarrah, N., van Ommen, J. G. & Lefferts, L. Development of monolith with a carbon-nanofiber-washcoat as a structured catalyst support in liquid phase. *Catalysis Today* **79**, 29–33 (2003).

[100] de Lathouder, K. M., Flo, T. M., Kapteijn, E. & Moulijn, J. A. A novel structured bioreactor: Development of a monolithic stirrer reactor with immobilized lipase. *Catalysis Today* **105**, 443–447 (2005).

[101] Walden, P. *Bull.Acad.Sci.St. Petesburg* 405–422 (1914).

[102] Hagiwara, R. & Ito, Y. Room temperature ionic liquids of alkylimidazolium cations and fluoroanions. *Journal of Fluorine Chemistry* **105**, 221–227 (2000).

[103] Stark, A. & Seddon, K. R. *Kirk-Othmer Encyclopaedia of Chemical Technology*, vol. 26 (John Wiley and Sons, Inc., Hoboken, New Jersey, 1998).

[104] Welton, T. Ionic liquids in catalysis. *Coordination Chemistry Reviews* **248**, 2459–2477 (2004).

[105] Geldbach, T. J. & Dyson, P. J. *Metal Catalyzed Reactions in Ionic Liquids* (Springer, 2005).

[106] Parvulescu, V. I. & Hardacre, C. Catalysis in ionic liquids. *Chemical Reviews* **107**, 2615–2665 (2007).

[107] Zhao, D. B., Liao, Y. C. & Zhang, Z. D. Toxicity of ionic liquids. *Clean-Soil and Water* **35**, 42–48 (2007).

[108] Freemantle, M. Basf's smart ionic liquid. *Chemical and Engineering News* **81**, 9 (2003).

[109] Aiken, J. D. & Finke, R. G. A review of modern transition-metal nanoclusters: their synthesis, characterization, and applications in catalysis. *Journal of Molecular Catalysis A-Chemical* **145**, 1–44 (1999).

[110] Shchukin, D. G. & Sukhorukov, G. B. Nanoparticle synthesis in engineered organic nanoscale reactors. *Advanced Materials* **16**, 671–682 (2004).

[111] Bronstein, L. M., Sidorov, S. N. & Valetsky, P. M. Nanostructured polymer systems as nanoreactors for nanoparticle formation. *USPEKHI KHIMII* **73**, 542–558 (2004).

[112] Dupont, J. & Suarez, P. A. Z. Physico-chemical processes in imidazolium ionic liquids. *Physical Chemistry Chemical Physics* **8**, 2441–2452 (2006).

[113] Dupont, J., Suarez, P. A. Z., De Souza, R. F., Burrow, R. A. & Kintzinger, J. P. C-h-pi interactions in 1-n-butyl-3-methylimidazolium tetraphenylborate molten salt: Solid and solution structures. *Chemistry-A European Journal* **6**, 2377–2381 (2000).

[114] Dupont, J., Fonseca, G. S., Umpierre, A. P., Fichtner, P. F. P. & Teixeira, S. R. Transition-metal nanoparticles in imidazolium ionic liquids: Recycable catalysts for biphasic hydrogenation reactions. *Journal of the American Chemical Society* **124**, 4228–4229 (2002).

[115] Migowski, P. & Dupont, J. Catalytic applications of metal nanoparticles in imidazolium ionic liquids. *Chemistry-a European Journal* **13**, 32–39 (2007).

[116] Machado, G. *et al.* Structural aspects of transition-metal nanoparticles in imidazolium ionic liquids. *International Journal of Nanotechnology* **4**, 541–563 (2007).

[117] Redel, E., Thomann, R. & Janiak, C. First correlation of nanoparticle size-dependent formation with the ionic liquid anion molecular volume. *Inorganic Chemistry* **47**, 14–16 (2008).

[118] Scheeren, C. W. *et al.* Synthesis and characterization of pt(0) nanoparticles in imidazolium ionic liquids. *Journal of Physical Chemistry B* **110**, 13011–13020 (2006).

[119] Zhao, D. B., Fei, Z. F., Scopelliti, R. & Dyson, P. J. Synthesis and characterization of ionic liquids incorporating the nitrile functionality. *Inorganic Chemistry* **43**, 2197–2205 (2004).

[120] Zhao, D. B., Fei, Z. F., Geldbach, T. J., Scopelliti, R. & Dyson, P. J. Nitrile-functionalized pyridinium ionic liquids: Synthesis, characterization, and their application in carbon - carbon coupling reactions. *Journal of the American Chemical Society* **126**, 15876–15882 (2004).

[121] Benazzi, E., Olivier, H., Chauvin, Y., Joly, J. F. & Hirschauer, A. Supported liquid organochloroaluminates: A novel class of solid acid catalysts for butene alkylation with isobutane. *Abstracts of Papers of the American Chemical Society* **212**, 45 (1996).

[122] Arhancet, J. P., Davis, M. E., Merola, J. S. & Hanson, B. E. Hydroformylation by supported aqueous-phase catalysis - a new class of heterogeneous catalysts. *Nature* **339**, 454–455 (1989).

[123] Cornils, B. *Aqueous-Phase Organometallic Catalysis: Concepts and Applications* (Wiley-VCH, Weinheim, 2004).

[124] Mehnert, C. P., Cook, R. A., Dispenziere, N. C. & Afeworki, M. Supported ionic liquid catalysis - a new concept for homogeneous hydroformylation catalysis. *Journal of the American Chemical Society* **124**, 12932–12933 (2002).

[125] Valkenberg, M. H., deCastro, C. & Holderich, W. F. Friedel-crafts acylation of aromatics catalysed by supported ionic liquids. *Applied Catalysis a-General* **215**, 185–190 (2001).

[126] Wolfson, A., Vankelecom, I. F. J. & Jacobs, P. A. Co-immobilization of transition-metal complexes and ionic liquids in a polymeric support for liquid-phase hydrogenations. *Tetrahedron Letters* **44**, 1195–1198 (2003).

[127] Carlin, R. T. & Fuller, J. Ionic liquid-polymer gel catalytic membrane. *Chemical Communications* 1345–1346 (1997).

[128] Riisager, A., Fehrmann, R., Haumann, M. & Wasserscheid, P. *Eur. J. Inorg. Chem.* 695 (2006).

[129] Abello, S. *et al.* Supported choline hydroxide (ionic liquid) as heterogeneous catalyst for aldol condensation reactions. *Chemical Communications* 1096–1097 (2004).

[130] Mehnert, C. P., Mozeleski, E. J. & Cook, R. A. Supported ionic liquid catalysis investigated for hydrogenation reactions. *Chemical Communications* 3010–3011 (2002).

[131] Mikkola, J. P., Virtanen, P., Karhu, H., Salmi, T. & Murzin, D. Y. Supported ionic liquids catalysts for fine chemicals: citral hydrogenation. *Green Chemistry* **8**, 197–205 (2006).

[132] Muller, T. E. New catalysts for hydroamination reactions - transition metal complexes in supported ionic liquids. *Abstracts of Papers of the American Chemical Society* **226**, U621–U621 (2003). Part 1.

[133] Riisager, A., Wasserscheid, P., van Hal, R. & Fehrmann, R. Continuous fixed-bed gas-phase hydroformylation using supported ionic liquid-phase (silp) rh catalysts. *Journal of Catalysis* **219**, 452–455 (2003).

[134] Huang, J. *et al.* Pd nanoparticles immobilized on molecular sieves by ionic liquids: Heterogeneous catalysts for solvent-free hydrogenation. *Angewandte Chemie-International Edition* **43**, 1397–1399 (2004).

[135] Kume, Y., Qiao, K., Tomida, D. & Yokoyama, C. Selective hydrogenation of cinnamaldehyde catalyzed by palladium nanoparticles immobilized on ionic liquids modified-silica gel. *Catalysis Communications* **9**, 369–375 (2008).

[136] Hagiwara, H., Sugawara, Y., Isobe, K., Hoshi, T. & Suzuki, T. Immobilization of pd(oac)(2) in ionic liquid on silica: Application to sustainable mizoroki-heck reaction. *Organic Letters* **6**, 2325–2328 (2004).

[137] Breitenlechner, S., Fleck, M., Muller, T. E. & Suppan, A. Solid catalysts on the basis of supported ionic liquids and their use in hydroamination reactions. *Journal of Molecular Catalysis A-Chemical* **214**, 175–179 (2004).

[138] Riisager, A., Eriksen, K. M., Wasserscheid, P. & Fehrmann, R. Propene and l-octene hydroformylation with silica-supported, ionic liquid-phase (silp) rh-phosphine catalysts in continuous fixed-bed mode. *Catalysis Letters* **90**, 149–153 (2003).

[139] Riisager, A. *et al.* Very stable and highly regioselective supported ionic-liquid-phase (silp) catalysis: Continuous flow fixed-bed hydroformylation of propene. *Angewandte Chemie-International Edition* **44**, 815–819 (2005).

[140] Flumerfelt, R. W. & Glover, C. J. *Ullmann's Encyclopedia of Industrial Chemistry* (Wiley-VCH, 2002).

[141] Hardacre, C., Mullan, E. A., Rooney, D. W., Thompson, J. M. & Yablonsky, G. S. Comparison of mass transfer effects in the heterogeneously catalysed hydrogenation of phenyl acetylene in heptane and an ionic liquid. *Chemical Engineering Science* **61**, 6995–7006 (2006).

[142] Mikkola, J. P., Warna, J., Virtanen, P. & Salmi, T. Effect of internal diffusion in supported ionic liquid catalysts: Interaction with kinetics. *Industrial and Engineering Chemistry Research* **46**, 3932–3940 (2007).

[143] Anthony, J. L., Maginn, E. J. & Brennecke, J. F. Solubilities and thermodynamic properties of gases in the ionic liquid 1-n-butyl-3-methylimidazolium hexafluorophosphate. *Journal of Physical Chemistry B* **106**, 7315–7320 (2002).

[144] Kumelan, J., Kamps, A. P. S., Tuma, D. & Maurer, G. Solubility of h-2 in the ionic liquid [bmim][pf6]. *Journal of Chemical and Engineering Data* **51**, 11–14 (2006).

[145] Dyson, P. J., Laurenczy, G., Ohlin, C. A., Vallance, J. & Welton, T. Determination of hydrogen concentration in ionic liquids and the effect (or lack of) on rates of hydrogenation. *Chemical Communications* 2418–2419 (2003).

[146] Lam, W. & Lloyd, L. *The Oil and Gas Journal* **27**, 66 (1972). Times Cited: 81.

[147] Derrien, M. *Catalytic Hydrogenation*, vol. 27 (Elsevier, Amsterdam, 1986).

[148] Bond, G. C. & Sheridam, J. Studies in heterogeneous catalysis .1. the hydrogenation of mixtures of hydrocarbon. *Transactions of the Faraday Society* **48**, 664–668 (1952).

[149] Bond, G. C., Dowden, D. A. & Mackenzie, N. The selective hydrogenation of acetylene. *Transactions of the Faraday Society* **54**, 1537–1546 (1958). Times Cited: 81.

[150] Sheridan, J. The metal-catalyzed reaction between acetylene and hydrogen. 2. further experiments with nickel catalysts. *Journal of the Chemical Society* 133–142 (1945).

[151] Ng, L. K., Eng, C. N. & Zack, R. S. Ethylene from ngl feedstocks. 3. flow scheme comparison. *Hydrocarbon Processing* **62**, 99–103 (1983).

[152] MargitfalviI, J., Guczi, L. & Weiss, A. H. Reaction routes for hydrogenation of acetylene-etylene mixtures using a double labeling method. *Reaction Kinetics and Catalysis Letters* **15**, 475–479 (1980).

[153] Molnar, A., Sarkany, A. & Varga, M. Hydrogenation of carbon-carbon multiple bonds: chemo-, regio- and stereo-selectivity. *Journal of Molecular Catalysis a-Chemical* **173**, 185–221 (2001).

[154] Alammar, A. S. & Webb, G. Hydrogenation of acetylene over supported metal-catalysts .1. adsorption of [c-14]acetylene and [c-14]ethylene on silica supported rhodium, iridium and palladium and alumina supported palladium. *Journal of the Chemical Society-Faraday Transactions I* **74**, 195–205 (1978). Part 1.

[155] Bos, A. N. R. & Westerterp, K. R. Mechanism and kinetics of the selective hydrogenation of ethyne and ethene. *Chemical Engineering and Processing* **32**, 1–7 (1993).

[156] Borodzinski, A. & Golebiowski, A. Surface heterogeneity of supported palladium catalyst for the hydrogenation of acetylene-ethylene mixtures. *Langmuir* **13**, 883–887 (1997).

[157] Borodzinski, A. & Cybulski, A. The kinetic model of hydrogenation of acetylene-ethylene mixtures over palladium surface covered by carbonaceous deposits. *Applied Catalysis A-General* **198**, 51–66 (2000). Times Cited: 14.

[158] Borodzinski, A. Hydrogenation of acetylene-ethylene mixtures on a commercial palladium catalyst. *Catalysis Letters* **63**, 35–42 (1999). Times Cited: 14.

[159] Borodzinski, A. The effect of palladium particle size on the kinetics of hydrogenation of acetylene-ethylene mixtures over pd/sio2 catalysts. *Catalysis Letters* **71**, 169–175 (2001).

[160] Teschner, D. *et al.* Alkyne hydrogenation over pd catalysts: A new paradigm. *Journal of Catalysis* **242**, 26–37 (2006).

[161] Borodzinski, A. & Bond, G. C. Selective hydrogenation of ethyne in ethene rich streams on palladium catalysts. part1. effect of changes to the catalyst during. *Catalysis Reviews-Science and Engineering* **48**, 91–144 (2006).

[162] G.C.Bond. *Catalysis by Metals* (Academic Press, London, 1962).

[163] P., B. J., Cosyns, J., Derrien, M. & Leger, G. Newest hydrogenation catalysts. *Hydrocarbon Processing* **64**, 51–59 (1985).

[164] Sheridan, J. The metal-catalyzed reaction between acetylene and hydrogen. 3. some effects of added substances on the reaction over nickel. *Journal of the Chemical Society* 301–305 (1945).

[165] Sheridan, J. The metal-catalyzed reaction between acetylene and hydrogen. 4. reaction over platinum. *Journal of the Chemical Society* 305–311 (1945).

[166] Zhang, Q. W., Li, J., Liu, X. X. & Zhu, Q. M. Synergetic effect of pd and ag dispersed on al2o3 in the selective hydrogenation of acetylene. *Applied Catalysis A-General* **197**, 221–228 (2000).

[167] Khan, N. A., Shaikhutdinov, S. & Freund, H. J. Acetylene and ethylene hydrogenation on alumina supported pd-ag model catalysts. *Catalysis Letters* **108**, 159–164 (2006).

[168] Gonzalez, S., Neyman, K. M., Shaikhutdinov, S., Freund, H. J. & Illas, F. On the promoting role of ag in selective hydrogenation reactions over pd-ag bimetallic catalysts: A theoretical study. *Journal of Physical Chemistry C* **111**, 6852–6856 (2007).

[169] Ponec, V. Catalysis by alloys in hydrocarbon reactions. *Advances in Catalysis* **32**, 149–214 (1983).

[170] Ponec, V. Alloy catalysts: the concepts. *Applied Catalysis A-General* **222**, 31–45 (2001).

[171] Westerterp, R., Bos, R., Wijngaarden, R., Kusters, W. & Martens, A. Selective hydrogenation of acetylene in an ethylene stream in an adiabatic reactor. *Chemical Engineering and Technology* **25**, 529–539 (2002).

[172] Cider, L. & Schoon, N. H. Hydrogenation of acetylene at transient conditions in the presence olefins and carbon-monoxide over palladium. *Industrial and Engineering Chemistry Research* **30**, 1437–1443 (1991).

[173] Sarkany, A., Guczi, L. & Weiss, A. H. On the aging phenomenon in palladium catalyzed acetylene hydrogenation. *Applied Catalysis* **10**, 369–388 (1984).

[174] Sarkany, A., Weiss, A. H., Szilagyi, T., Sandor, P. & Guczi, L. Green oil poisoning of a pd/a12o3 acetylene hydrogenation catalyst. *Applied Catalysis* **12**, 373–379 (1984).

[175] Leviness, S., Nair, V., Weiss, A. H., Schay, Z. & Guczi, L. Acetylene hydrogention selectivity control on pdcu/al2o3 catalysts. *Journal of Molecular Catalysis* **25**, 131–140 (1984).

[176] Kim, W. J., Shin, E. W., Kang, J. H. & Moon, S. H. Performance of si-modified pd catalyst in acetylene hydrogenation: catalyst deactivation behavior. *Applied Catalysis A-General* **251**, 305–313 (2003).

[177] Kim, W. J., Kang, J. H., Ahn, I. Y. & Moon, S. H. Deactivation behavior of a tio2-added pd catalyst in acetylene hydrogenation. *Journal of Catalysis* **226**, 226–229 (2004).

[178] Larsson, M., Jansson, J. & Asplund, S. The role of coke in acetylene hydrogenation on pd/alpha-al2o3. *Journal of Catalysis* **178**, 49–57 (1998).

[179] Battiston, G. C., Dalloro, L. & Tauszik, G. R. Performance and aging of catalysts for the selective hydrogenation of acetylene: a micropilot-plant study. *Applied Catalysis* **2**, 1–17 (1982).

[180] Ahn, I. Y., Lee, J. H., Kum, S. S. & Moon, S. H. Formation of c4 species in the deactivation of a pd/sio2 catalyst during the selective hydrogenation of acetylene. *Catalysis Today* **123**, 151–157 (2007).

[181] Subrahmanyam, C., Magureanu, A., Renken, A. & Kiwi-Minsker, L. Catalytic abatement of volatile organic compounds assisted by non-thermal plasma - part 1. a novel dielectric barrier discharge reactor containing catalytic electrode. *Applied Catalysis B-Environmental* **65**, 150–156 (2006).

[182] Badini, C. & Laurella, F. Oxidation of fecral alloy: influence of temperature and atmosphere on scale growth rate and mechanism. *Surface and Coatings Technology* **135**, 291–298 (2001).

[183] Yuranov, I., Kiwi-Minsker, L. & Renken, A. Structured combustion catalysts based on sintered metal fibre filters. *Applied Catalysis B-Environmental* **43**, 217–227 (2003).

[184] Chao, J., Lin, C. T. & Chung, T. H. Vapor-pressure of coal chemicals. *Journal of Physical and Chemical Reference Data* **12**, 1033–1063 (1983).

[185] Kiwi-Minsker, L., Semagina, N. & Renken, A. *Metal Nanoclusters in Catalysis and Material Science: The Issue of Size Control* (Elsevier B.V., 1998).

[186] Cusanelli, A., Frey, U., Richens, D. T. & Merbach, A. E. The slowest water exchange at a homoleptic mononuclear metal center: Variable-temperature and variable-pressure o-17 nmr study on [ir(h2o)(6)](3+). *Journal of the American Chemical Society* **118**, 5265–5271 (1996).

[187] Roe, D. C. Sapphire nmr tube for high-resolution studies at elevated pressure. *Journal of Magnetic Resonance* **63**, 388–391 (1985).

[188] Vander Wal, R. L. & Hall, L. J. Carbon nanotube synthesis upon stainless steel meshes. *Carbon* **41**, 659–672 (2003).

[189] Louis, B. *et al.* Carbon nanofibers grown over graphite supported ni catalyst: relationship between octopus-like growth mechanism and macro-shaping. *Topics in Catalysis* **45**, 75–80 (2007).

[190] Walker, P., Shelef, M. & Anderson, R. *Chemistry and Physics of Carbon*, vol. 4 (Marcel Dekker, New York, 1968).

[191] McKee, D. *Chemistry and Physics of Carbon*, vol. 16 (Marcel Dekker, New York, 1981).

[192] Hamwi, A., Alvergnat, H., Bonnamy, S. & Beguin, F. Fluorination of carbon nanotubes. *Carbon* **35**, 723–728 (1997).

[193] Sing, K. S. W. *et al.* Reporting physisorption data for gas solid systems with special reference to the determination of surface-area and porosity (recommendations 1984). *Pure and Applied Chemistry* **57**, 603–619 (1985).

[194] Lakshminarayanan, P. V., Toghiani, H. & Pittman, C. U. Nitric acid oxidation of vapor grown carbon nanofibers. *Carbon* **42**, 2433–2442 (2004).

[195] Rasheed, A., Howe, J. Y., Dadmun, M. D. & Britt, P. F. The efficiency of the oxidation of carbon nanofibers with various oxidizing agents. *Carbon* **45**, 1072–1080 (2007).

[196] Marchon, B., Carrazza, J., Heinemann, H. & Somorjai, G. A. Tpd and xps studies of o-2, co2, and h2o adsorption on clean polycrystalline graphite. *Carbon* **26**, 507–514 (1988).

[197] Figueiredo, J. L., Pereira, M. F. R., Freitas, M. M. A. & Orfao, J. J. M. Modification of the surface chemistry of activated carbons. *Carbon* **37**, 1379–1389 (1999).

[198] Pereira, M. F. R., Orfao, J. J. M. & Figueiredo, J. L. Oxidative dehydrogenation of ethylbenzene on activated carbon catalysts 3. catalyst deactivation. *Applied Catalysis A: General* **218**, 307–318 (2001).

[199] Figueiredo, J. L., Pereira, M. F. R., Freitas, M. M. A. & Orfao, J. J. M. Characterization of active sites on carbon catalysts. *Industrial and Engineering Chemistry Research* **46**, 4110–4115 (2007).

[200] Zhuang, Q. L., Kyotani, T. & Tomita, A. The change of tpd pattern of o2-gasified carbon upon air exposure. *Carbon* **32**, 539–540 (1994).

[201] Zielke, U., Huttinger, K. J. & Hoffman, W. P. Surface-oxidized carbon fibers .1. surface structure and chemistry. *Carbon* **34**, 983–998 (1996).

[202] T., C. D., Cromarty, B. J. & Dilks, A. A theoretical investigation of molecular core binding and relaxation energies in a series of oxygen containing organic molecules of interest in the study of surface oxidation of polymers. *Journal of Polymer Science A-Polymer Chemistry* **16**, 3173–3184 (1978).

[203] Sherwood, P. M. A. Surface analysis of carbon and carbon fibers for composites. *Journal of Electron Spectroscopy and Related Phenomena* **81**, 319–342 (1996).

[204] Briggs, D. & Seah, M. (eds.) *Practical Surface Analysis-Second Edition*, vol. 1 (John Wiley and Sons, Inc., 1990).

[205] Valkenberg, M. H., deCastro, C. & Holderich, W. F. Immobilisation of ionic liquids on solid supports. *Green Chemistry* **4**, 88–93 (2002).

[206] Mehnert, C. P. Supported ionic liquid phases. *Chemistry-a European Journal* **11**, 50–56 (2004).

[207] Schrock, R. R. & Osborn, J. A. Catalytic-hydrogenation using cationic rhodium complexes .1. evolution of catalytic system and hydrogenation of olefins. *Journal of the American Chemical Society* **98**, 2134–2143 (1976).

[208] Dupont, J., Suarez, P. A. Z., Umpierre, A. P. & de Souza, R. F. Pd(ii)-dissolved in ionic liquids: A recyclable catalytic system for the selective biphasic hydrogenation of dienes to monoenes. *Journal of the Brazilian Chemical Society* **11**, 293–297 (2000).

[209] Cahela, D. R. & Tatarchuk, B. J. Permeability of sintered microfibrous composites for heterogeneous catalysis and other chemical processing opportunities. *Catalysis Today* **69**, 33–39 (2001).

[210] Schrock, R. R. & Osborn, J. A. Preparation and properties of some cationic complexes of rhodium(i) and rhodium(iii). *Journal of the American Chemical Society* **93**, 2397 (1971).

[211] Chaloner, P., Esteruelas, M., Joé, F. & Oro, L. *Homogeneous Hydrogenation-Catalysis by Metal Complexes*, vol. 15 (Kluwer Academic Publisher B.V., Dordrecht, Boston, London, 1994).

[212] Chauvin, Y., Mussmann, L. & Olivier, H. A novel class of versatile solvents for two-phase catalysis: Hydrogenation, isomerization, and hydroformylation of alkenes catalyzed by rhodium complexes in liquid 1,3-dialkylimidazolium salts. *Angewandte Chemie-International Edition in English* **34**, 2698–2700 (1996).

[213] Chauvin, Y. Two-phase catalysis in nonaqueous ionic liquids. *Actualite Chimique* 44–46 (1996).

[214] Pignolet, R. H. *Homogeneous Catalysis with Metal Phosphine Complexes* (Plenum Press, New York and London, 1983).

[215] Duckett, S. B., Newell, C. L. & Eisenberg, R. Observation of new intermediates in hydrogenation catalyzed by wilkinsons catalyst, rhcl(pph(3))(3), using parahydrogen-induced polarization. *Journal of the American Chemical Society* **116**, 10548–10556 (1994).

[216] Che, M. & Bennett, C. O. The influence of particle-size on the catalytic properties of supported metals. *Advances in Catalysis* **36**, 55–172 (1989). Times Cited: 368.

[217] Gigola, C. E., Aduriz, H. R. & Bodnariuk, P. Particle-size effect in the hydrogenation of acetylene under industrial conditions. *Applied Catalysis* **27**, 133–144 (1986).

[218] Ryndin, Y. A., Nosova, L. V., Boronin, A. I. & Chuvilin, A. L. Effect of dispersion of supported palladium on its electronic and catalytic properties in the hydrogenation of vinylacetylene. *Applied Catalysis* **42**, 131–141 (1988).

[219] Sarkany, A., Weiss, A. H. & Guczi, L. Structure sensitivity of acetylene ethylene hydrogenation over pd catalysts. *Journal of Catalysis* **98**, 550–553 (1986).

[220] Boitiaux, J. P., Cosyns, J. & Vasudevan, S. Hydrogenation of highly unsaturated-hydrocarbons over highly dispersed palladium catalyst .1. behavior of small metal particles. *Applied Catalysis* **6**, 41–51 (1983). Times Cited: 119.

[221] Sarkany, A. Formation of c-4 oligomers in hydrogenation of acetylene over pd/al2o3 and pd/tio2 catalysts. *Reaction Kinetics and Catalysis Letters* **74**, 299–307 (2001).

[222] Semagina, N., Renken, A., Laub, D. & Kiwi-Minsker, L. Synthesis of monodispersed palladium nanoparticles to study structure sensitivity of solvent-free selective hydrogenation of 2-methyl-3-butyn-2-ol. *Journal of Catalysis* **246**, 308–314 (2007).

[223] Van Hardeveld, R. & Hartog, F. The statistics of surface atoms and surface sites on metal crystals. *Surf. Sci.* **15**, 189–230 (1969).

[224] Paal, Z. *et al.* Rh/gnf catalysts: Characterization and catalytic performance in methylcyclopentane reactions. *Catalysis Today* **102**, 254–258 (2005).

[225] Semagina, N., Renken, A. & Kiwi-Minsker, L. Pd nanoparticles size effect in 1-hexyne selective hydrogenation. *J. Phys. Chem. C.* **111**, 13933–13937 (2007).

[226] Toebes, M. L., van Dillen, J. A. & de Jong, Y. P. Synthesis of supported palladium catalysts. *Journal of Molecular Catalysis A-Chemical* **173**, 75–98 (2001).

[227] Jackson, S. D. & Casey, N. J. Hydrogenation of propyne over palladium catalysts. *Journal of the Chemical Society-Faraday Transactions* **91**, 3269–3274 (1995).

[228] Albers, P. *et al.* Investigations of palladium catalysts on different carbon supports. *Journal of Catalysis* **181**, 145–154 (1999).

[229] Tysoe, W. T., Nyberg, G. L. & Lambert, R. M. Low-temperature catalytic chemistry of the pd(111) surface - benzene and ethylene from acetylene. *Journal of the Chemical Society-Chemical Communications* 623–625 (1983).

[230] Barbier, J., Lamy Pitarea, E., Marecot, J., Boitiaux, Cosmys, J. & Verna, F. Role of sulfur in catalytic hydrogenation reactions. *Advances in Catalysis* **37**, 279 (1990).

[231] R.G.Finke. *Metal nanoparticles: synthesis, characterization and application* (Marcel Dekker, New York, 2002).

[232] Haumann, M., Dentler, K., Joni, J., Riisager, A. & Wasserscheid, P. Continuous gas-phase hydroformylation of 1-butene using supported ionic liquid phase (silp) catalysts. *Advanced Synthesis and Catalysis* **349**, 425–431 (2007).

[233] Ruta, M., Yuranov, I., Dyson, P. J., Laurenczy, G. & Kiwi-Minsker, L. Structured fiber supports for ionic liquid-phase catalysis used in gas-phase continuous hydrogenation. *Journal of Catalysis* **247**, 269–276 (2007).

[234] Toshima, N. *Fine Particles: Synthesis, Characterization and Mechanism of Growth* (Marcel Dekker, New York, 2000).

[235] Kralik, M. & Biffis, A. Catalysis by metal nanoparticles supported on functional organic polymers. *Journal of Molecular Catalysis A-Chemical* **177**, 113–138 (2001).

[236] Umpierre, A. P., Machado, G., Fecher, G. H., Morais, J. & Dupont, J. Selective hydrogenation of 1,3-butadiene to 1-butene by pd(0) nanoparticles embedded in imidazolium ionic liquids. *Advanced Synthesis and Catalysis* **347**, 1404–1412 (2005).

[237] Dupont, J. On the solid, liquid and solution structural organization of imidazolium ionic liquids. *Journal of the Brazilian Chemical Society* **15**, 341–350 (2004).

[238] Verwey, E. *Theory of Stability of Lyophobic Colloids* (Dover Publications, Inc, New York, 1999).

[239] Bostrom, M., Williams, D. R. M. & Ninham, B. W. Specific ion effects: Why dlvo theory fails for biology and colloid systems. *Physical Review Letters* **8716**, 168103 (2001).

[240] Camper, D., Becker, C., Koval, C. & Noble, R. Low pressure hydrocarbon solubility in room temperature ionic liquids containing imidazolium rings interpreted using regular solution theory. *INDUSTRIAL and ENGINEERING CHEMISTRY RESEARCH* **44**, 1928–1933 (2005).

[241] Migowski, P. *et al.* Synthesis and characterization of nickel nanoparticles dispersed in imidazolium ionic liquids. *Physical Chemistry Chemical Physics* **9**, 4814–4821 (2007).

[242] Chiappe, C. & Pieraccini, D. Ionic liquids: solvent properties and organic reactivity. *Journal of Physical Organic Chemistry* **18**, 275–297 (2005).

[243] Anthony, J. L., Anderson, J. L., Maginn, E. J. & Brennecke, J. F. Anion effects on gas solubility in ionic liquids. *Journal of Physical Chemistry B* **109**, 6366–6374 (2005).

Curriculum Vitae

EDUCATION

2005-2008 **Ecole Polytechnique Fédérale de Lausanne, Switzerland**

Ph.D. in Environment

1997-2003 **Politecnico di Milano, Italy**

Master of Science in Chemical Engineering. Main subjects: Thermodynamics, Industrial Chemistry, Fundamentals of Chemical Engineering, Unit Operations of Chemical Plants

2000-2001 **Ecole Polytechnique Fédérale de Lausanne, Switzerland**

Student exchange program at the department of Chemical Engineering

WORK EXPERIENCE

2005-2008 **Ecole Polytechnique Fédérale de Lausanne, Switzerland**

Research Assistant at the Group of Chemical Reaction Engineering

2004-2005 **Dow Chemical, Italy**

Commercial Development Representative

2003 **Dow Chemical, Italy**

6 month process engineering internship

2002 **Institut National Polytechnique de Toulouse, France**

6 month research internship at the Laboratory for Catalysis and Fine Chemistry, in collaboration with the Sensor Lab at the University of Brescia (Italy)

LANGUAGES

Italian Native speaker

English Fluent

French Fluent

Spanish Fluent

German Beginner

INTERNATIONAL COLLABORATIONS in the framework of IDECAT (Integrated Design of Catalytic Nanomaterials for a Sustainable Production)

2007 Department of Inorganic Chemistry at the Fritz Haber Institute of the Max Planck Society, Berlin, Germany

2006 Department of Industrial Chemistry and Engineering of Materials, University of Messina, Italy

PUBLICATIONS

- M.Ruta, D.Rosenthal, R. Schlögl, L.Kiwi Minsker, *Combined X-ray photoelectron spectroscopy (XPS) and temperature programmed desorption (TPD) study of oxygen-functionalized carbon nanofibers on metallic filters as catalyst support*, in preparation.
- M.Ruta, G.Laurenczy, P.J.Dyson, L. Kiwi-Minsker, *Pd-nanoparticles in supported ionic liquid phase (SILP) as highly stable catalysts for selective hydrogenation under continuous-flow,* Journal of Physical Chemistry C, in press.
- M.Ruta, N.Semagina, L.Kiwi-Minsker, *Monodispersed Pd nanoparticles for acetylene hydrogenation: particle size and support effects,* Journal of Physical Chemistry C, in press.
- M.Ruta, I.Yuranov, P.J.Dyson, G.Laurenczy, L.Kiwi-Minsker, *Structured fiber supports for ionic liquid-phase catalysis in gas-phase continuous hydrogenation,* Journal of Catalysis 247 (2007) 269-276.

ORAL PRESENTATIONS

- M.Ruta, N.Semagina, L.Kiwi-Minsker, *Monodispersed Pd nanoparticles on CNF-structured supports for acetylene hydrogenation,* 14th International Congress on Catalysis, 13-18 July 2008, Seoul, Korea.

POSTERS

- M.Ruta, D.Rosenthal, L.Kiwi-Minsker, R. Schlögl, *Combined XPS and TDS study of oxygen functionalized CNF,* NT08-International Conference on the Science and Application of Nanotubes, 29 June-4 July 2008, Montpellier, France.
- M.Ruta, I.Yuranov, P.J.Dyson, G.Laurenczy, L.Kiwi-Minsker, *Ionic Liquid on carbon nanofiber-based structured supports for continuous gas-phase hydrogenation,* Europacat VIII, 26-31 August 2007, Turku, Finland.
- N.Semagina, M.Ruta, A.Renken, L.Kiwi-Minsker, *Microemulsion-derived palladium nanoparticles in liquid- and gas-phase selective hydrogenations,* Europacat VIII, 26-31 August 2007, Turku, Finland.
- M.Gangeri, S. Perathoner, G.Centi, P.Lanzafame, M.Fiorello, M.Ruta, L.Kiwi-Minsker, *Sintered metal fibers as new macrostructured supports for the catalytic electrodes used in PEM fuel cells,* Europacat VIII, 26-31 August 2007, Turku, Finland.
- M.Ruta, I.Yuranov, P.J.Dyson, G.Laurenczy, L.Kiwi-Minsker, *Structured SILP catalyst for gas phase selective hydrogenation*, DECHEMA-Green Solvents for Processes, 8-11 October 2006, Friedrichshafen, Germany.